Performance of Biologically Inspired Flapping Foils

by

Melissa B. Read

S.B., Mechanical Engineering
Massachusetts Institute of Technology, 2004

SUBMITTED TO THE DEPARTMENT OF MECHANICAL ENGINEERING
IN PARTIAL FULFILLMENT OF THE REQUIREMENTS FOR THE DEGREE OF

MASTER OF SCIENCE IN MECHANICAL ENGINEERING

AT THE

MASSACHUSETTS INSTITUTE OF TECHNOLOGY

JUNE 2006

Signature of Author _____
Department of Mechanical Engineering
May 12, 2006

Certified by _____
Alexandra H. Techet
Assistant Professor of Mechanical and Ocean Engineering
Thesis Supervisor

Accepted by _____
Lallit Anand
Professor of Mechanical Engineering
Chairman, Department Committee on Graduate Students

Performance of Biologically Inspired Flapping Foils

by

Melissa B. Read

Submitted to the Department of Mechanical Engineering
On May 12, 2006 in Partial Fulfillment of the
Requirements for the Degree of Master of Science in
Mechanical Engineering

ABSTRACT

Flapping foil propulsion is thought to provide AUVs with greater maneuverability than propellers. This thesis seeks to simplify the design process for this type of propulsion system by identifying thrust and wake characteristics for flapping foils and determining how these factors scale with certain parameters. First, the wake of a flapping NACA 0030 foil was studied qualitatively using fluorescent dye visualizations. The foil was heaved and pitched in a sinusoidal fashion. The effects of varying Reynolds number, Strouhal number, maximum pitch angle, and the phase shift between heave and pitch were studied. It was determined that at very low Strouhal numbers the wake was 'S' like and at moderate Strouhal numbers the wake contained discreet horseshoe-like vortices. Next, the wake was studied quantitatively using particle image velocimetry (PIV). Through this technique, numerical thrust coefficients and vorticity strengths were obtained as well as qualitative information regarding the morphology of the wake. The coefficient of thrust peaked at a different Strouhal number for each Reynolds number studied. This trend was compared to natural phenomenon. Impulsively started maneuvers were also studied using PIV. Both single flaps and half flaps of the foil were studied. It was determined that impulsively started single flaps produced a much larger maximum coefficient of thrust than the impulsively started half flaps. Many of the experiments were repeated using a biologically inspired trout tail shaped foil.

Thesis Supervisor: Alexandra H. Techet
Title: Assistant Professor of Mechanical and Ocean Engineering

Acknowledgements

I would first and foremost like to thank my advisor, Professor Alexandra H. Techet. She has served as an amazing guide during my first foray into experimental research. Her patience and her expertise in hydrodynamics have proved invaluable on this project.

Next, I would like to thank Cha Ling O'Connell, a UROP, who perfected the processes of manufacturing the rigid NACA foils used in the experiments. I would also like to thank Matthew Krueger, an undergraduate member of the Experimental Hydrodynamics Laboratory, who developed the technique used to manufacture the flexible NACA foils as well as the formula for the fluorescent dye used in the flow visualization experiments. In addition I would like to thank Alex Hornstein, another UROP who built the motor controller used to drive the experimental apparatus.

The other members of the Experimental Hydrodynamics Laboratory, namely Tadd Truscott, Matthew Weldon, Brenden Epps, and David Tobias, were incredibly helpful throughout the entire project. They assisted me on everything from experimental setup to software issues to hydrodynamic theory. I owe them each a tremendous amount of thanks.

Finally, I would like to thank my family, Wayne, Ceil, and Justin Read. Without the support of my parents and brother I would not be where I am today.

Contents

List of Figures

List of Tables

List of Symbols and Abbreviations

α angle of attack

Γ circulation

δt time between laser pulses

η hydrodynamic efficiency

θ pitch angle

θ_o maximum pitch angle

μ dynamic viscosity

ρ density

τ non-dimensional time

Φ phase shift between heave and pitch

Ψ period

w vorticity

c chord

C_t coefficient of thrust

f frequency

f_c camera frequency

h heave

h_o maximum heave amplitude

P_i power input

P_o power output

Re Reynolds number

s span

St Strouhal number

T thrust

$\overline{T}$ phase Average Thrust

U forward velocity

U_h maximum heave velocity

V volume

AUV Autonomous Underwater Vehicle

PIV Particle Image Velocimetry

Chapter 1

Introduction

1.1 Motivation

Biomimetic flapping foil propulsion is the use of biologically inspired hydrofoils to propel a watercraft in a manner similar to fish swimming. This is currently being pursued as an alternative to traditional propeller driven watercrafts. One of the main advantages flapping foils have over propellers is increased maneuverability through directed thrust. A fish can make a turn in half a body length [Weihs, 1972] whereas propeller driven watercraft can take as many as ten body lengths to complete a turn. At MIT, a sea turtle inspired biomimetic flapping foil autonomous underwater vehicle has been developed which exploits this high maneuverability to operate in highly energetic environments, such as the surf zone, where fish swim [Licht *et al.*, 2004]. Efficiencies of flapping foils have been measured in excess of 80% [Anderson *et al.*, 1998]. While much work has been done on the efficiency and thrust capabilities of flapping foils and how they change with Strouhal number, angle of attack, and other variables [Anderson, 1996], only a small sampling of Reynolds numbers have been studied. Numerical methods have also been used to predict performance but are limited to somewhat low Reynolds numbers [Blondeaux *et al.*, 2005]. Several review papers provide a broad overview of work that has been done in the field [Triantafyllou *et al.*, 2004]. The ultimate aim of the research conducted in this thesis is to create a scaling law to predict flapping foil performance for all Reynolds numbers with the purpose of improving the design of foils for watercraft propulsion.

The inspiration for flapping foil propulsion comes from nature. Fish have long been noted for their exemplary maneuverability and thrust capability [Videlar, 1993]. There are several aspects of fish biological makeup thought to account for this including fin kinematics, body flexibility, and the ability of some marine animals to keep a laminar boundary layer at high Reynolds numbers [Blake, 1983]. Body flexibility is not practical for watercraft design and the mechanisms which allow dolphins to keep a laminar boundary layer are not well understood; therefore, the fin kinematics are the simplest aspect of fish locomotion to integrate into watercraft design. Breder (1926) categorized fish according to the mode of their kinematics, first by whether they were propelled by peripheral fins or by a wave undulating through the body and the caudal fin, commonly referred to as the tail. Those fish that use an undulating wave for propulsion are further broken down by the percentage of the body that participates in the wave. In angulliforms, such as eels, the entire body undulates. On the other end of the spectrum, thunniforms, like tuna, keep almost their entire body straight, with only their caudal fin participating in the wave. The kinematics of a carangiform swimmer were implemented for the experiments carried out in this thesis. A carangiform keeps the majority of its body straight, undulating only the last one-third [Sfakiotakis *et al.*, 1999]. The foil follows the motion of the tail and can be represented as a simple sine wave, as shown in figure 1.

The wake morphology behind the flapping foils varies with Strouhal number when Reynolds number is held constant [Anderson, 1996]. At relatively low Strouhal numbers, the wake behind flapping foils is a von Kármán vortex street, which is a drag wake. As Strouhal number is increased, the wake changes to a reverse von Kármán vortex street, which is a thrust producing wake [von Kármán and Burgers, 1934]. This thesis explores this changing wake morphology and how it scales with Reynolds number both qualitatively using florescent dye visualizations and quantitatively with particle image velocimetry.

The end goal of this research is to create an understanding of the thrust and efficiencies produced by flapping foils broad enough to be used by design engineers with a relatively limited knowledge of fluid dynamics.

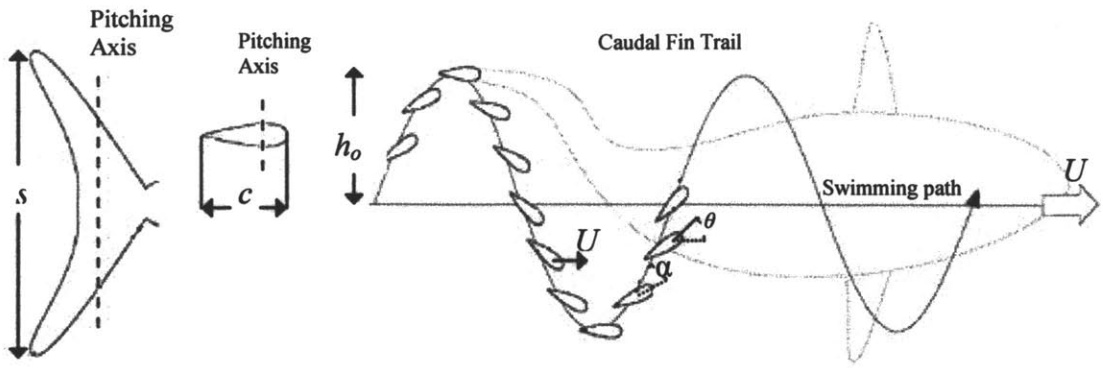

Figure 1: Relationship between a flapping foil and a caudal fin [Sfakiotakis *et al.*, 1999].

1.2 Chapter Preview

The design and construction of the mechanism that controls the motion of the flapping foils required significant consideration. The second chapter of this thesis covers the design of the apparatus used in each of the experiments subsequently discussed. The kinematics and geometry of the foil are defined because the kinematics of the heaving and pitching mechanism are dependant on them. The choices of kinematics and mechanism design of prior experiments are also considered. The construction of the foils and their interface with the pitching and heaving mechanism are described. Finally, potential improvements to the machine are suggested.

The third chapter covers fluorescent dye visualizations used to qualitatively observe the three-dimensional wake structures behind flapping foils at low Reynolds numbers. The dye application methodology and imaging techniques are covered. Prior results and methodologies of flapping foil wake visualizations are discussed. The visualizations are compared to and confirmed by CFD results. Unfortunately, at high Reynolds numbers the dye dissipated too quickly to provide clear images.

Experiments resulting in quantitative thrust data for flapping foil propulsion are the subjects of chapter 4. Particle image velocimetry, a technique that measures the velocity flow field around the foil, is explained. Methods for defining and measuring thrust, efficiency, and power are defined. The cases discussed in this chapter are limited

to the cases used in the dye visualizations. The results obtained are compared to other experimental and numerical results.

Chapter 5 explores the thrust generated at higher Reynolds and Strouhal numbers than the cases studied in chapter 4. The trends in morphologies are also discussed. These thrust and morphology characteristics are then compared to those of various high and low Reynolds number swimmers.

When discussing maneuverability, the stopping and starting characteristics are critical. Impulsively started single and half flaps model a foil beginning to flap from rest. Chapter 6 discusses the thrust and formation characteristics seen in a single flap and a half flap. Two different ways of calculating thrust are compared.

The foil used in most of these experiments, a NACA 0030, is an approximation of the tail of a carangiform swimmer. Chapter 7 looks at several of the experiments performed in chapters 5 and 6 performed with a two-dimensional model of a trout tail as opposed to the NACA foil. Other foil geometries are also reviewed.

Last, chapter eight discusses the conclusions of these experiments and makes recommendations for further research.

Chapter 2

Apparatus Design

2.1 Overview

In order to measure the performance of flapping foil propulsion, a mechanism to drive the foil had to be built. This chapter defines the kinematics and geometry of the foil that in turn define the kinematics and geometry of the mechanism. The parameters varied and the mechanisms used in prior flapping foil experiments are discussed. The detailed design of the apparatus is described. The motor control, foil design and construction, and foil to drive mechanism interface are all discussed.

2.2 Flapping Foil Kinematics and Geometry

As mentioned in the motivation section, most experiments done with flapping hydrofoils use them as an approximation of carangiform swimming. Generally carangiform swimmers are regarded as using only the last one-third of their body while the first two-thirds remains rigid [Sfakiotakis *et al.*, 1999]. This motion is simplified as a combination of oscillatory heaving and pitching. The equation of heave motion is

$$h(t) = h_o \sin(2\pi f t) \qquad \textit{Eq. 1}$$

where h_o is the maximum amplitude of the heave motion, f is the frequency of oscillation in Hz, and t is time in seconds. The equation for pitch is

$$\theta(t) = \theta_o \sin(2\pi ft + \Phi) \qquad \textit{Eq. 2}$$

where θ_o is the maximum pitch angle and Φ is the phase shift between heave and pitch. The motion of the foil is sometimes described with respect to a non-dimensional time τ defined as

$$\tau = 2\pi ft \qquad \textit{Eq. 3}$$

Figure 2 shows the pitch and heave kinematics of a flapping foil with $\Phi=90^\circ$.

Rather than explicitly define the frequency of oscillation and the forward velocity of the foil, these parameters are typically derived from the dimensionless parameters Strouhal number and Reynolds number. Strouhal number is defined as

$$St = \frac{2h_o f}{U} \qquad \textit{Eq. 4}$$

where U is forward velocity. Reynolds number is defined as

$$Re = \frac{\rho U c}{\mu} \qquad \textit{Eq. 5}$$

where ρ is the density of the fluid, μ is the dynamic viscosity, and c is the chord length of the foil. Chord length is graphically depicted in figure 3. Span is also defined.

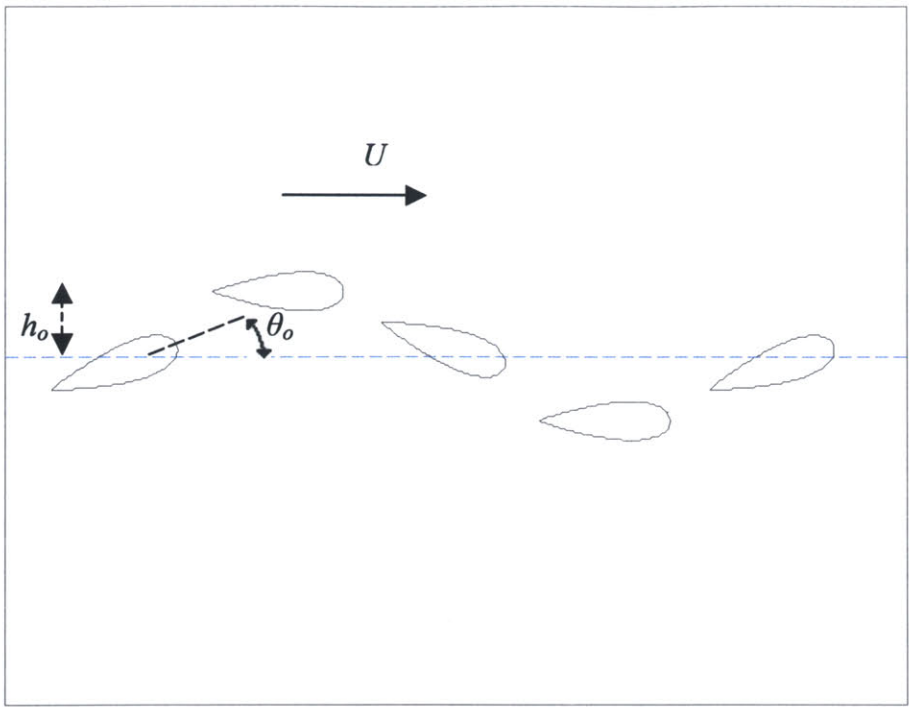

Figure 2: Heave and pitch profile for flapping foil with θ_o=20° and Φ=90° from τ=0 to 2π.

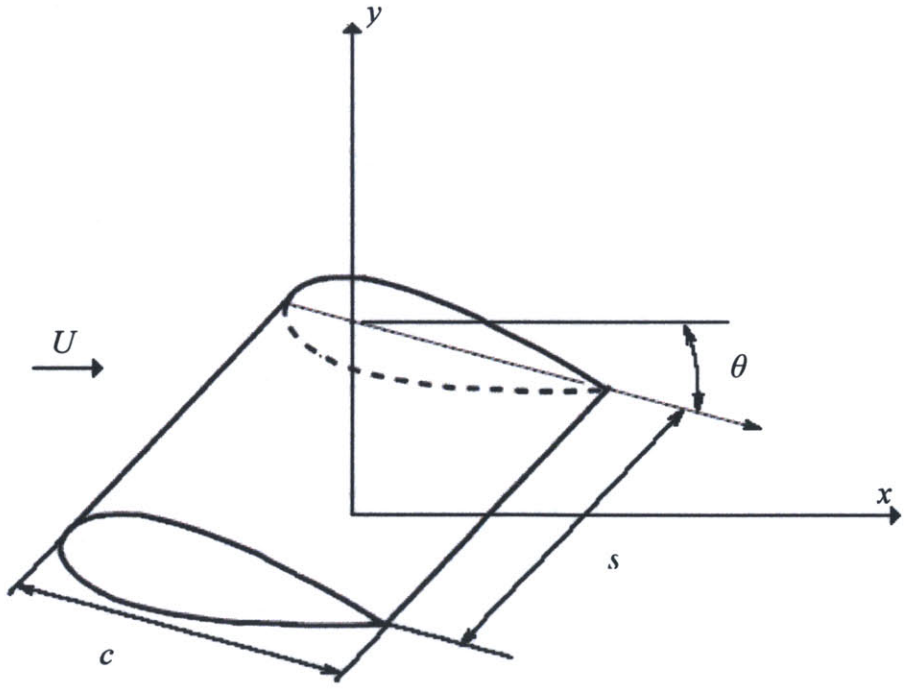

Figure 3: Foil geometry where *c* is chord length and *s* is span.

2.3) Previous Experimental Parameters and Mechanisms

Much experimental work has been done involving heaving and pitching flapping foils. The experimental setup of these experiments has varied significantly. Some experiments have used separate motors for the heaving and pitching motions. Other experiments have used mechanical linkages to control both heave and pitch with the same motor. While some studies opted to tow the foil forward, others kept the foil stationary and placed it in a water or air tunnel. The parameters varied in each experiment as well as the discreet values chosen for each parameter have differed. The size and shape of the airfoils have varied. Also, numerical methods have been used to simulate the flow field around flapping foils. While numerical methods do not have a physical experimental setup, the parameter choices and foil geometries used in the calculations are of note.

In Anderson (1996) particle image velocimetry was performed on heaving and pitching flapping foils. The heaving and pitching motions were controlled using one motor and a scotch-yoke mechanism. The foil was towed through a stationary tank using an A.C. motor. The foil used was an NACA 0012 foil with chord length c=38.1mm and a high aspect ratio. The foil was pivoted about the quarter-chord. The experiments were all performed at Reynolds number $Re=1100$. Strouhal number, maximum pitch angle, and the phase shift between heave and pitch were varied. The values of each of these parameters at each run are shown in table 1 [Anderson, 1996].

von Ellenrieder *et al.* (2003) performed dye visualizations on foils of much smaller aspect ratios than those studied by Anderson (1996). Separate stepper motors controlled the heaving and pitching motions. Rather than towing the foil, it was placed in a recirculating water tunnel. The foil used was an NACA 0030 foil with chord length c=19mm and an aspect ratio of three. The foil was pivoted about the quarter-chord. The Reynolds number the experiments were performed at was $Re=161.5$, significantly lower than the Reynolds number used in Anderson (1996). The ratio between maximum heave amplitude and chord length was kept constant at $h_o/c=0.5$. The parameters varied were Strouhal number, maximum pitch angle, and phase shift between heave and pitch. The values of these variables for each run are listed in table 2 [von Ellenrieder *et al.*, 2003].

St	θ_o	Φ
0.1, .02, .03	*0°, 7°,15°,*	*90°*
0.45	*50°, 45°, 60°*	*90°*
0.45	*30°*	*30°, 50°, 70°, 90°, 100°, 105°, 110°*

Table 1: Experimental parameters from Anderson (1996).

St	θ_o	Φ
0.2, 0.25, 0.3, 0.35, 0.4	*5°*	*90°*
0.35	*0°, 5°, 10°, 15°, 20°*	*90°*
0.35	*5°*	*60°, 75°, 90°, 105°, 120°*

Table 2: Experimental parameters from von Ellenreider *et al.* (2003).

Computational fluid dynamics performed by Blondeaux *et al.* (2005) were used to predict the flow around foils at parameters very similar to those used in von Ellenrieder *et al.* (2003). Obviously the CFD had no need for any physical mechanisms. The foil simulated was identical to the one used in von Ellenrieder *et al.* (2003). The Reynolds number was $Re=164$. The maximum pitch angle was $\theta_o=5°$, the phase shift between heave and pitch was $\Phi=90°$, and the ratio between maximum heave amplitude and chord length was $h_o/c=0.5$. Simulations were run at Reynolds numbers of $Re=0.175$ and 0.35 [Blondeaux *et al.*, 2005].

The experiments discussed are only a small sampling of those that have made significant contributions in the field of flapping foils. They were chosen because the experiments all dealt with foils that had significant three-dimensional effects or collected quantitative data regarding thrust and efficiencies. Both of these issues are important when considering the propulsion performance of flapping foils. For this reason, the parameters this thesis chose to consider are similar to those looked at in Anderson (1996), von Ellenreider *et al.* (2003), and Blondeaux *et al.* (2005). The foil predominately considered in this thesis is a NACA 0030 of chord length c=19mm and an aspect ratio of three, though other aspect ratios and a trout tail shaped foils were also studied. The ratio of maximum heave amplitude to chord length for all of the NACA foils was $h_o/c=0.5$. The parameter values used in this thesis are listed in table 3. These parameter values allow for direct comparison to prior experiments and the ability to look at new situations.

Re	*St*	θ_o	Φ
161.5	*0.2, 0.25, 0.3, 0.35, 0.4, 0.5, 0.6, 0.7, 0.8, 0.9, 1.0, 1.1, 1.2, 1.3, 1.4, 1.5*	*5°*	*90°*
161.5	*0.35, 0.8*	*0°, 5°, 10°, 15°, 20°*	*90°*
161.5	*0.35, 0.8*	*5°*	*60°, 75°, 90°, 105°, 120°*
750	*0.2, 0.3, 0.4, 0.5, 0.6, 0.7, 0.8, 0.9, 1.0, 1.1*	*5°*	*90°*
750, 1000	*0.5*	*0°, 5°, 10°, 15°, 20°*	*90°*
750, 1000	*0.5*	*5°*	*60°, 75°, 90°, 105°, 120°*
1000	*0.2, 0.3, 0.4, 0.5, 0.6, 0.7, 0.8*	*5°*	*90°*

Table 3: Experimental parameter values.

2.4 Design Strategy

Several strategies for how to build the experimental mechanism were considered. The design was broken down into three main modules and two dominating strategies for the design of each of these modules were proposed. The first module was the heaving and pitching mechanism. The second module was responsible for the forward motion of the foil. The last module consisted of the mechanism used for changing parameters such as maximum pitch angle and phase shift between heave and pitch.

The experiments in von Ellenrieder *et al.* (2003) used separate motors for heaving and pitching motions whereas the Anderson (1996) experiments used one motor in conjunction with a scotch-yoke mechanism to mechanically link heaving and pitching motion. There are pros and cons to both of these approaches. One advantage of separate motors is increased flexibility. This allows the mechanism to move in any combination of heaving and pitching rather than being limited to the motion governed by equations 1 and 2. Another advantage is increased precision. The addition of mechanical elements

stacks error in the system. The main advantage of mechanically coupled heave and pitch is increased fluidity of motion. Using separate motors, the pitching motor would have to rapidly change direction, which, without somewhat complicated controls, can lead to jerky motion. Conversely, a scotch yoke mechanism allows one motor to move at a constant speed, so smooth motion can be achieved with relatively simple motor control. Another advantage of using one motor is that regardless of any motor control issues, the relative motion between pitch and heave is guaranteed. One disadvantage is that the linkage has to be mechanically altered when parameters like maximum pitch angle are changed whereas in the dual motor strategy, the motor controller deals with the parameter changes. The scope of this thesis is limited to motions governed by equations 1 and 2, therefore the increased flexibility offered by the dual motor strategy was not necessary. Since the sampling between parameters is so sparse, the error introduced by stacking mechanical components was not thought to have a major impact on the data. Also, a great importance was placed on fluidity of the foil motion. Since using a mechanical linkage achieved this fluidity easier than with motor control, it was determined that a single motor in conjunction with a mechanical linkage between heave and pitch would be the best way to achieve the flapping foil motion.

The second main design choice was whether to use a recirculating water tunnel, like the one von Ellenreider *et al.* (2003) used, or whether to tow the foil forward through still water, as Anderson (1996) did. The main advantage of using a water tunnel is that since the foil does not move, the camera can be kept in a constant position while still always having the foil in frame. Another advantage is that data can be collected for long periods of time without having to worry about the foil running into the end of the tank. The main disadvantage of a water tunnel is that it can be difficult to produce a completely uniform flow field, especially at very low speeds. The main advantage of using a towing mechanism in a still tank is that the experiment can be made simply because it would not have to interface with a water tunnel. Additionally, still water is easier to achieve than uniform flowing water. Since the forward velocities are so small, ranging from U=8.5 mm/s to 52.6 mm/s, a large amount of data can be taken in a relatively small tank. Also, it should be noted the MIT recirculating water tunnel cannot run at speeds below approximately 500 mm/s. Due to the small space needed and the unavailability of a slow

speed water tunnel, it was determined that the foil would be towed through a tank of stationary water.

The final major design issue was how to change certain parameters such as phase shift between heave and pitch and maximum pitch angle. The other variable parameters, Reynolds number and Strouhal number, are changed through the motor control. The two competing strategies for altering these parameters were using sliding mechanisms to allow for infinitely many placements and using a finite number of locating pegs. The main advantage of using a sliding mechanism is the flexibility. This type of mechanism would allow for infinitely many maximum pitch angles and phase shifts. Using a finite number of pegs greatly simplifies the calibration process since certain positions can be found simply in a repeatable manner. Conversely, a sliding mechanism would require extensive calibration to ensure that the correct value of the parameter had been achieved. Since the number of values for which phase shift between heave and pitch and maximum pitch angle to be studied were relatively small, using a finite number of locating pegs was the clear winner. The details of this module, the heave and pitch mechanism, and the forward motion mechanism are all laid out in the following section.

2.5 Detail Design

The detail design of the experimental apparatus was approached so that each module could be made as simple as possible. Since the mechanism had to operate near water, corrosion resistant materials were chosen. This section discusses the details of the supporting structure and tank as well as the three modules discussed in the design strategy section: the heaving and pitching mechanism, the forward motion module, and the mechanism for changing parameters. The last module, for changing phase shift and pitch angle parameters, is not independent of the heaving and pitching mechanism, so these two modules will be discussed together.

The tank and supporting structure are relatively simple and easy to move. A breeder 40 glass tank, which has dimensions of 919mm long by 464mm wide by 430mm deep, was chosen because it would be significantly long enough to gather enough data,

Figure 4: Tank and frame.

wide enough to not interfere with the wake of the flapping foil, and deep enough so that surface and bottom effects would not be an issue. This tank sits on a frame made of 80/20 aluminum extrusions. The frame is intentionally kept sparse as not to impede any potential camera angles. The tank is placed on rubber strips on top of the aluminum to prevent it from slipping. The frame set on four leveling feet. The weight of the water in the tank, approximately 180 kg, is more than enough to prevent the structure from being inadvertently moved. The tank and supporting structure are shown in figure 4.

The forward drive mechanism is very simple. A precision lead screw is mounted to the right side of the 80/20 frame. At speeds below 2 Hz, a stepper motor coupled to the leadscrew with a helical coupling drives the leadscrew. At higher speeds, the stepper motor is removed and replaced with a fractional horsepower gear motor also coupled to the leadscrew with a helical coupling. The lead screw drives a precision sliding carriage on oil-lubricated bearings forward. An aluminum carriage which supports the heave and pitch mechanism, is mounted onto the precision sliding carriage. The aluminum carriage spans the entire tank. The left side of the aluminum carriage is supported by a plain nylon bearing surface sliding against the 80/20 frame. This module is shown in figure 5.

The heave and pitch mechanism allows heave and pitch to be controlled with just one motor. The mechanism allows a finite number of phase shifts between heave and pitch and maximum pitch angles, specifically phase shifts $\Phi=60°, 75°, 90°, 105°$, and

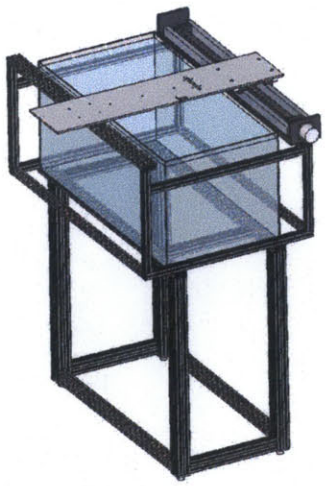

Figure 5: Forward driving lead screw

120° and maximum pitch angles θ_o=*0°, 5°, 10°, 15°,* and *20°*. The maximum heave amplitude is fixed at h_o=*9.5*mm noting that h_o/c=*0.5*. The mechanism that controls the heaving and pitching motion is shown in figure 6.

A large ball bearing linear guide is mounted onto the aluminum carriage spanning the tank. A smaller aluminum support structure is mounted to the top of the linear guide. Thus the small support structure can move back and forth relative to the large aluminum carriage in a side-to-side direction. A GBM stepping motor, product number 42BYG023, is mounted on the small support structure. The motor is a 2 phase, 1.8° step angle motor driven by a controller designed and constructed by an MIT undergraduate student, Alex Hornstein. The motor control is discussed in greater detail in the following section, motor control. The motor is coupled to a $^1/_4$" stainless steel shaft located between the motor and the large aluminum carriage by a pin hole coupling. The shaft is supported by two stainless steel ball bearings. At the end of the shaft is an aluminum coupling with a pin offset 9.5mm from the center. The pin extends below the aluminum coupling into a slot in the carriage. The total distance traveled by the small support structure is 19mm, twice the distance of the pin offset. The hydrofoil is pivoted from the small support structure, so this side-to-side motion corresponds to the heave of the hydrofoil. This motion is shown in figure 7.

The stepper motor controlling the heaving motion is a dual shaft motor, meaning the shaft not only extends below the motor to control heaving motion, but also above the

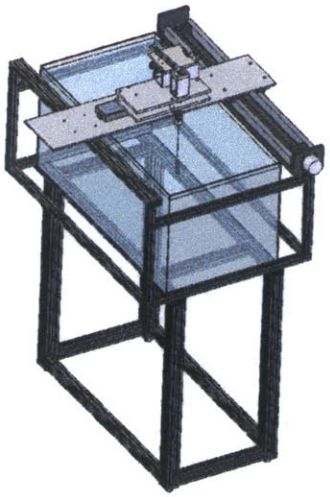

Figure 6: Heave and pitch mechanism.

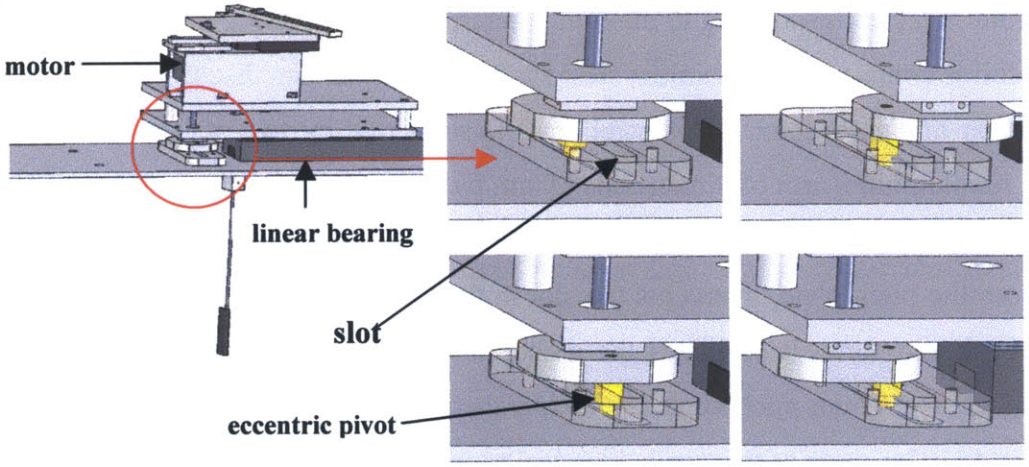

Figure 7: Kinematics of the heave mechanism. The heave mechanism is shown in relation to the rest of the machine on the left hand side. The right hand side shows the mechanism from left to right, top to bottom, at $\tau=0$, $\pi/2$, π, and $3\pi/2$. As the motor rotates, the eccentric pivot (which is highlighted in yellow) moves back and forth in the slot of the base (which is shown transparent.) This causes the main part of the mechanism, including the motor, to move back and forth atop the linear bearing.

motor. The pitching mechanism works off this secondary motor shaft. A precision steel ball thrust bearing is mounted on the shaft. The thrust bearing rests on a square piece of aluminum extrusion. On top of that bearing is an aluminum coupling which dictates the phase shift between heave and pitch. The coupling consists of five sets of screw holes. An aluminum bar with a protruding plain cylindrical bearing can be placed in any of the five sets of holes. This places the plain cylindrical bearing exactly out of phase with the roller bearing which controls heave. The phase shifts achieved are $\Phi=60°$, $75°$, $90°$, $105°$, and $120°$. The plain cylindrical bearing extends upward into a slot in the aluminum pitch plate. This pitch plate sits on top of a small ball bearing linear guide mounted to the small aluminum support structure. Therefore, when the single motor rotates, it causes the pitch plate to slide back and forth relative to the small aluminum support structure. Another plain cylindrical bearing extends upward from the pitch plate. It can be placed in one of four holes corresponding to maximum pitch angles of $\theta_o=5°$, $10°$, $15°$, and $20°$. The hydrofoil is connected to a stainless steel shaft via a mechanism discussed in detail in a later section of this chapter. This steel shaft is supported by two stainless steel ball bearings. An aluminum arm of dimensions 19mm by 254mm extends from the top of the shaft. This arm has a slot milled out of its center. The plain cylindrical bearing, which extends from the pitch plate, intercepts the slot in the aluminum arm. As the pitch plate oscillates back and forth, it oscillates the aluminum arm according to equation 2. For example, if the maximum pitch angle is $\theta_o=15°$, then the arm will oscillate between $\theta=-15°$ and $\theta=15°$. The angle of the arm is identical to the pitch angle of the foil. The $\theta_o=0°$ case was achieved by disconnecting the pitch mechanism from the motor and locking the foil in a $\theta_o=0°$ pitch position. The kinematics of the complete pitch and heave mechanism are shown in figure 8.

Both figures 7 and 8 show the heave and pitch motion for $\theta_o=20°$ and $\Phi=90°$. The system is also designed to perform at other maximum pitch angles and phase shifts. The configurations for each maximum pitch angle are shown in figure 9. The configurations for each phase shift are shown in figure 10.

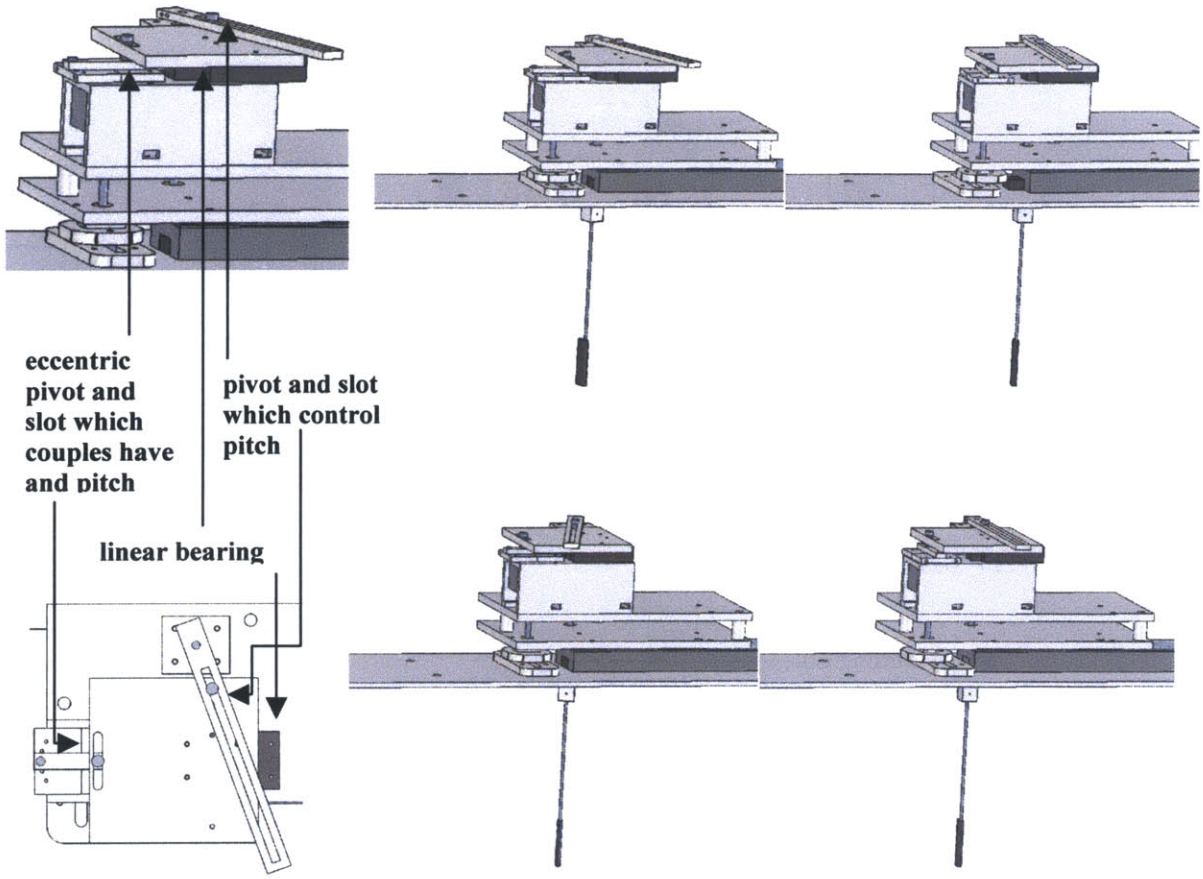

Figure 8: Kinematics of the pitching mechanism. The sinusoidal profile of the pitch is achieved in a similar way to that of the heave. An eccentric pin riding in a slot linked to a linear bearing causes linear motion. A pivot atop of that linear bearing rides in a slot that oscillates from the most negative value of pitch to the most positive value of pitch. The foil's shaft is located on the pivot of this angularly oscillating slot. The four images on the right show the mechanism from left to right, top to bottom, at $\tau=0$, $\pi/2$, π, and $3\pi/2$.

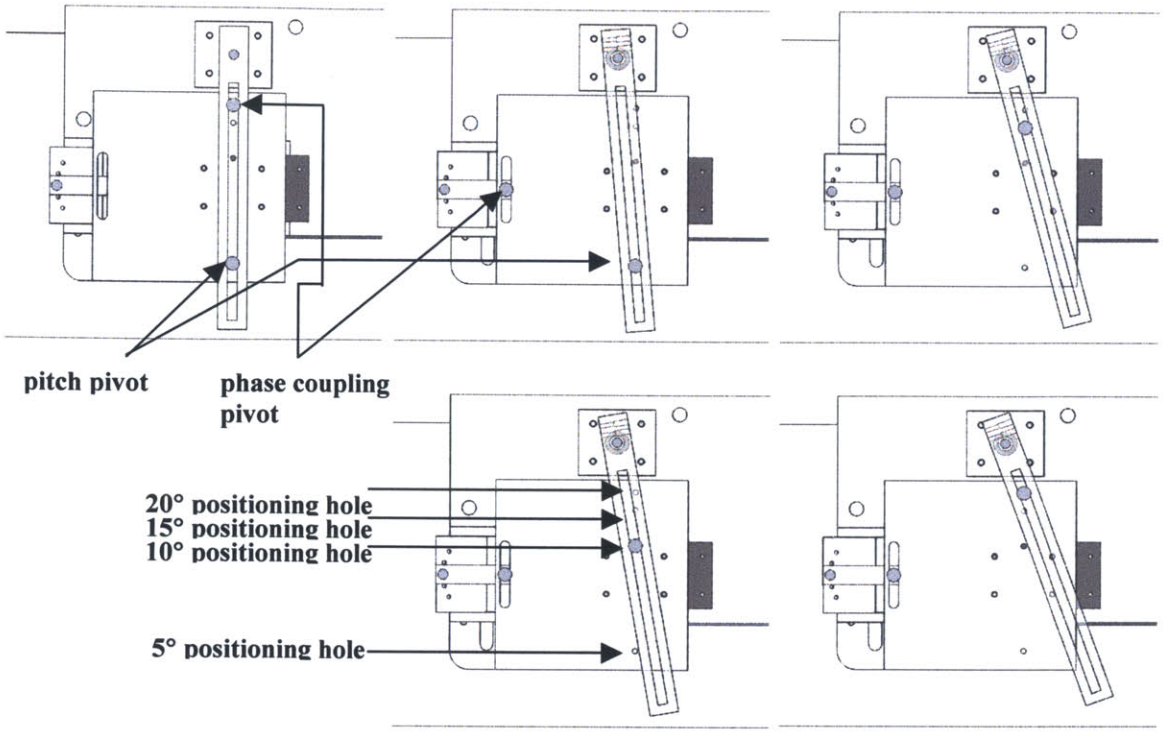

Figure 9: Configuration of the mechanism for maximum pitch angles from left to right, top to bottom, θ_o=0°, 5°, 10°, 15°, and 20°. Each of these configurations is shown at the same heave position. The long pivoting slot is shown in transparency. For the θ_o =5°, 10°, 15°, and 20° configurations, the pitch pivot is placed in one of four discreet positioning holes. For the θ_o =0° case, the coupling pivot between heave and pitch is removed and placed in the 20° position while the pitch pivot is placed in the 5° position. This locks the pivoting slot at θ_o=0°.

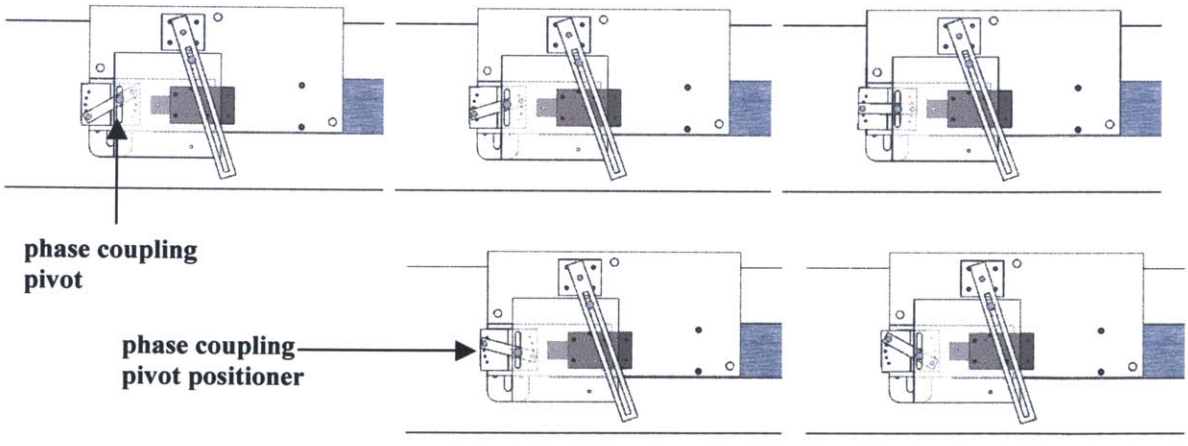

Figure 10: Configuration of the mechanism for phase shifts between heave and pitch from left to right, top to bottom, of Φ=60°, 75°, 90°, 105°, and 120°. The angle of the phase coupling pivot positioner relative to the drive shaft is changed by attaching a small aluminum bar, on which the coupling pivot is located, to one of the five sets of discreet hole locations corresponding to the various phase shifts. The block on which the pitch pivot is attached to is shown in transparency for a clearer view.

The design of this mechanism allows for a simple, repeatable way to change parameters. Most of the aluminum couplings are clamped into place. The initial alignment of these couplings was done by machining holes into the couplings corresponding to holes in the motor support structure or the large aluminum carriage. Precision alignment pins were used to hold the couplings in place while they were clamped onto their respective shafts. The design of this mechanism allows the user to easily set the foil motion according to any of the discreet variables chosen. It is able to function in the presence of water. The frame and setup are as minimal as possible to allow for the greatest number of camera angles.

2.6 Motor Control

Three separate motors control the experimental apparatus. One motor is used for the pitch and the heave. One motor is used to control the lead screw at slow speeds and a separate motor is used to control the lead screw at high speeds.

As mentioned in the detail design section, the motor which controls pitch and heave is a 2 phase GBM stepping motor, product number 42BYG023, with a step angle of 1.8°. It was necessary to use a position controlled motor because torque varies throughout the cycle. A controller designed and built by MIT undergraduate Alex Hornstein runs the motor. The controller is programmed via serial port using ATOM Basic Pro. The program takes in Reynolds number and Strouhal number and computes the frequency at which the motor needs to operate. The motor functions at frequencies between 0.08 Hz and 2.25 Hz. A Strouhal number of $St=0.2$ at a Reynolds number of $Re=161.5$ is at the low end of the spectrum while a Strouhal number of $St=1.5$ and a Reynolds number of $Re=1000$ is at the high end of the spectrum. The Strouhal and Reynolds numbers listed correspond to the NACA 0030 foil of chord length c=19mm used throughout the experiments detailed in this thesis. Since the motor is a stepper motor, the program works by calculating the amount of time it needs to pause between steps. The stepper motor has no feedback, so it needed to be calibrated because

calculation time needs to be accounted for in the program. The motor is calibrated visually using the PIV system to determine the timing errors.

The stepper motor that controls the leadscrew at low speeds operates in a manner very similar to the motor that controls pitch and heave. It is a Superior Electric slo-syn stepper motor also controlled by Alex Hornstein's controller but programmed using ATOM Basic as opposed to ATOM Basic Pro. The program's only input is Reynolds number which is used to calculate operating frequency. The motor is calibrated using the same visual calibration method used for the heave and pitch motor. The maximum operating frequency is about 2 Hz which corresponds to a Reynolds number of about $Re=190$ for the foils studied in this thesis. Since this study required looking at Reynolds numbers up to $Re=1000$, a different motor, a Bodine Electric Company fractional horsepower gear motor, was used. The Bodine motor's minimum speed corresponded roughly to a minimum Reynolds number of $Re=200$, which is why it could not be used at the lower Reynolds numbers. Unlike the heave and pitch motor, this motor sees constant torque throughout the cycle, so a constant voltage DC motor was adequate. A Minarik controller with a hand dial determined the speed of the motor. The speed was calibrated using the same visual calibration technique used for the stepper motors.

Overall, the motor control was adequate for the experiments done in this thesis; however, it is recommended that for further experiments, the motors be upgraded to motors with feedback that could be controlled with a more used friendly system such as LabView.

2.7 Foil Construction and Mechanism Interface

The majority of the experiments in this thesis use NACA 0030 foils with a chord length of $c=19$mm and an aspect ratio of three. Several experiments were also performed using a trout tail shaped foil cut from a $^1/_{16}$" thick piece of stainless steel sheet metal. The construction of these foils as well as the mechanism that interfaces and aligns them with the experimental set up both required a significant amount of design.

NACA symmetrical airfoils are defined by the following equations:

$$x_n(x) = \frac{x}{c} \qquad \textit{Eq. 5}$$

$$y(x_n) = 0.5tc(0.2969x_n^{0.5} - 0.126x_n - .3516x_n^2 + 0.2843x_n^3 - 0.1015x_n^4) \qquad \textit{Eq. 6}$$

where x is the x component, c is the chord length, x_n is the normalized x component, y is the y component, and t is the foil thickness. For a four-digit NACA foil, the percent thickness is the last two digits. Therefore, for a NACA 0030 foil, t is equal to 0.3 and the foil's maximum thickness will be 30% of the chord length.

In order to construct the foils, molds were CNC milled out of aluminum blocks using ball end mills. These molds were bolted to a back plate. Also bolted to the back plate were aluminum parts which aligned a $^1/_8$" stainless steel shaft to the quarter-chord position of the foil since the foils in the experiments of this thesis are pivoted about the quarter-chord. The length of the shaft was chosen so that the foils would be submerged three foil heights to eliminate surface effects. Solid models of the mold set up are shown in figure 11.

This setup allowed the shaft to be molded into the foils. The NACA foils were constructed out of two materials, one rigid and one flexible. Rigid foils were molded out of epoxy resin. Prior to molding the foils, the molds were sprayed with mold release. The flexible foils were molded out of polyurethane. Photos of these foils are shown in figure 12.

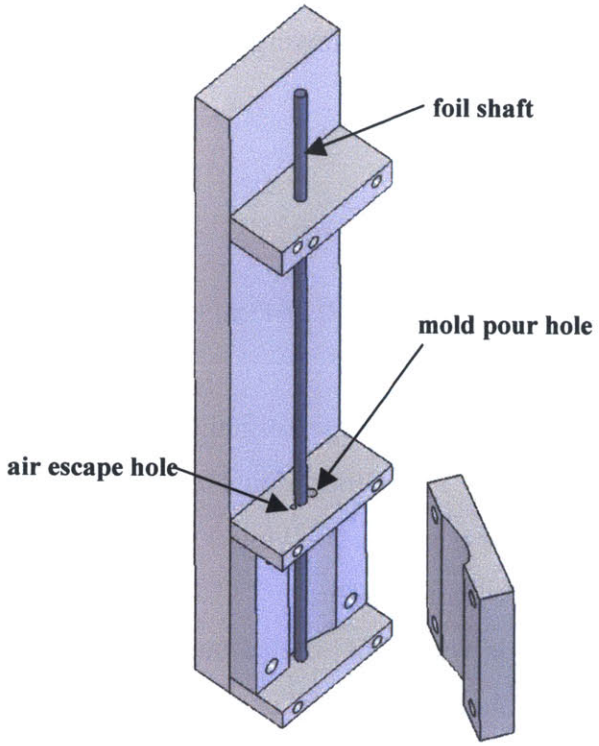

Figure 11: The mold setup for making foils. The shaft is aligned by the set up. Once the mold is bolted closed, the foil material is poured through the mold pour hole. There is a second smaller hole which allows air to escape from the mold.

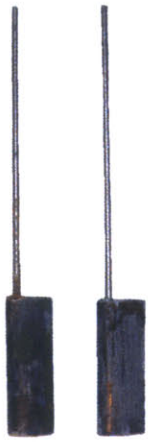

Figure 12: Photos of the NACA 0030 foils. The one on the left is made of epoxy resin, the one on the right is made of polyeurethene. The natural colors of the foils are white and pink respectively but both were dyed black to prevent light diffusion during PIV.

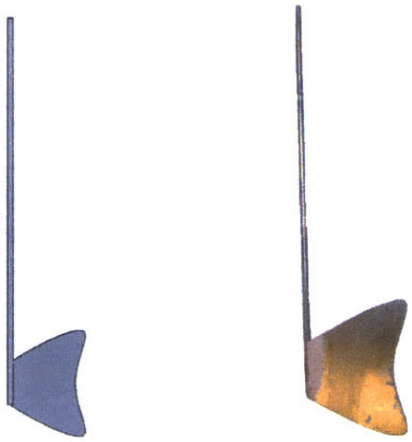

Figure 13: Stainless steel trout tail foil. The image on the left is the solid model, the image on the right is the actual foil used.

The trout tail foil was made in a very different manner from the NACA foils. A profile of a trout tail was drawn based on the drawing in Videlar (1993). A DXF file was made from this drawing and it was cut out of a piece of $^1/_{16}$" stainless steel sheet metal using a waterjet cutter. The sides of the foil were filed and sanded. A $^1/_{16}$" slot of depth $^5/_{64}$" was milled into the end of a $^1/_8$" stainless steel rod. The length of the slot was the same as the length of the front edge of the foil. The foil was welded into the slot. The transition region between the rod and foil was filled with Bondo© and sanded until smooth. A solid model and photo of the trout tail foil are shown in figure 13.

A magnetic interface is used to quickly align and attach the foil to the experimental setup. Since the foils are extremely light, a very small magnet is used to hold them in place. The foil is aligned with a hexagonal keyway mechanism. A rigid aluminum coupling links a piece of steel hex shaft to the heaving and pitching stainless steel shaft descending from the heave and pitch mechanism. This interfaces with an alignment collar placed on the top of the foil shaft. The alignment collar consists of an acrylic cube with a hexagonal hole broached in it. At the end of the hexagonal hole is a magnet. This keyway is attached to an aluminum rectangle with a $^1/_8$" hole in it. In order to attach the foil to the alignment collar, the foil is bolted into the original CNC molds. The top of the foil shaft is placed in the $^1/_8$" hole in the alignment collar. The collar is then bolted to the back plate of the mold. A set screw is tightened to hold the foil square to the alignment collar. The foil and alignment collar are then unbolted.

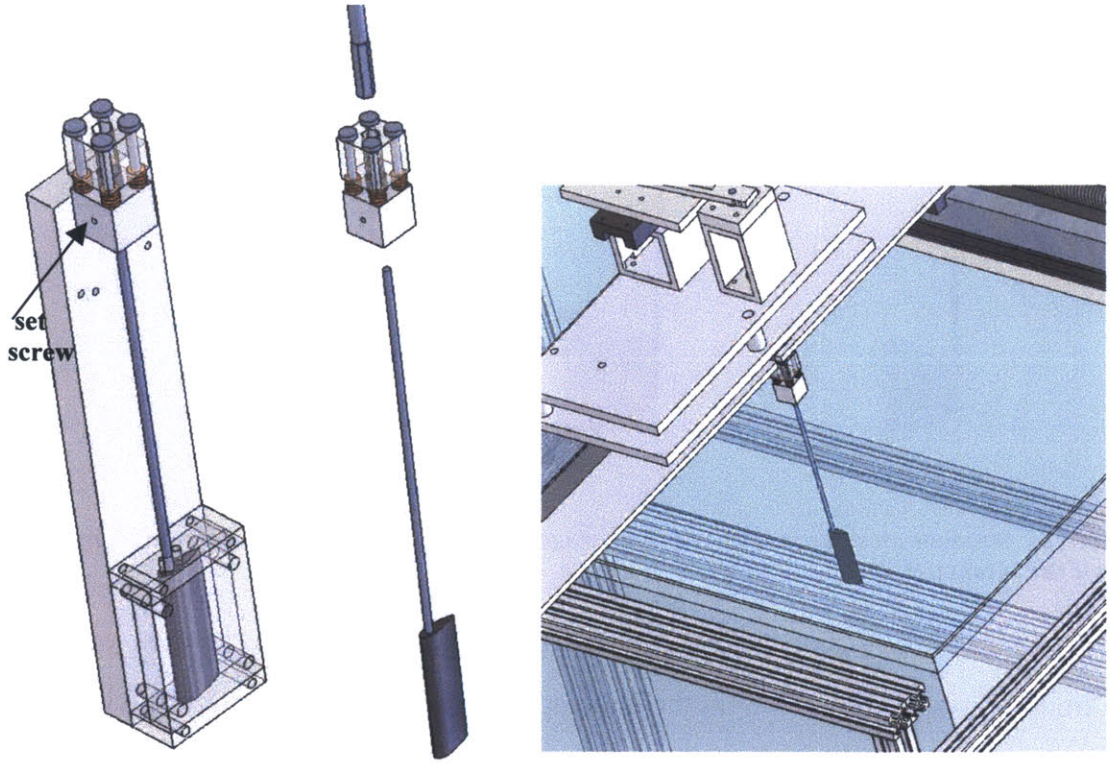

Figure 14: Magnetic alignment mechanism. The image on the left shows how the foil is aligned to the mechanism using the pre-existing molds. The center image shows a broken out assembly. The right image shows the magnetic alignment mechanism in the context of the rest of the apparatus.

The alignment collar interfaces with the machine by sliding the steel hex rod on the heave and pitch mechanism into the broached acrylic. Since steel is magnetic, it snaps to the magnet inside the collar. In this way, it is possible to quickly align and attach foils to the mechanism in a repeatable manner. The initial alignment of the steel hex shaft to the machine was done visually using a high precision camera. Photos of the alignment mechanism are shown in figure 14.

2.8 Apparatus Summary

This apparatus was used in all the subsequent experiments described in this thesis. The heaving and pitching motion obtained was very smooth and simple to control due to the one motor design. However, the many linkages in this mechanism made it difficult to calibrate and characterize the error. It is recommended that future iterations of the design

use two separate motors along with feedback control for increased accuracy and flexibility.

Chapter 3

Fluorescent Dye Visualizations

3.1 Overview

The three-dimensional shape of flapping foil wakes is notoriously hard to determine. It is possible to do with numerical methods but requires a large amount of computing power. Particle image velocimetry can provide three-dimensional flow fields, but only in two-dimensional planes, so creating an entire flow field requires taking data in slices and piecing them together. Dye visualization offers a way to qualitatively look at the entire flow field without having to do multiple experiments and without using computationally heavy numerical methods.

Dye visualization is valuable for several reasons. First, it allows for a simple way to look at wake morphology. Wake morphology is a good way to compare different situations. If two foils have similar wakes, chances are the fluid dynamics involved in both flows are similar. This similarity is very important for the ultimate goal of this thesis, determining the scalability of flapping foil dynamics. Dye visualizations are also a good way to quickly determine how three-dimensional a flow is. In the later PIV experiments, overall thrust is estimated by the flow field at the mid plane of the foil. Knowing qualitatively how three-dimensional the wake is allows one to get a feel for the accuracy of the two-dimensional thrust approximation. The dye visualizations presented in this chapter provide excellent insights into the wake morphology and the extent to which three-dimensional effects are a factor.

3.2 Prior Dye Visualizations

Multiple methods of dye visualization have been evaluated. The goal of dye visualization is to provide a comprehensive three-dimensional qualitative representation of the wake behind a flapping foil. This must be done without changing the fluid dynamics of the flow. This section discusses two different types of flow visualizations previously used as well as the benefits and detriments of each.

Some of the earliest work done on visualization of flapping foil wakes was done not in water, but in air. Freymouth (1989) performed visualizations on flat wings of rectangular and triangular shapes in an air tunnel. The forward speed of air was 610 mm/s. Liquid titanium tetrachloride was applied uniformly to the surface of the wing. The $TiCl_4$ coating caused white fumes to tag the air that had been in contact with the foil, where vorticity is produced. By this method, Freymouth (1989) was able to view the vortical structures behind the airfoil. The images were taken in the planform view and captured with a camera at a frame rate of 64 frames per second [Freymouth, 1989]. One of these flow visualizations is shown in figure 15. Although the Freymouth (1989) images are not of exceptionally high quality, the method is promising. The idea of uniformly coating the surface of the foil carries over into the domain of water because it offers the benefit of ensuring that all of the fluid that comes into contact with the foil is marked.

von Ellenrieder *et al.* (2003) performed dye visualizations on a rigid NACA 0030 symmetric airfoil of chord length $c=19$mm and an aspect ratio of three. Reynolds number was held constant at $Re=161.5$, which corresponds to a forward velocity of $U=8.5$mm/s. The experiments were performed in a recirculating water tunnel. The parameters varied were Strouhal number, maximum pitch angle, and phase shift between heave and pitch. The values of these parameters are listed in table 2. The foils used were hollow with 0.9mm holes positioned every 2mm along the leading edge from which fluorescent dye was injected during the experiment. The dye flow was controlled by a needle valve. The dye reservoir was a bottle approximately 1 m above the foil. The foils were pitched about the quarter-chord by a hollow shaft that also served as the dye supply

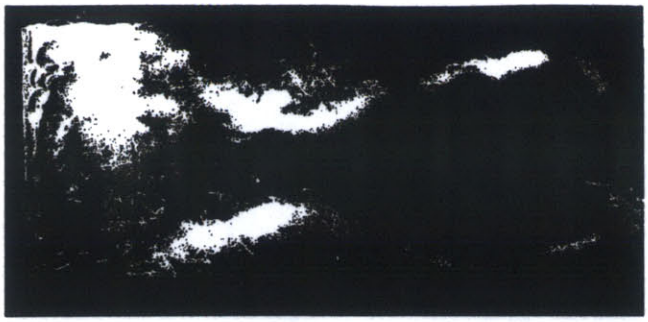

Figure 15: Dye visulazation on a flapping foil in an air tunnel [Freymouth, 1989].

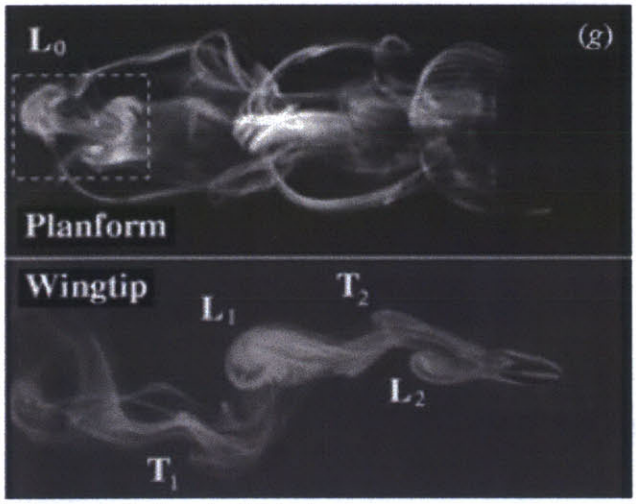

Figure 16: A representative image from the von Ellenrieder *et al.* (1998) flow visualization experiments.

line. Video of the foils was taken from both a planform and wingtop view using two CCD cameras with frame rates of 25 frames per second [von Ellenrieder *et al.*, 2003]. One of these flow visualizations is shown in figure 16.

One concern when using this type of approach is that since the dye is entering the flow with some velocity, momentum is being added to the system and could be altering the flow. Another potential problem with this approach is the large size of the dye distribution holes; they take up nearly half of the leading edge of the foil. A sketch of the von Ellenrieder *et al.* (2003) observed morphology of the wake is shown in figure 17. von Ellenrieder *et al.* (2003) describes the vortical structures as "ring like structures with a bulbous head....and two filamentary arms." von Ellenrieder *et al.* (2003) proposed that the dual arms are the result of leading-edge separation, which joins the trailing edge vorticity to form one multi-filament vortical structure. These secondary filamentary arms

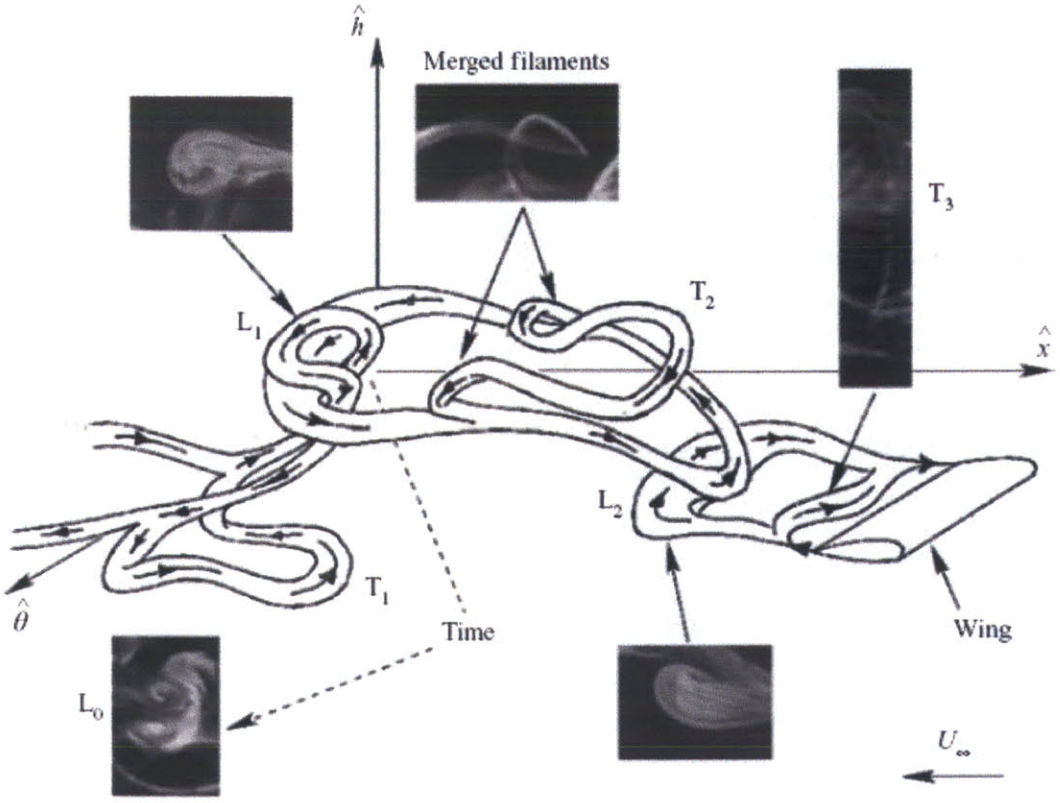

Figure 17: von Ellenrieder *et al.* (2003) proposed wake morphology.

had not been seen in any of the literature prior to these visualizations.

Since the Freymouth (1989) method does not involve adding momentum to the system and does not involve putting holes in the surface of the foil, it was considered more appealing than the von Ellenrieder *et al.* (2003) method. Therefore this thesis uses a similar method, but instead of using $TiCl_4$, the surface of the foils is coated with a fluorescent dye. This method is detailed in the following section.

3.3 Experimental Setup and Method

Before performing any dye visualizations, a dye, which would shed off the foil in a manner that allowed clear visualizations and did not interfere with the dynamics of the flow, had to be developed. A water soluble fluorescing agent was chosen as the marker

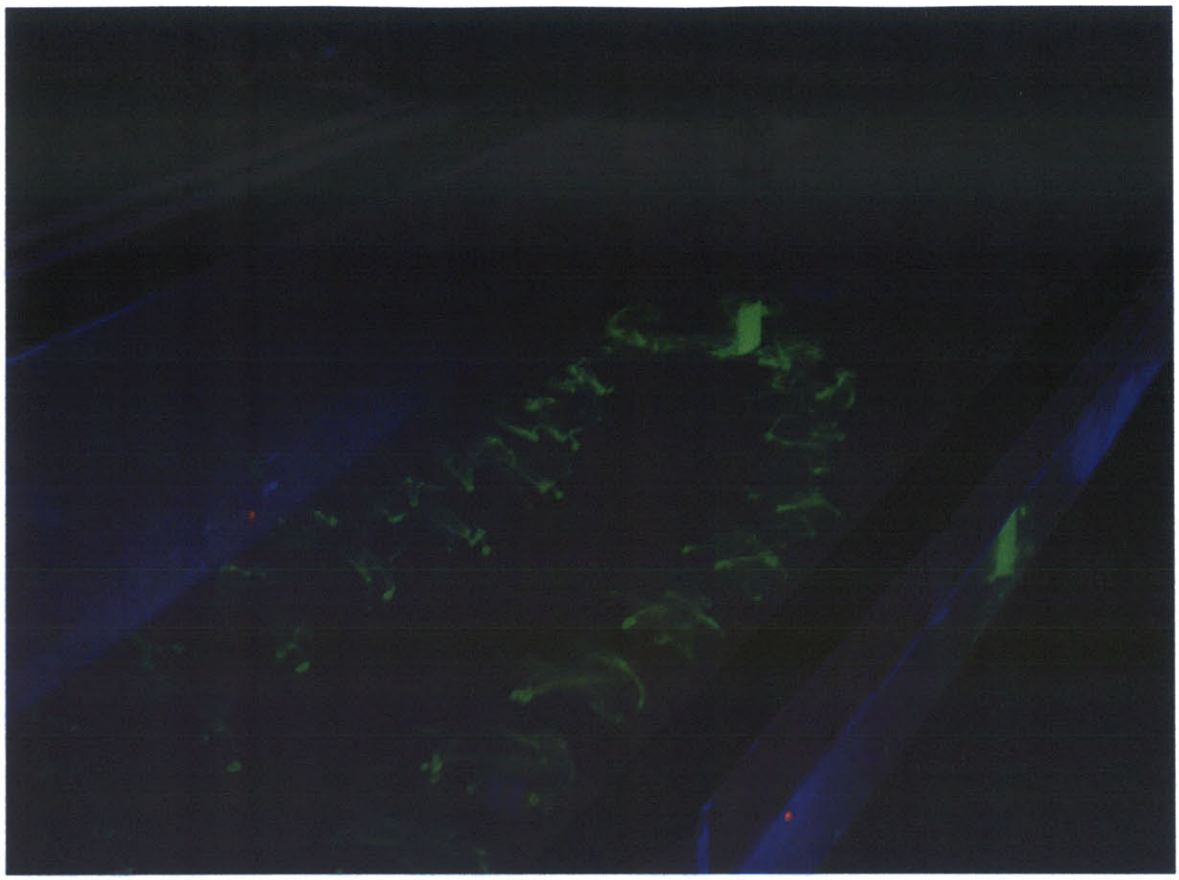

Figure 18: An image of the fluorescent dye in water after a run illustrating its neutral buoyancy.

because it could be used under a standard black light. When placed in water by itself, this dye diluted far too fast to be useful. It also had no way of attaching to the surface of the foils. Two undergraduate students, Matthew Krueger and Cha Ling O'Connell, experimented adding various thickening agents to the dye. They came up with a mixture of 1 volume part dye to 8 volume parts Elmer's glue. This mixture could be painted onto the foils. Since the foils are painted by hand, there is some variability with regard to the evenness of the application. The effect of this has not been studied. Once dried, the foils could be placed in water. If held still, the dye remained on the foil. When the foil was moved through the water, the dye shed gradually. The dye/glue mixture also had a density approximately equal to water, as shown by the photograph in figure 18. The photograph in figure 18 was taken approximately three minutes after the foil had completed a heaving and pitching run. If the water is not disturbed, the dye remains in the same position for tens of minutes. Unfortunately, the dye only exhibited these desired

properties at low Reynolds numbers of $Re \leq 300$. At higher Reynolds numbers, the dye diffused too fast, clouding the entire tank.

Due to this upper limit, the visualizations performed were limited to those performed in von Ellenrieder *et al.* (2003), varying Strouhal number, maximum pitch angle, and phase shift between heave and pitch while keeping Reynolds number constant at $Re=161.5$. Strouhal number, maximum pitch angle, and phase shift were varied according to the values listed in table 2. These values are also appealing because Blondeaux *et al.* (2005) had run CFD simulations for several of these scenarios, therefore the data would be able to be confirmed by a source independent of the von Ellenrieder *et al.* (2003) visualizations. This is important because of the aforementioned concerns regarding the von Ellenrieder *et al.* (2003) techniques. Both the epoxy resin and polyurethane NACA 0030 foils of chord length $c=19$mm and aspect ratio three were tested to determine what effect foil flexibility had on the wake dynamics. The motion of the foils is described by equations 1 and 2 and implemented by the mechanism described in chapter 2. Two black lights were mounted to the 80/20 frame. When the experiments were run, all other lights were turned off and the blacklights were the only source of light. The foil was visible at all times because it was completely coated with the dye. Video of each of the runs was obtained with a Canon GL2 digital video camera at a frame-rate of 30 frames per second. The spotlight feature was used so that the camera would automatically focus on the illuminated wake and foil. When planform data was being obtained, the camera was placed on a tri pod to the side of the tank. When wingtip data was being obtained, the video camera was mounted under the tank. This set up is shown in figure 19.

Six foils were rotated during the experiments. As soon as one was used, the remaining dye was washed off and it was repainted so that it would be dry the next time it came up in the rotation. The tank was drained between every run. After the tank was filled, the water was allowed to rest for at least five minutes before another run was performed. If the water was visibly not still, the next run was not performed until it had settled. In addition to videotape of the foils being taken, still photos were also taken with a Sony Cybershot digital camera. Since this camera had significantly better resolution than the video camera, the images taken were much clearer. Still images were taken from

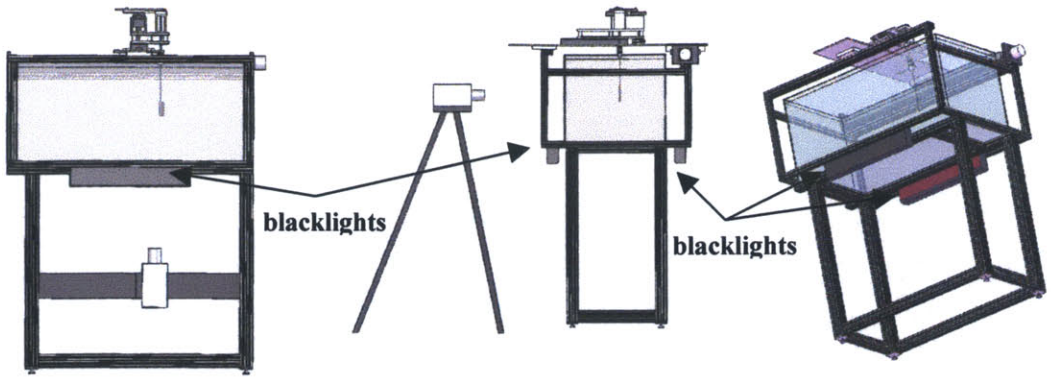

Figure 19: Experimental set up for the dye visualizations. The image on the left shows where the camera is set up for taking wingtip data. The center image shows where the camera is mounted for taking planform data. The image on the right shows a view from underneath the apparatus with the blacklights mounted to the frame but with no cameras.

a planform, wingtip, and isometric view. The photographer held the camera and the images were triggered manually, so unfortunately most of the images taken cannot be phase synched and the angles they are taken from are not identical. They do however provide a very high quality visual representation of the wake morphology. Both the still images and those taken from the video camera are shown in the following section.

It should be noted that this same method and apparatus are used in Krueger (2005). Krueger (2005) used were polyurethane foils and pitched them about the three-tenths-chord as opposed to the quarter-chord.

3.4 Dye Visualization Images.

Dye visualizations were performed on both rigid epoxy resin foils and flexible polyurethane foils. The Reynolds number was kept constant at $Re=161.5$ and Strouhal number, maximum pitch angle, and phase shift between heave and pitch were varied. Still images were taken from planform, wingtip, and isometric views of each of these cases using both the rigid and flexible foil. These results are shown in figures 20 through 25. Once again it should be noted that it was not possible to phase sync these pictures. Since the camera was held by hand, not all the pictures are at the exact same angle. Also the quality of the pictures varied because of the shakiness associated with hand held photography.

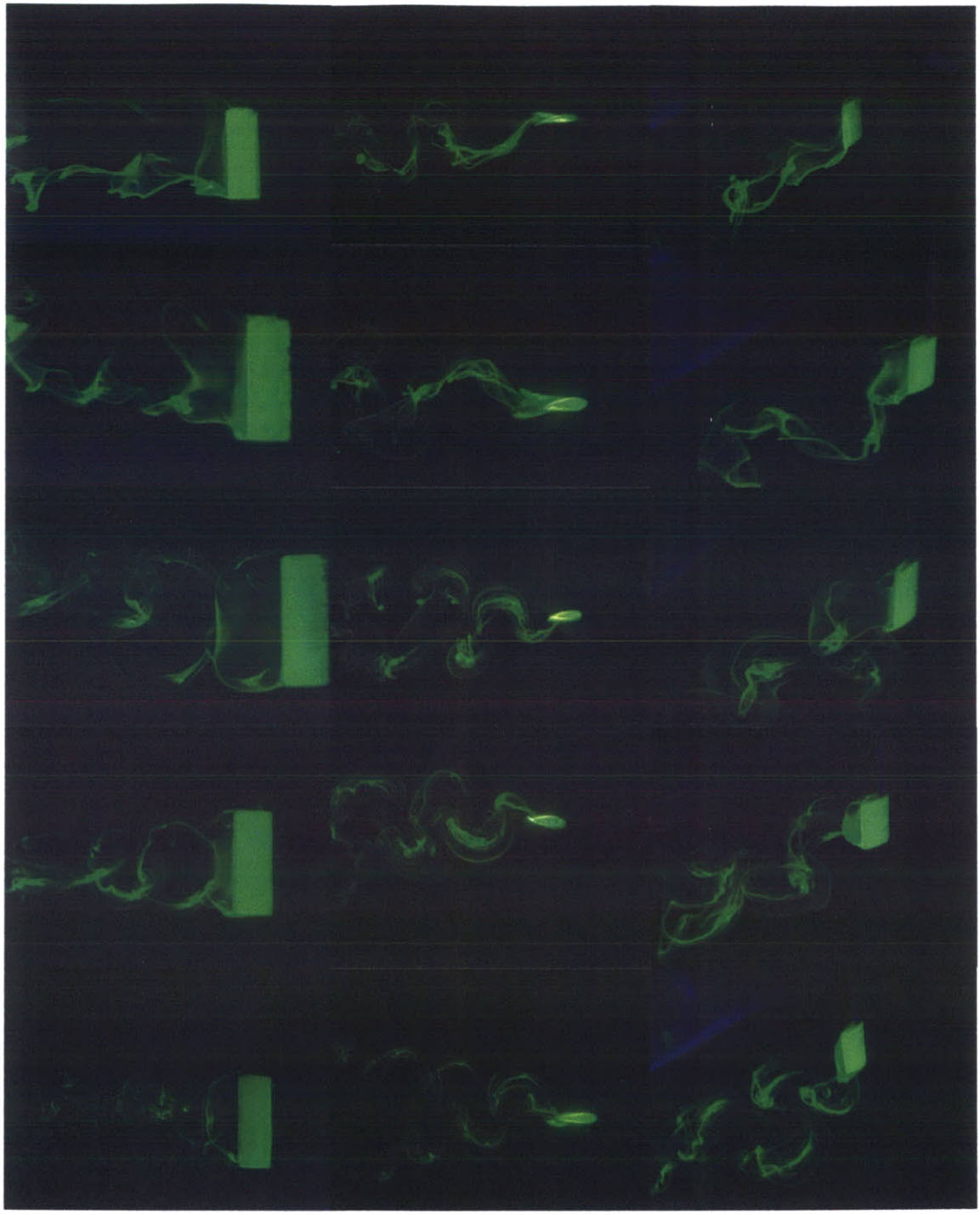

Figure 20: Planform, wingtip, and isometric views of a rigid foil at *Re=161.5, θ_o=5°, Φ=90°* as Strouhal number is increased. From top to bottom the Strouhal numbers shown are *St=0.2, 0.25, 0.3, 0.35*, and *0.4*.

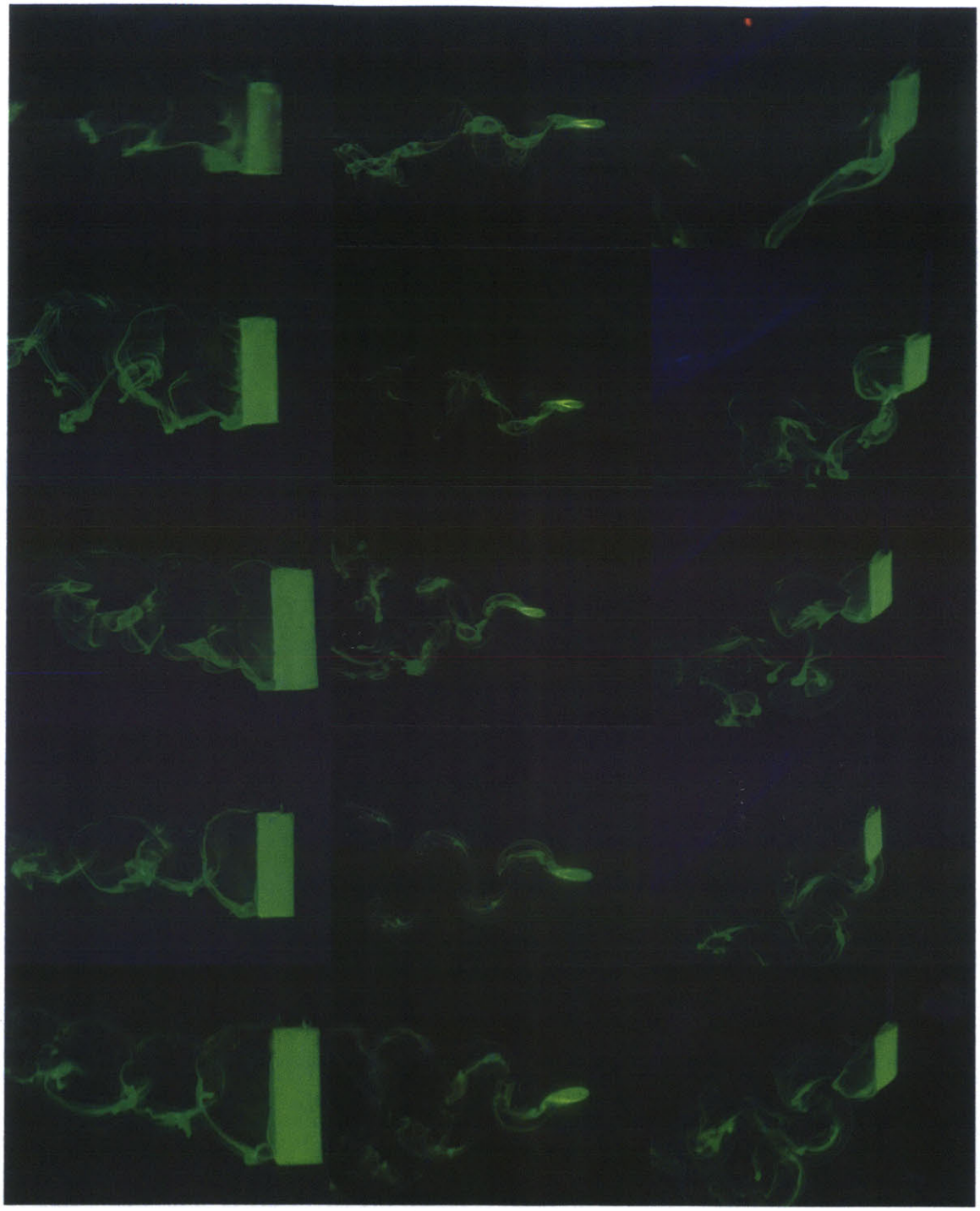

Figure 21: Planform, wingtip, and isometric views of a flexible foil at *Re=161.5*, θ_o*=5°*, Φ*=90°* as Strouhal number is increased. From top to bottom the Strouhal numbers shown are *St=0.2, 0.25, 0.3, 0.35,* and *0.4.*

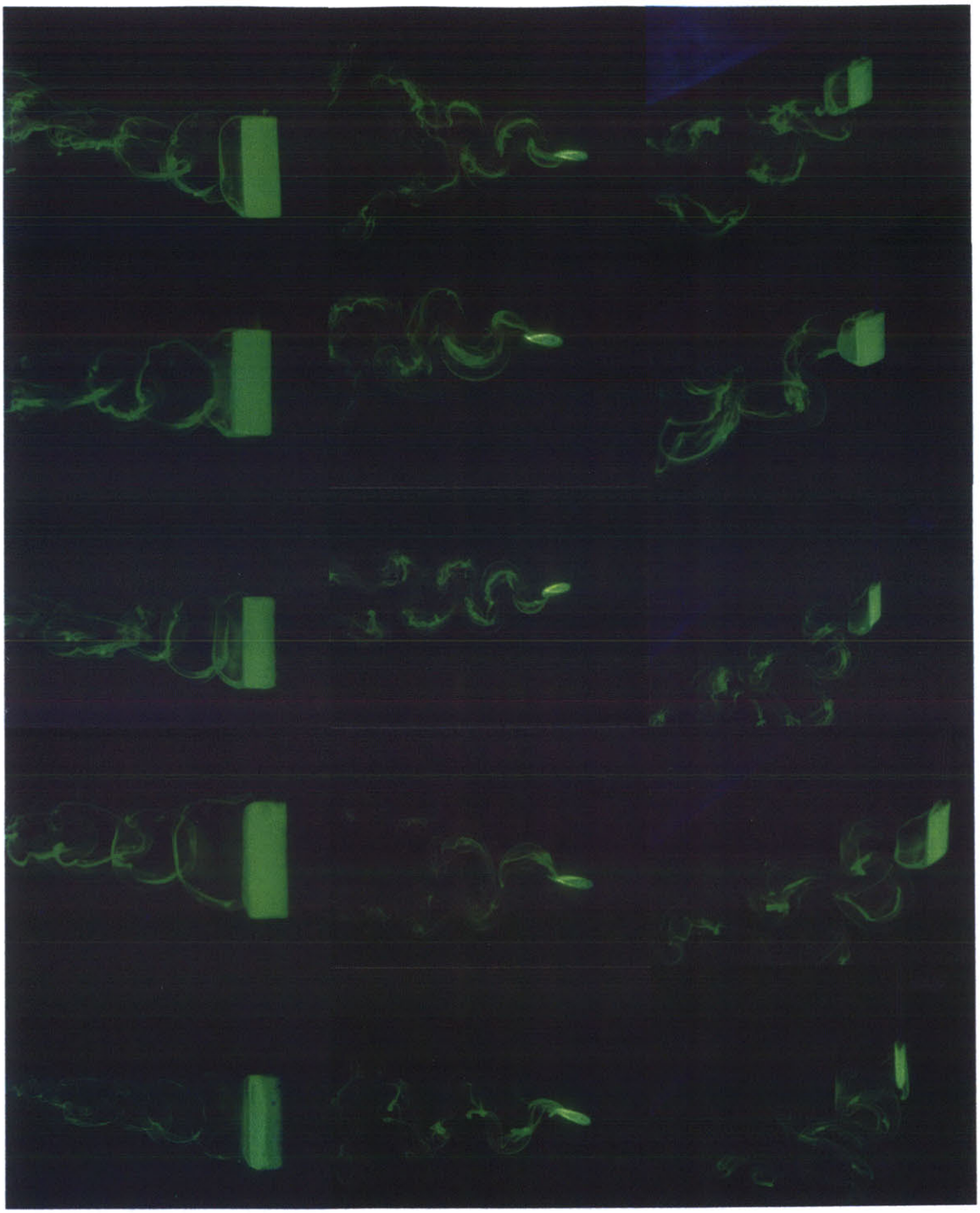

Figure 22: Planform, wingtip, and isometric views of a rigid foil at *Re=161.5, St=0.35, Φ=90°* as maximum pitch angle is increased. From top to bottom θ_o = *0°, 5°, 10°, 15°,* and *20°*.

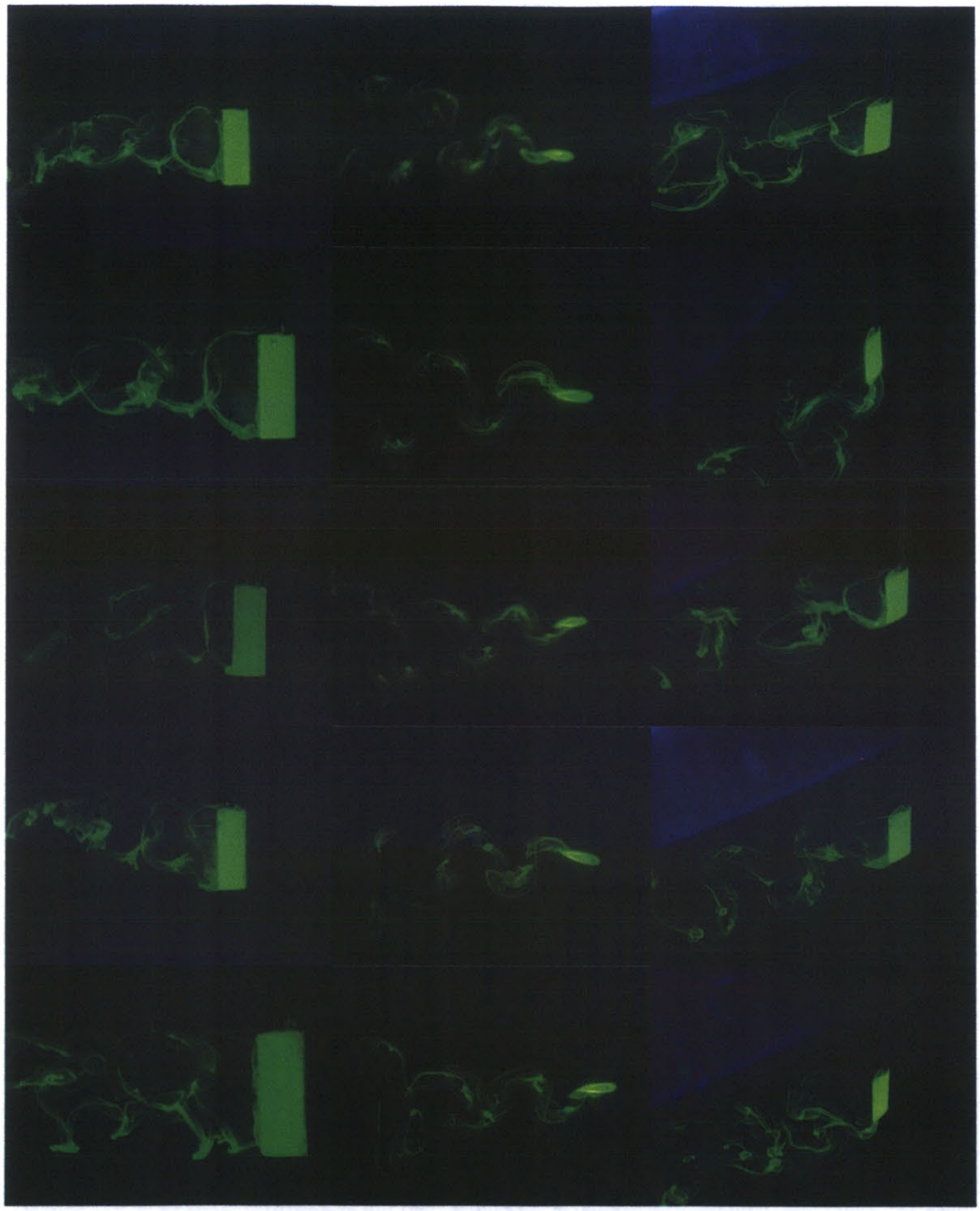

Figure 23: Planform, wingtip, and isometric views of a flexible foil at *Re=161.5, St=0.35, Φ=90°* as maximum pitch angle is increased. From top to bottom θ_o= 0°, 5°, 10°, 15°, and *20°*.

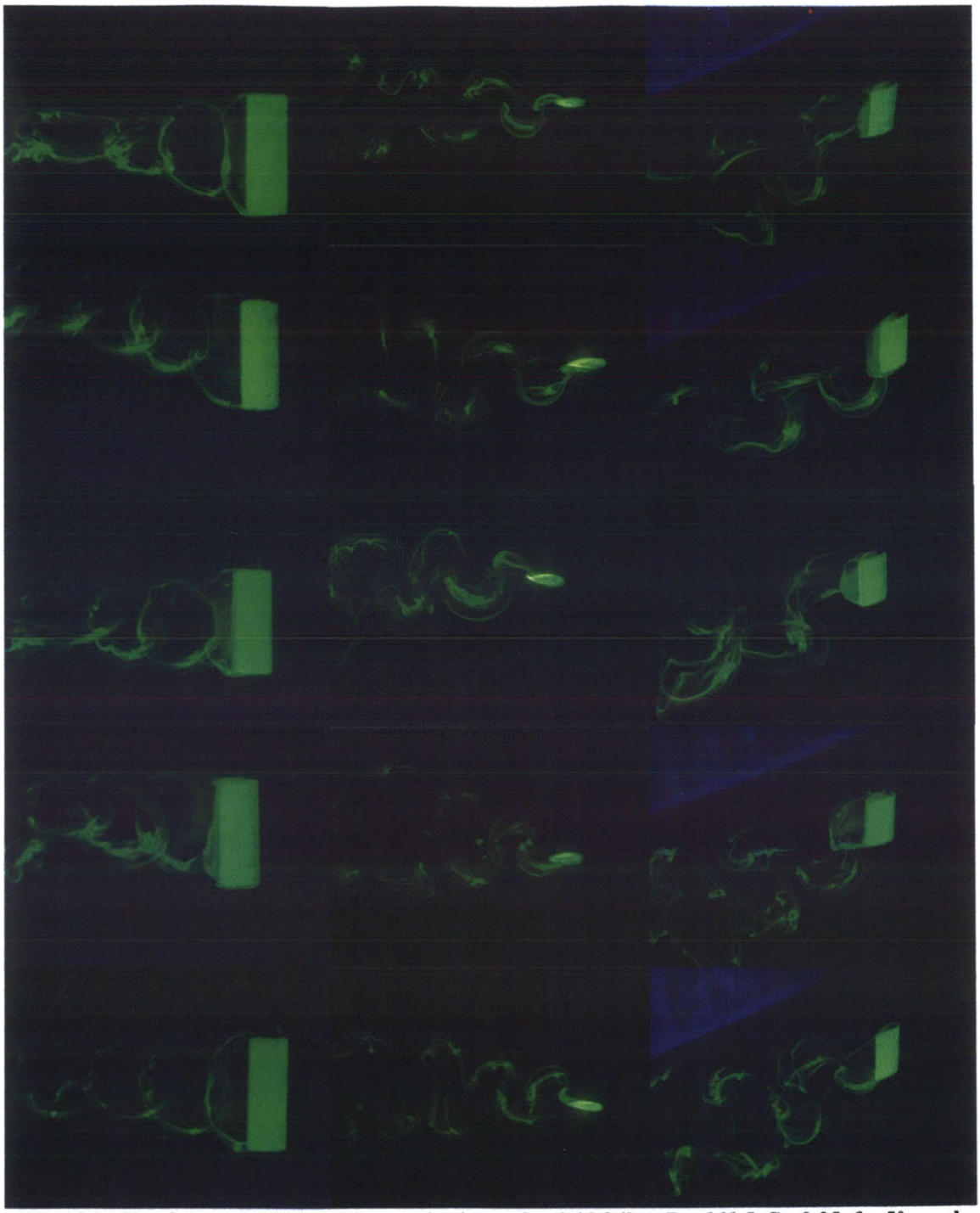

Figure 24: Planform, wingtip, and isometric views of a rigid foil at *Re=161.5, St=0.35, θ_o=5°*, as phase shift between heave and pitch is increased. From top to bottom *Φ= 60°, 75°, 90°, 105°*, and *120°*.

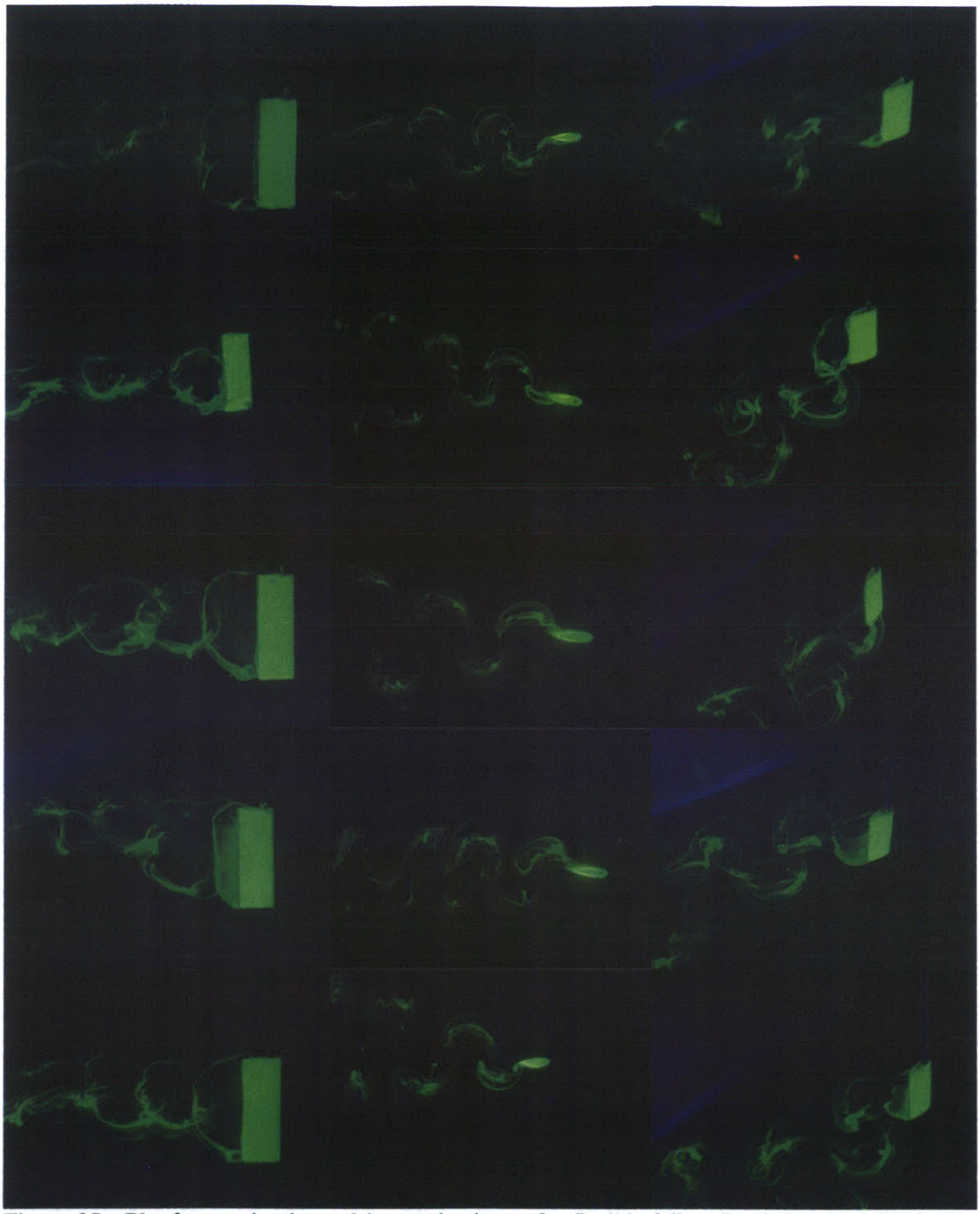

Figure 25: Planform, wingtip, and isometric views of a flexible foil at *Re=161.5, St=0.35, θ_o=5°*, as phase shift between heave and pitch is increased. From top to bottom *Φ= 60°, 75°, 90°, 105°*, and *120°*.

For the rigid foil, at the lower Strouhal numbers, the vortical structures arrange themselves in an 'S' shaped wake. As Strouhal number increases, the wake develops more distinct individual horseshoe-like vortical structures. The results from increasing Strouhal number for the flexible foil are nearly identical to the results seen in the rigid foil. However, it should be noted that at these low Strouhal and Reynolds numbers, there was no visible deflection of the foil. Therefore it is not surprising that the results are so similar. Once again an 'S' shaped wake is seen at the lower Strouhal numbers and a wake with distinct horseshoe-shaped vortices is seen at the higher Strouhal numbers.

As maximum pitch angle increases, the wake of the rigid foil appears to get slightly wider. This makes sense because the trailing edge of the foil sweeps a larger area. The horseshoe like vortical structures also appears to be getting longer, though it is difficult to be certain because of the large variation in photo quality and vantage point. The $\theta_o=0°$ case looks quite a bit different than the rest. In the other cases, the pitch angle changes so the overall change in angle of attack is smaller and happens slower than it does in $\theta_o=0°$ case. The rapid change in angle of attack in the $\theta_o=0°$ case might explain why the wake of that instance looks more turbulent than the others. As with increasing Strouhal number, the flexible foil results for increasing maximum pitch angle are not significantly different than those for the rigid foil. The rigid foil dye visualizations seemed to be of slightly higher quality. This can be attributed to the dye adhering more readily and evenly to the rigid foil.

The variation in phase shift between heave and pitch for the rigid foil appears to change the width of the wake. The wake seems to be widest at the $\Phi=90°$ case and increasingly thinner as the phase shift moves away from $\Phi=90°$ in either direction. However, due to the variation in quality and vantage points of the photos, it is difficult to say for sure if the wake is indeed changing width with phase shift. The results of increasing the phase shift on a flexible foil also suggest that a maximum wake thickness is achieved at $\Phi=90°$. Since a straight line of ideal vortices behind a foil would produce no thrust, it is proposed that having a wider wake, such as the one generated a phase shift close to $\Phi=90°$, would result in a higher thrust. Guglielmini and Blondeaux (2004) verifies that the ideal phase shift is $\Phi=90°$. This also implies that the other cases that

generate a large wake, such as the higher Strouhal number and higher maximum pitch angle cases, would also result in higher thrusts.

3.5 Qualitative Comparison to Prior Visualization and CFD

The main difference between the imaged obtained by von Ellenrieder *et al.* (2003) and those obtained in the visualizations performed in this thesis, was that von Ellenrieder *et al.* (2003) sees a secondary filamentary arm absent from these results. It is proposed that the filamentary arm is the result of adding momentum into the system via the dye or that the holes along the leading edge disrupted the flow. However, the argument could just as easily be made that adding a viscous dye into the boundary layer casts doubt on the results of this thesis. Therefore, this discrepancy needs to be resolved by comparing the data with that of a third party. Blondeaux *et al.* (2005) ran a CFD simulation at a Reynolds number of $Re=164$, Strouhal number of $St=0.35$, maximum pitch angle of $\theta_o=5°$, and a phase shift between heave and pitch of $\Phi=90°$. Planform, wingtip, and isometric views are presented from this numerical study and directly compared to the flow visulazations. Also, in order to eliminate concerns that the properties of the dye interfere with the flow, PIV was also performed on foils under these same conditions. Those results are also compared to the numerical results of Blondeaux *et al.* (2005) in chapter 4. This section also discusses the results of other visualizations that aren't directly comparable. Images from the 30 frames per second camera were used to compare the flow visualizations to the CFD. These images, which are lower quality than the stills, were chosen because it was possible to match the phase of the images with the phase of the numerical simulations. Figure 26 shows the wingtip view of the dye visualizations and the numerical results at phases $\tau=0$, $\pi/4$, $\pi/2$, and $3\pi/4$. The numerical results are shown in the form of isosurfaces.

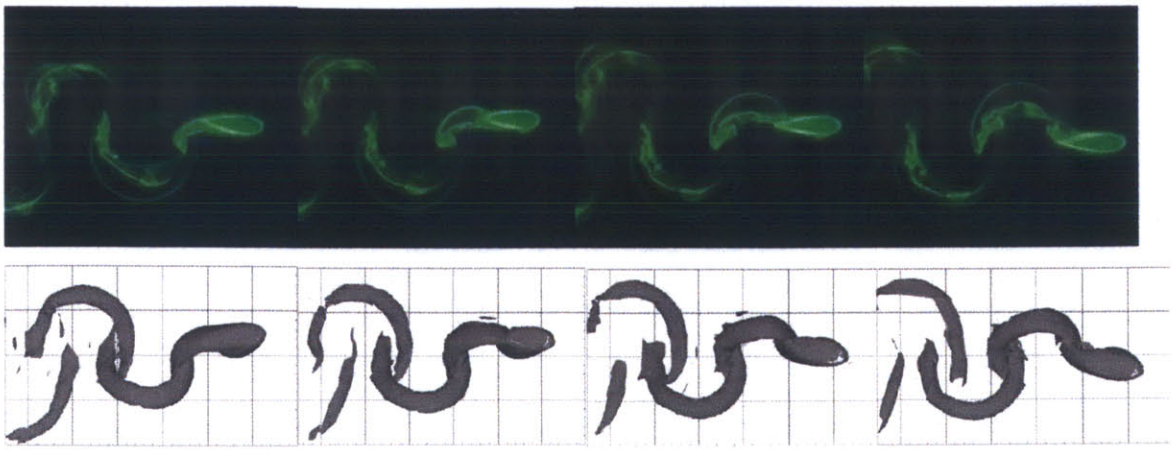

Figure 26: Wingtip comparison between dye visualizations and CFD isosurfaces from Blondeaux *et al.* (2005). For the dye visualizations $Re=161.5$, $\theta_o=5°$, $\Phi_o=90°$, and $St=0.35$. For the CFD $Re=164$, $\theta_o=5°$, $\Phi_o=90°$, and $St=0.35$. From left to right $\tau=0$, $\pi/4$, $\pi/2$, and $3\pi/4$.

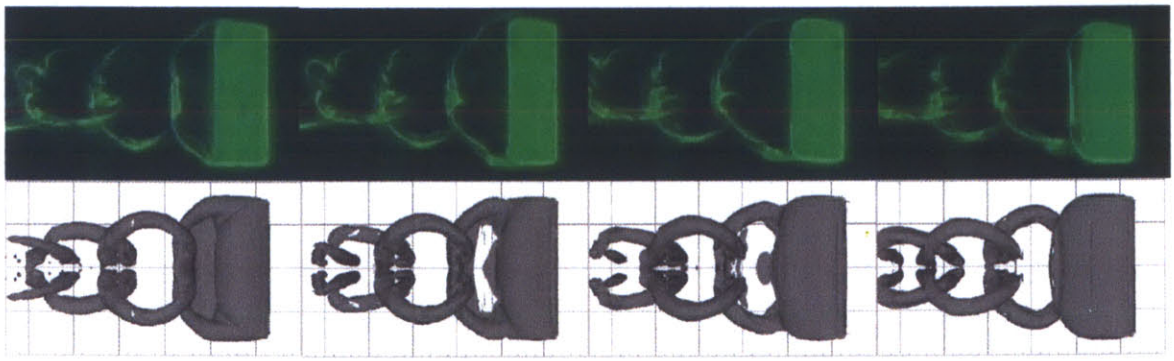

Figure 27: Planform comparison between dye visualizations and CFD isosurfaces from Blondeaux *et al.* (2005). For the dye visualizations $Re=161.5$, $\theta_o=5°$, $\Phi_o=90°$, and $St=0.35$. For the CFD $Re=164$, $\theta_o=5°$, $\Phi_o=90°$, and $St=0.35$. From left to right $\tau=0$, $\pi/4$, $\pi/2$, and $3\pi/4$.

The match up between the experimental and numerical results is excellent. The size and shape of the vortical structures are very similar. The area around the foil shows no evidence of leading edge separation as proposed by von Ellenrieder *et al.* (2003). Comparison between the planform views of the same case as the wingtip views is shown in figure 27.

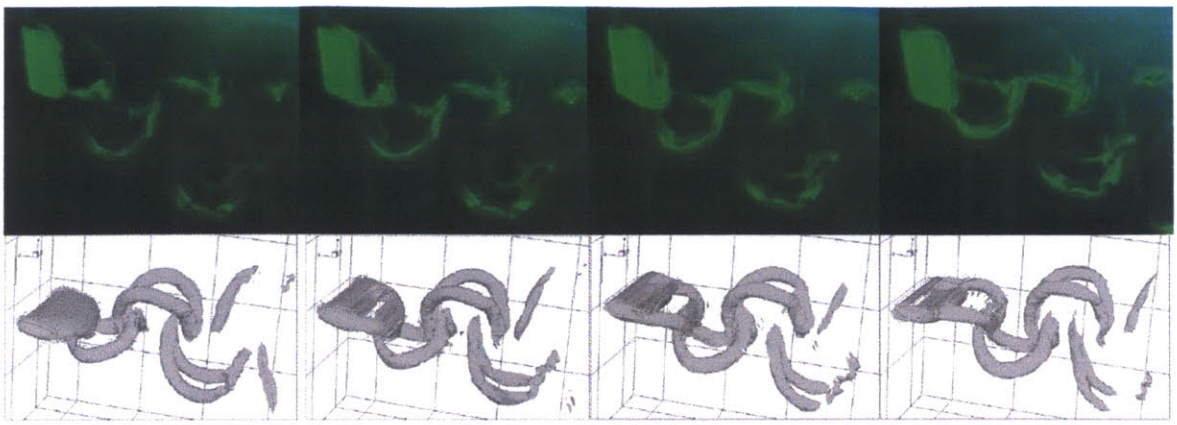

Figure 28: Isometric comparison between dye visualizations and CFD isosurfaces from Blondeaux *et al.* (2005). For the dye visualizations $Re=161.5$, $\theta_o=5°$, $\Phi_o=90°$, and $St=0.35$. For the CFD $Re=164$, $\theta_o=5°$, $\Phi_o=90°$, and $St=0.35$. From left to right $\tau=-\pi/2$, $-\pi/4$, 0, and $\pi/4$.

As with the wingtip view, the planform view shows excellent agreement between the experimental and numerical results with regard to the size and shape of the vortical structures. This view also does not show any evidence of a secondary filamentary arm. This is further confirmed by the isometric view, shown in figure 28.

Unfortunately, the isometric numerical data is not presented at the same angle as the experimental data. However, qualitative comparisons can still be made. Both exhibit the horseshoe-like vortical structures discussed in the pervious section of the chapter. The structures are of similar size and shape. The morphologies proposed by Blondeaux *et al.* (2005), von Ellenrieder *et al.* (2003), and this thesis are shown side by side in figure 29.

The morphologies proposed by the numerical method and by the experiments performed in this thesis are very similar. Both show simple horseshoe-shaped single-filament vortical structures.

Determining the wake morphology is important for several reasons. First, it allows comparisons regarding the dynamics of other foils to be made. Foils at higher Reynolds numbers or Strouhal numbers whose wake looks similar to the one shown in figure 29 most likely have similar fluid dynamics. This scalability is incredibly useful because the cost of computing solutions to faster situations is far too high to be practical. The second reason these visualizations are important is that they allow qualitative

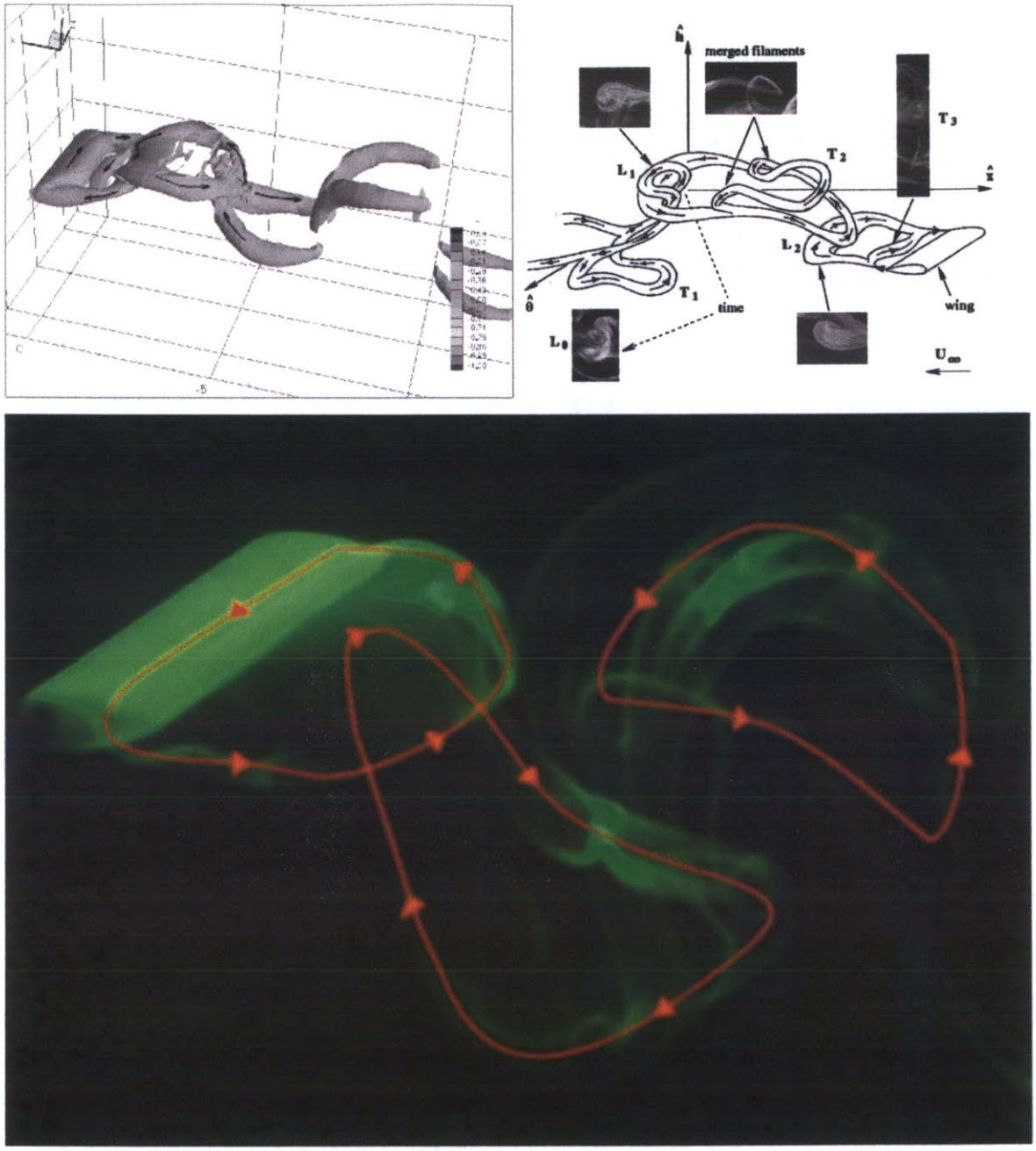

Figure 29: Three different proposed wake morphologies. The upper left image is from Blondeaux *et al.* (2005). The upper right image is from von Ellenrieder *et al.* (2003). The third is the morphology seen in the fluorescent dye visualizations.

statements to be made the accuracy of computing thrust from a two-dimensional mid-plane PIV slice. The visualizations show that this flow is very three-dimensional. The majority of the vorticity seems to be concentrated near the mid-plane. Therefore it can be hypothesized that by estimating thrust using mid-plane data most likely overestimates the overall thrust. However, since these foils are symmetric about the mid-plane, the vorticity is most likely to be concentrated in the mid-plane for all cases. Therefore, while two-dimensional thrust estimates are not ideal from an absolute quantitative view, they will be adequate for direct comparisons.

Overall, the quality of the visualizations obtained from these experiments far surpasses any other method previously seen. The results have been used to determine the wake morphology for the low Strouhal number, low Reynolds number cases presented. Some concerns remain as to whether or not the properties of the dye change the flow. These concerns are addressed in chapter 4 by using particle image velocimetry to confirm these results without using any dye. The only disappointment is that the dye cannot be used in situations with higher tangential speeds. Since it is thought that high tangential speed is what causes rapid dilution of the dye, it may be possible to study other morphologies by changing the size of the foil but running it at the same speed. In this manner, other Reynolds numbers could be investigated while still operating in the narrow window of tangential speeds where the dye provides clear visualizations.

Chapter 4

Particle Image Velocimetry at Low Reynolds and Strouhal Numbers

4.1 Overview

Particle image velocimetry (PIV) is a technique that non-invasively measures the flow field of a two-dimensional slice of a fluid. This allows for a relatively simple way to measure the characteristics of the wake of a flapping foil. This can be used to determine thrust and hydrodynamic efficiency of a flapping foil used for propulsion. Determining these values is key to outlining scaling characteristics for flapping foil propulsion, which is the aim of this thesis. This chapter overviews the PIV technique looks at relevant previous studies, details the calculations used to determine relevant parametesr, and presents the results of PIV performed on foils for the cases discussed in chapter 3. These results are then compared to numerical results as well as the dye visualizations. A more detailed description of the technique can be found in Raffel *et al.* (1998).

4.2 Particle Image Velocimetry

The thrust generated by a foil can easily be calculated if the velocities in the wake are known. PIV is a quick and simple way to measure these velocities. Planar PIV looks only at two-dimensional velocity vectors within a two-dimensional field. A laser sheet is

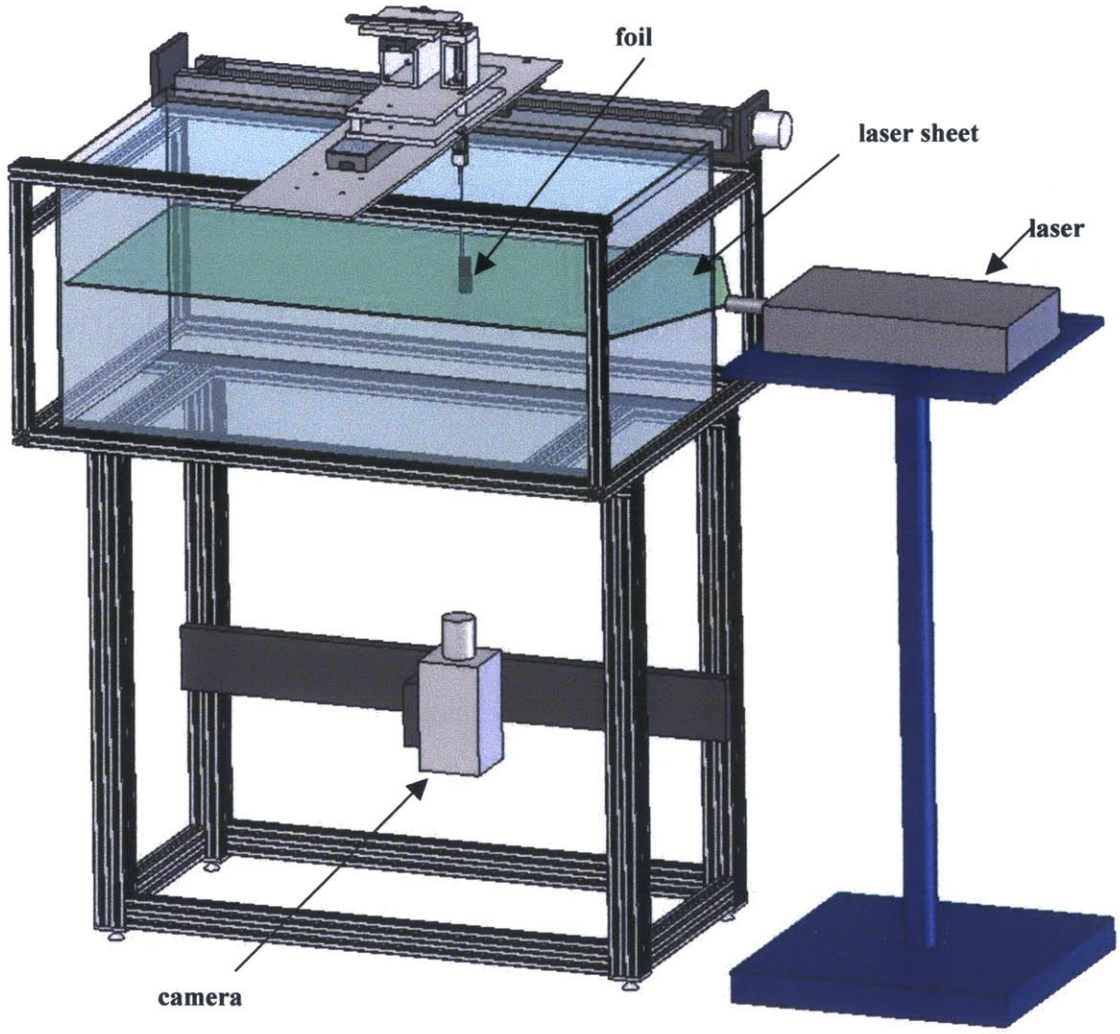

Figure 30: PIV set up. A laser emits a light sheet through the mid-span of the foil. A camera below the plane is equipped with a filter so it records only what illuminated in the laser's 2-D field.

used to illuminate the plane of interest and the water is seeded with particles. These particles are neutrally buoyant and small enough that they do not significantly impact the flow. A camera is placed perpendicular to the laser sheet. The lens has a filter, so the camera records only what the laser illuminates. The laser and camera configuration is shown in figure 30.

While the fluid is in motion, the laser pulses twice over a very short period of time δt. The camera is synched with the laser and takes images at these two points. Two of these images are shown in figure 31. The images are then broken up into small

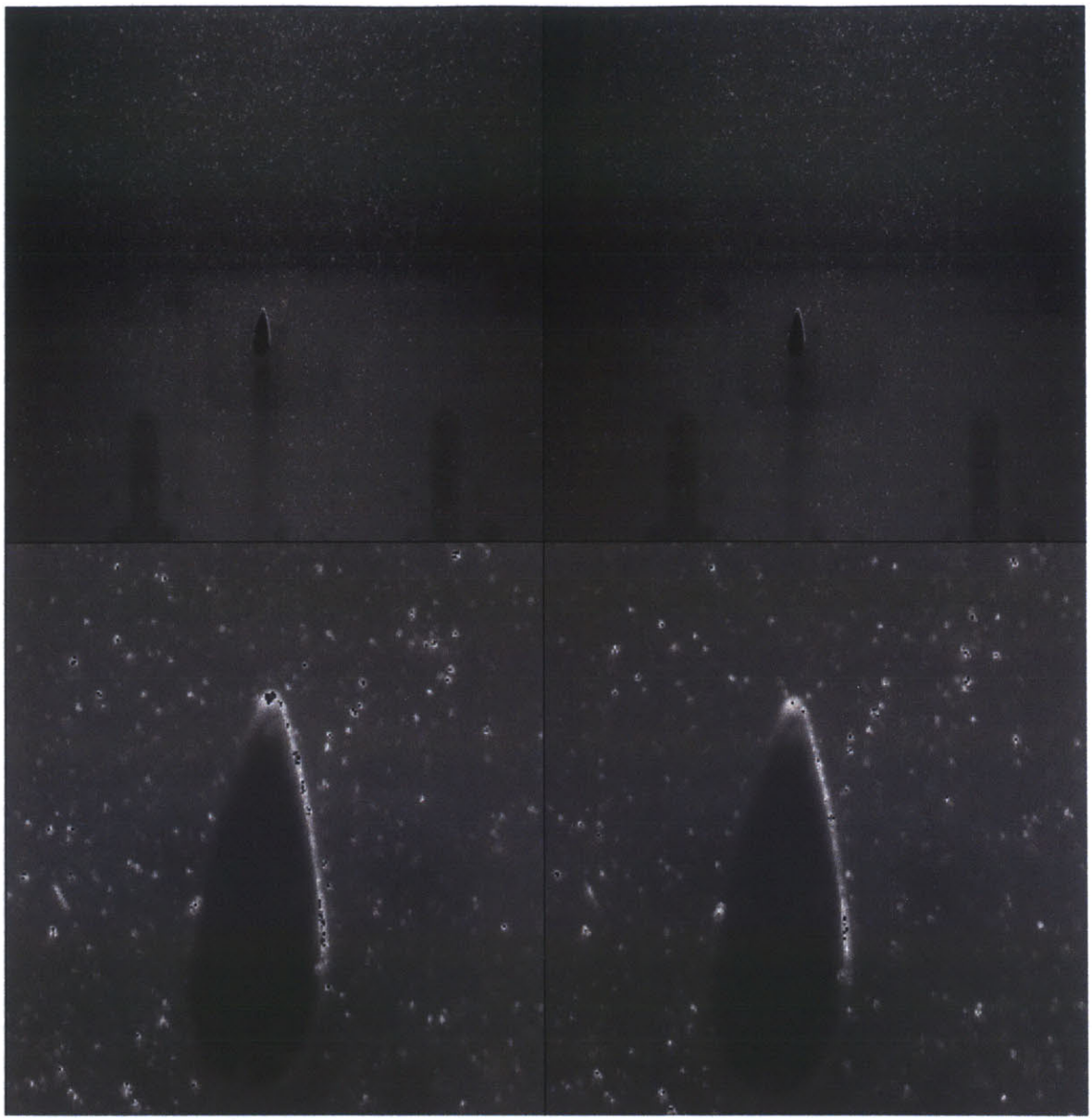

Figure 31: A close up look at PIV. The top images are two pictures taken 0.05 seconds apart. The bottom images are the same images as the top, zoomed in on the foil to see the individual particles.

squares. FFT is used to determine the relative motion of each square between the two frames, which gives the resulting velocity vectors. Davis, a software package by LaVision, was used to do these calculations. Davis simplifies the PIV process, allowing the user to specify the window size, the overlap between windows, and the time between frames. Gharib and Willart (1991) have studied the accuracy of Davis.

4.3 Thrust and Efficiency Calculations

The numerical output from PIV is horizontal and vertical velocity vectors. In order to calculate thrust, this data needs to be processed. Thrust can be calculated by applying conservation of momentum to a control volume surrounding the flapping foil. Conservation of momentum for an arbitrary control volume is defined as

$$F = \frac{D}{Dt}\int_V \rho\vec{u}dV = \int_V \frac{\partial}{\partial t}(\rho\vec{u})dV + \int_S \rho\vec{u}\vec{u}\cdot\hat{n}dS \qquad Eq.\ 7$$

where V is the volume of the control volume, ρ is the density of the fluid, u is the velocity of the fluid, S is the surface of the control volume and $\hat{n}$ is the unit normal vector to the surface [Kundu and Cohen, 2004]. F is the sum of all body forces on the fluid. Although the foil was actually being towed through still water, the analysis is simplified if the foil is considered stationary as water passes through the boundary. Since thrust is the desired result, conservation of momentum is applied in the x-direction. Conservation of momentum is evaluated over the area spanning from one chord length behind the foil to far away from the foil in all other directions; this control volume shown in figure 32. Steady flow and uniform hydrostatic pressure at the control surfaces are assumed. Since the normal components on the top and bottom surfaces of the control volume are in the y-direction, the momentum equation simplifies to

$$T = p\int_1^4 u(y)^2 - U^2 dy \qquad Eq.\ 8$$

Where U is the forward velocity on the leading edge side of the control volume and $u(y)$ is the forward velocity plus the perturbation velocities measured from PIV one chord

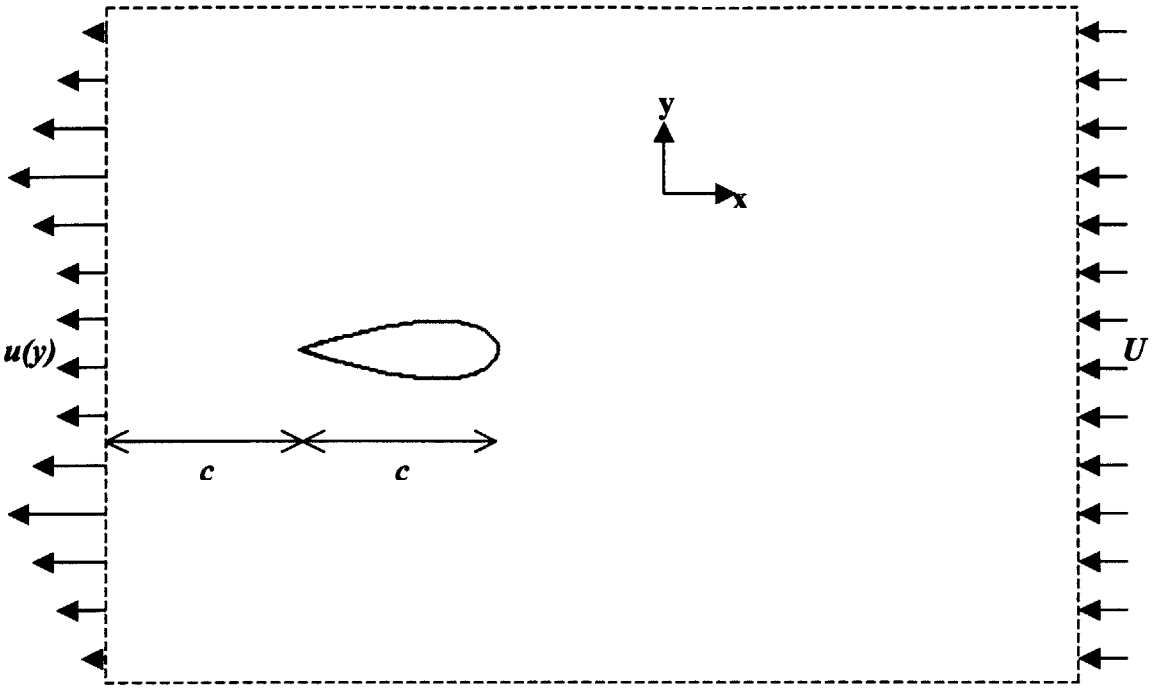

Figure 32: The control volume approach to conservation of momentum. At a distance far in front of the foil, the velocity is a uniform speed *U*. One chord length behing the foil, the velocity is *u(y)*, which is actually the perterbation velocity seen in the PIV added to the forward speed *U*.

length behind the foil. With conservation of mass, that expression simplifies to

$$T = p\int_{1}^{4} u(y)(u(y)-U)dy \qquad \textit{Eq. 9}$$

Though this result is accepted and used often, many of the assumptions are not valid [Anderson, 1996]. The constant pressure assumption is invalid because vortices cause changes in pressure and the wake of a flapping foil. Conservation of mass is not valid because the flow is largely three-dimensional as shown in the fluorescent dye visualizations. Perhaps the largest concern is that the flow is not steady, so disregarding the unsteady term in the momentum equation is not completely justified. In order to partially rectify the concern over the unsteadiness of the flow, instead of looking at

absolute thrust, a phase average thrust was used. Phase average thrust is defined as

$$\overline{T} = \frac{1}{N}\sum_{n=1}^{N} T\left(\tau = 2\pi\left(\frac{n}{N}\right)\right) \qquad \textit{Eq. 10}$$

where N is the number of images per cycle and $T(\tau)$ is thrust evaluated when the foil is at phase τ. The value N was limited by the maximum frequency of the camera. Two-dimensional phase average thrust coefficient is therefore defined as

$$Ct = \frac{\overline{T}}{\frac{1}{2}\rho U^2 (2h_o)} \qquad \textit{Eq. 11}$$

Hydrodynamic efficiency of a foil is defined as

$$\eta = \frac{P_o}{P_i} \qquad \textit{Eq. 12}$$

where P_o is power output and P_i is power input. Power output is simply defined as

$$P_o = \overline{T}U \qquad \textit{Eq. 13}$$

Power input is considerably more difficult to define. In words, the power input is the power required to heave and pitch the foil. Previous foil experiments have determined this by using force transducers [Anderson *et al.*, 1998] on the foil or determining it from the motor power. Unfortunately neither of these options was possible with the experimental setup used for the experiments. The foil was too small to use with force transducers and the motors used had no feedback. Some numerical experiments determine power in by integrating the pressure along the boundary of the foil [Blondeaux *et al.*, 2005]. Linear theory for two-dimensional flows provides thrust and efficiency

predictions. For sinusoidal heaving foils, the thrust, lift, and moment forces can be calculated using exact numerical solutions [Wu, 1971].

One proposed method of estimating efficiency was to use the theoretical power and the experimental thrust. However there were several problems with this approach. The first is that linear theory neglects viscous forces. This would suggest that efficiency calculated in this way would always be higher than the actual efficiency. However, several experiments, like those in Anderson *et al.* (1998), have shown efficiencies to be higher than those predicted by linear theory. This is because linear theory neglects higher order terms that increase efficiency. Since these higher order terms are non-linear, it is not obvious how any errors in efficiency would scale with Reynolds number or Strouhal number. This means that there is no guarantee that trends seen in efficiencies calculated using theoretical power and experimental thrust would be accurate. These factors lead to the conclusion that any attempt to estimate efficiency for the experiments performed in this thesis would be greatly flawed. For that reason, the efficiencies of the foils are not calculated.

4.4 Prior PIV experiments

There has been a lot of experimental work done involving PIV performed on flapping foils. Anderson (1996) and Anderson *et al.* (1998) performed PIV on high aspect ratio foils and obtained thrust and efficiency data as well as qualitative information about the wake. PIV is also very valuable for biological experiments. A flapping foil can be hooked up to a force transducer; a live fish, typically, cannot. Often PIV is used in live fish experiments to determine the fluid dynamics seen in a variety of fish maneuvers [Drucker and Lauder, 1999].

4.5 Experimental Setup

All of the experiments were run using the apparatus described in chapter two. Glass PIV particles 9-12 um in diameter were mixed into the tank. A New Wave Gemini Nd:YAG laser was positioned so that the light sheet it projected crossed the mid-plane of the foil. A Kodak Es. 4.0 camera was mounted beneath the tank. Both the laser and camera were connected to a computer where Davis software synched them and performed the PIV calculations. This set up is shown in figure 30.

The laser was placed on a leveling table. The camera was leveled using miniature visual levels. The camera was manually aligned with the axis of travel. Images of the foil were taken at either end of the camera's range of vision. If there was any deviation along the axis of travel, the camera was adjusted. This process was repeated until the error was less than the camera's resolution of one pixel. In order to calibrate the images, a ruler was placed on the level of the foil mid-plane in the tank and images of the ruler were taken. Using the Davis software, the ratio between pixels and mm was determined. One of these images is shown in figure 33.

The initial low Strouhal number experiments discussed in this chapter were performed on the same foils as those discussed in chapter 3. The motion of the foils was dictated by equations 1 and 2. Reynolds number, Strouhal number, phase shift between heave and pitch, and maximum pitch angle were all varied according to the values listed in table 2. In order to ensure proper phase averaging of the thrust, the frequency of the velocity fields calculated was proportional to the frequency of oscillation. For each of the runs discussed in this chapter, the velocity field would be measured eight times per period. Another timing issue was determining the length of time in-between the two laser pulses. If there was not enough time between the frames, than there would be no noticeable motion of the particles; too much time between the frames and the PIV interrogation window would have to be large, yielding inferior results. A general PIV rule of thumb is that the particles should move about one-third the final box size in-between frames [Willart and Gharib, 1991]. For each of the runs, test runs were performed to estimate about what the time delay should be. Table 4 lists each of the runs,

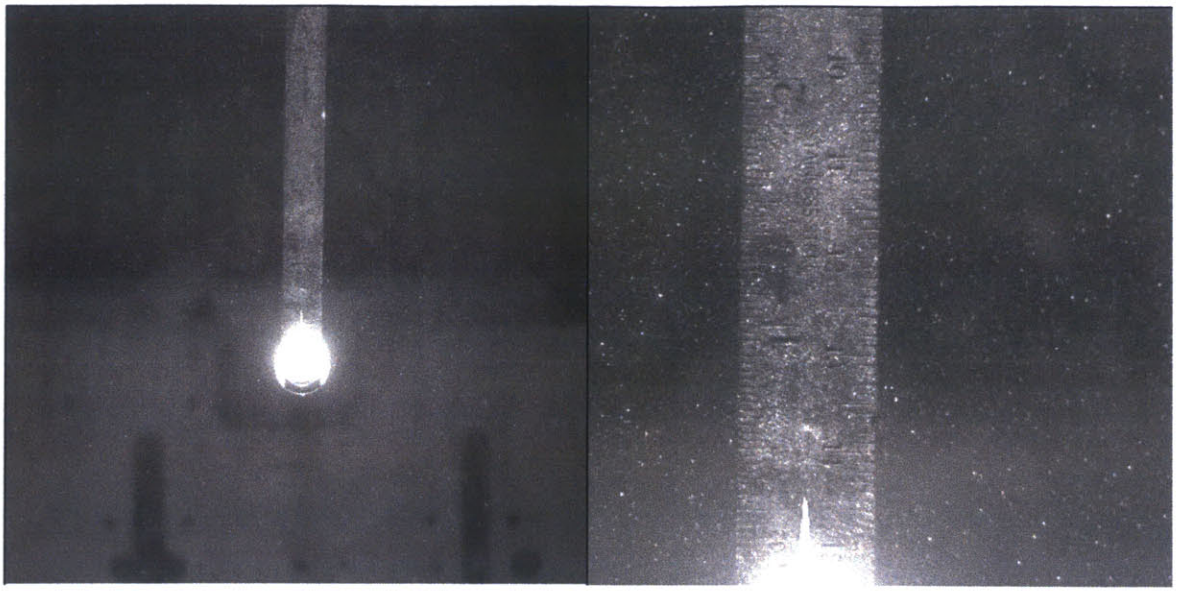

Figure 33: Calibration ruler. The image on the left shows the entire field while the image on the left shows a zoomed in image of the ruler.

St	θ_o	Φ	Frequency of oscilation, f	Frequency of camera, f_c	Time between frames, δt (μs)
0.2	*5°*	*90°*	*0.0895*	*0.7158*	*50,000*
0.25	*5°*	*90°*	*0.1118*	*0.8944*	*50,000*
0.3	*5°*	*90°*	*0.1342*	*1.0737*	*50,000*
0.35	*0°, 5°, 10°, 15°, 20°*	*90°*	*0.1566*	*0.7158*	*50,000*
0.35	*5°*	*60°, 75°, 90°, 105°, 120°*	*0.1566*	*1.2528*	*50,000*
0.4	*5°*	*90°*	*0.1789*	*1.4316*	*50,000*

Table 4: Data runs and respective camera frequencies. For each of these runs, the camera frequency was set so that the time inbetween data points was equal to one-eighth of a period.

frequencies of oscillation, frequencies of the camera, and time in between subsequent frames. Prior to each run, the tank was stirred and the glass cleaned with a squeegee. Then the water was allowed to settle. The laser and motors were triggered manually. Due to time constraints some, but not all, of the runs were repeated to determine repeatability.

4.6 Results and Analysis

PIV was performed on each of the cases outlined in table 2 using the PIV parameters listed in table 4. The velocity vectors and vorticity plots at $\tau=\pi/2$ are shown for each of these cases in figures 34 through 48. Figures 34 through 38 show increasing Strouhal number, figures 39 through 43 show increasing maximum pitch angle, and figures 44 through 48 show increasing phase shift between heave and pitch.

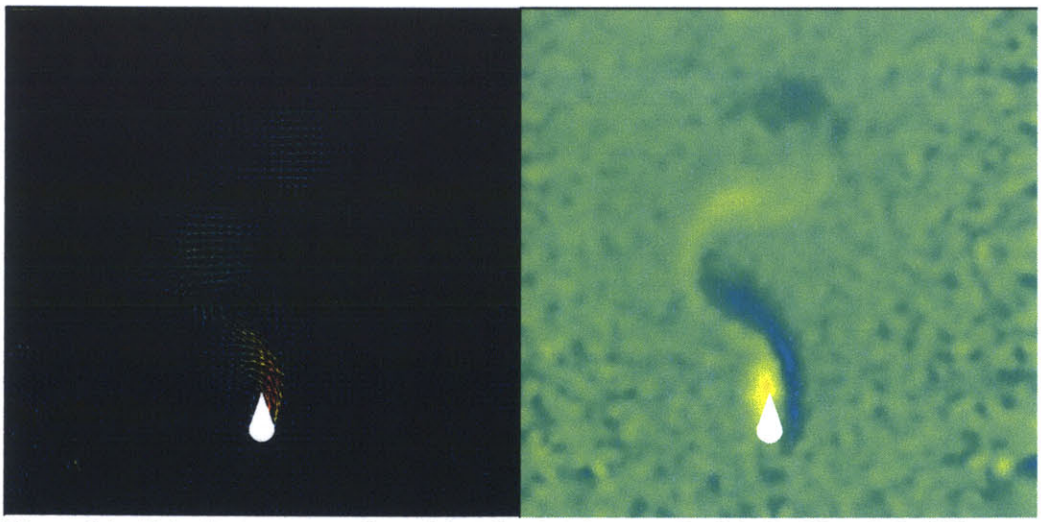

Figure 34: Velocity vectors and vorticity plot for the case $St=0.2$, $\theta_o=5°$, and $\Phi=90°$.

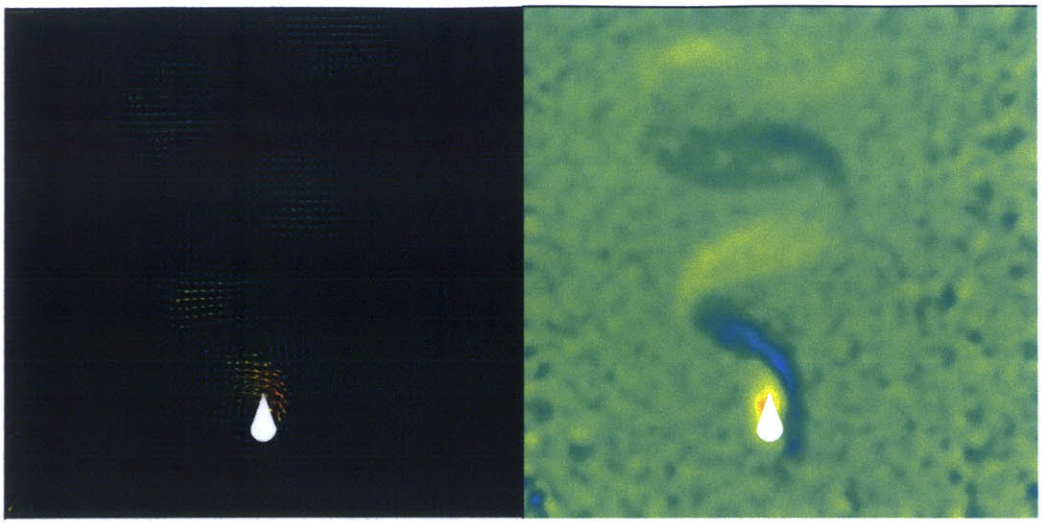

Figure 34: Velocity vectors and vorticity plot for the case $St=0.25$, $\theta_o=5°$, and $\Phi=90°$.

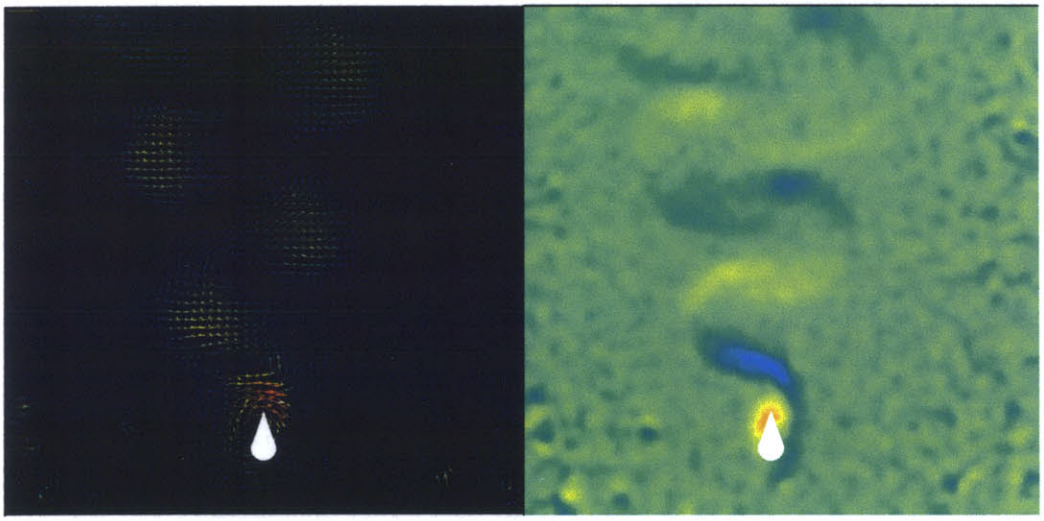

Figure 36: Velocity vectors and vorticity plot for the case $St=0.3$, $\theta_o=5°$, and $\Phi=90°$.

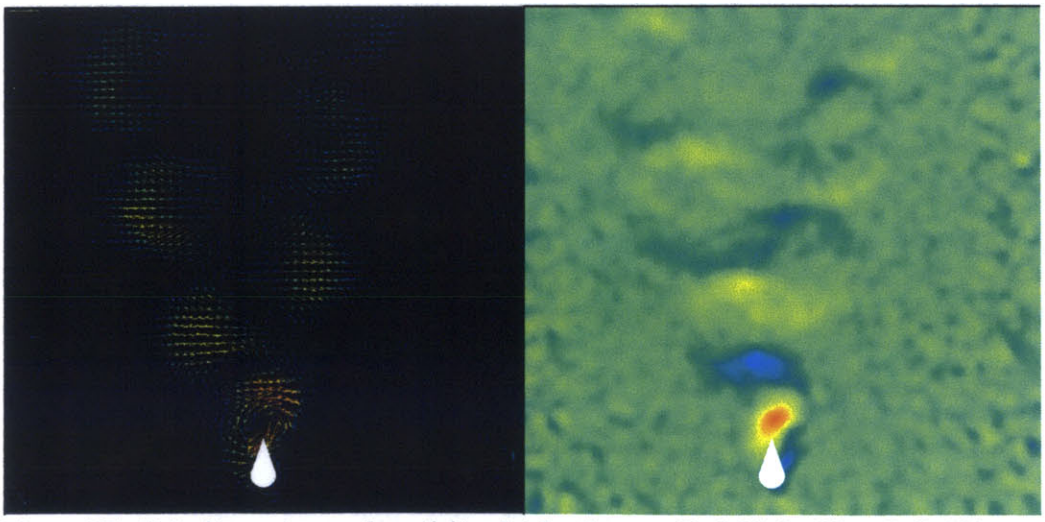

Figure 37: Velocity vectors and vorticity plot for the case $St=0.35$, $\theta_o=5°$, and $\Phi=90°$.

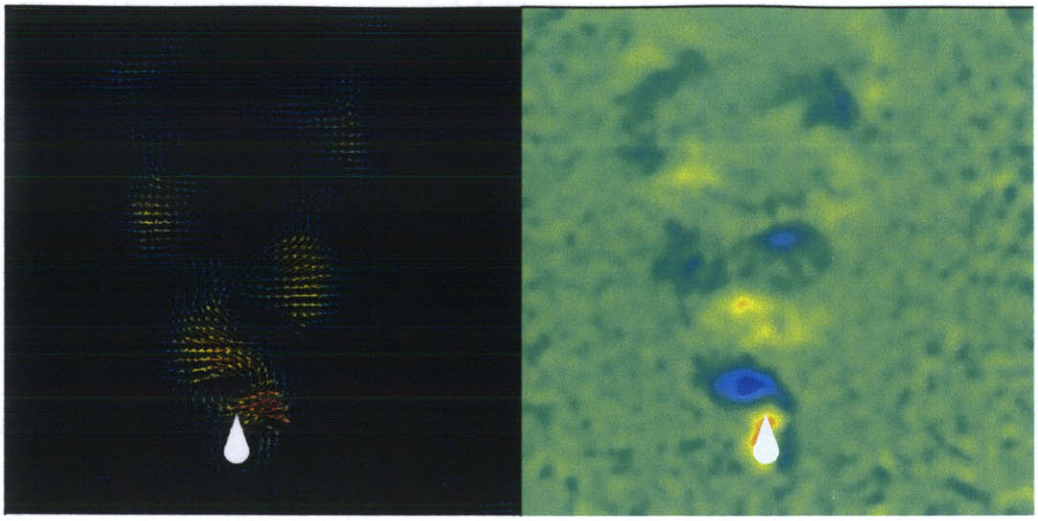

Figure 38: Velocity vectors and vorticity plot for the case *St=0.4*, θ_o=5°, and Φ=90°.

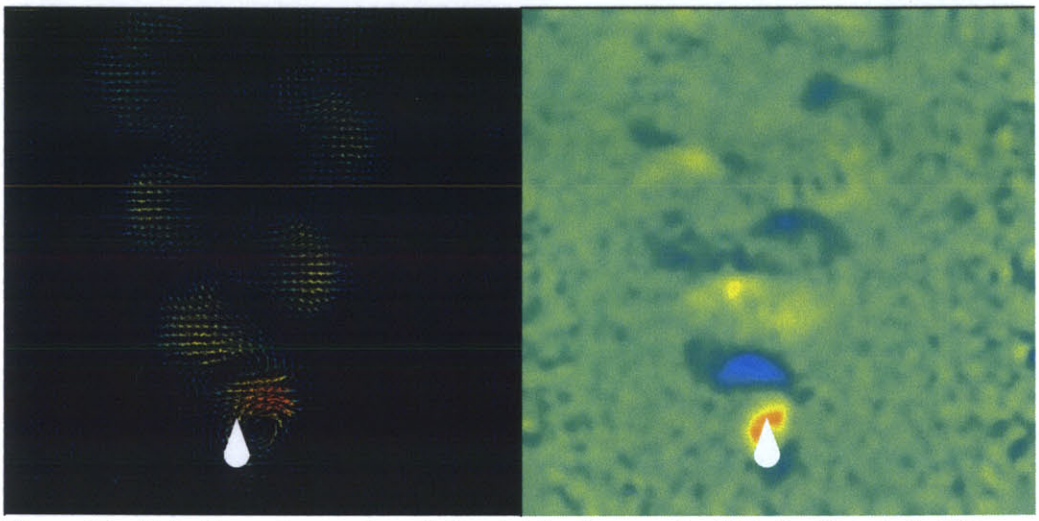

Figure 39: Velocity vectors and vorticity plot for the case *St=0.35*, θ_o=5°, and Φ=90°.

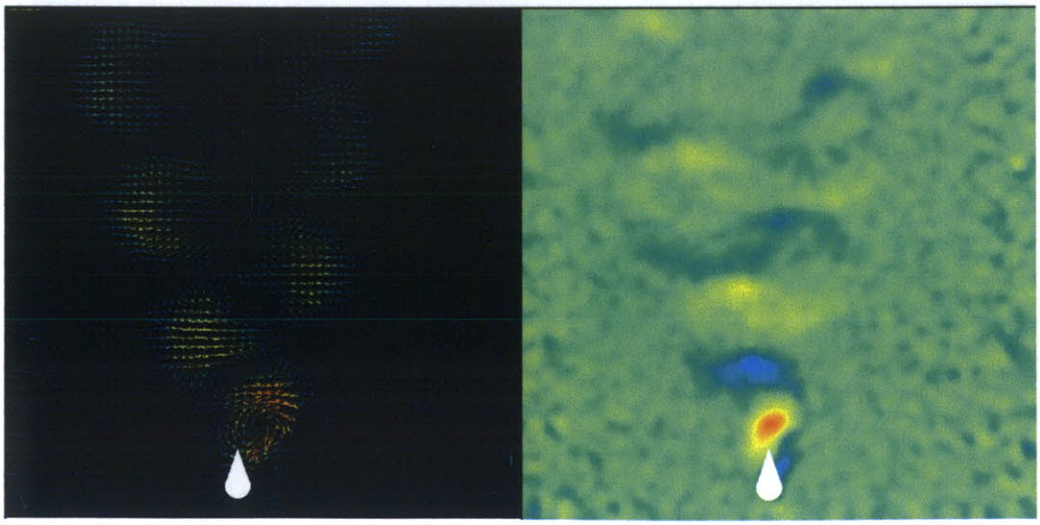

Figure 40: Velocity vectors and vorticity plot for the case *St=0.35*, θ_o=5°, and Φ=90°.

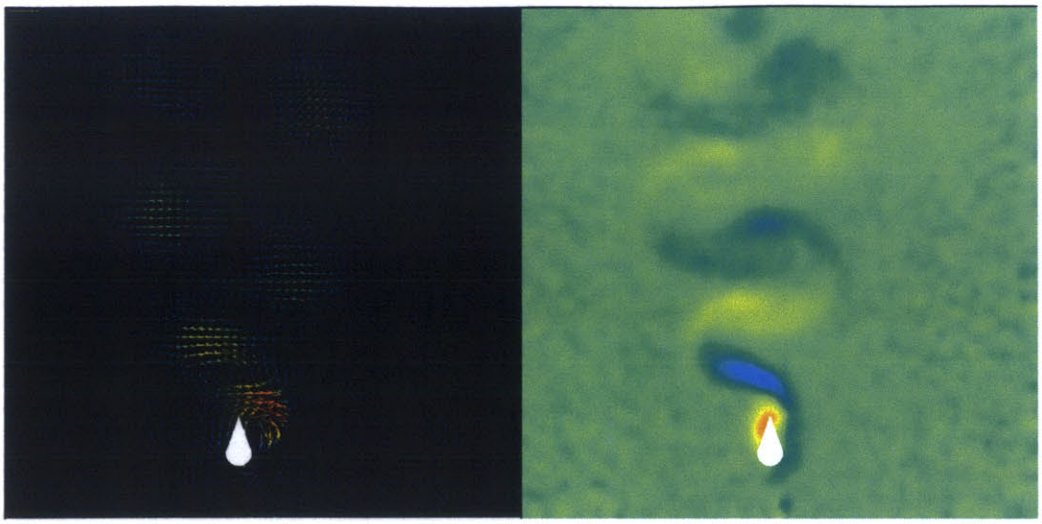

Figure 41: Velocity vectors and vorticity plot for the case *St=0.35*, θ_o*=10°*, and *Φ=90°*.

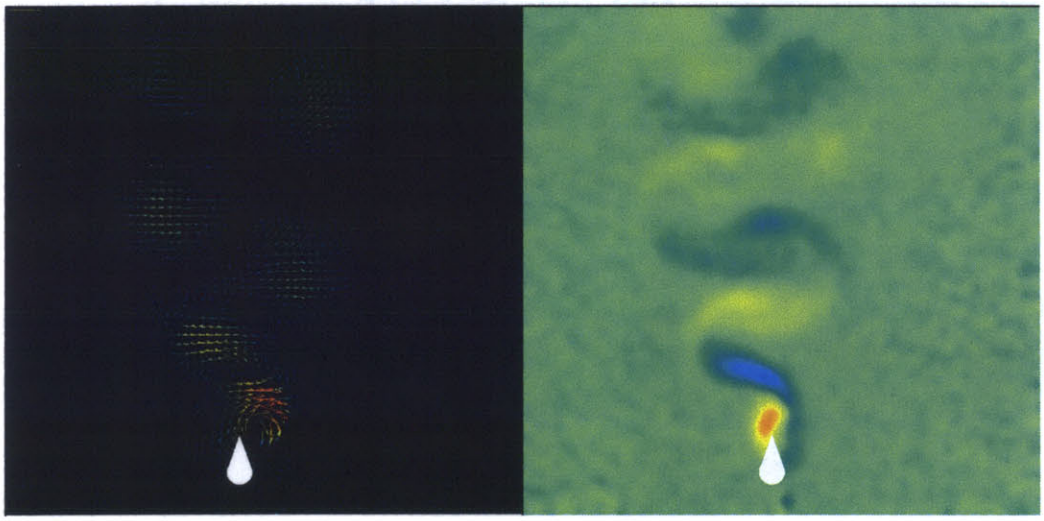

Figure 42: Velocity vectors and vorticity plot for the case *St=0.35*, θ_o*=15°*, and *Φ=90°*.

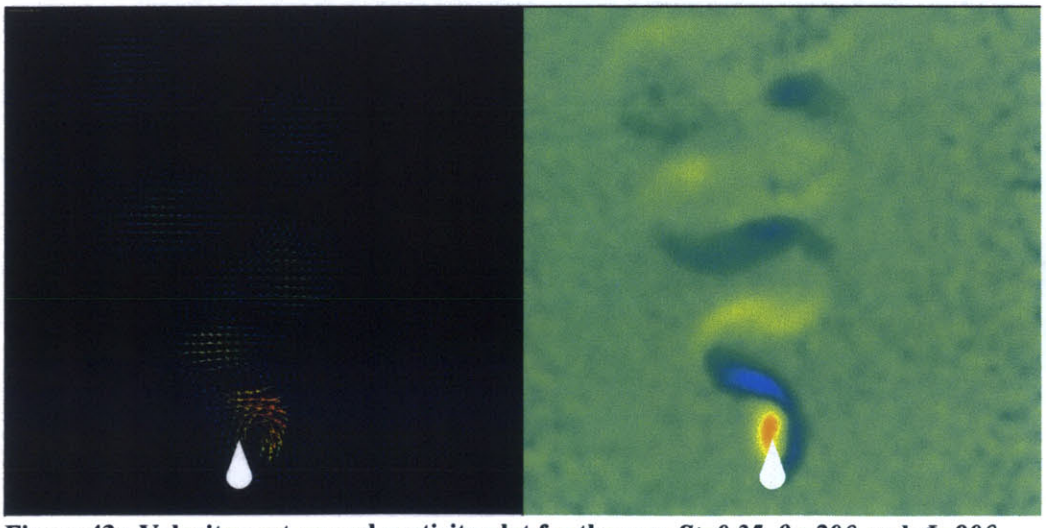

Figure 43: Velocity vectors and vorticity plot for the case *St=0.35*, θ_o*=20°*, and *Φ=90°*.

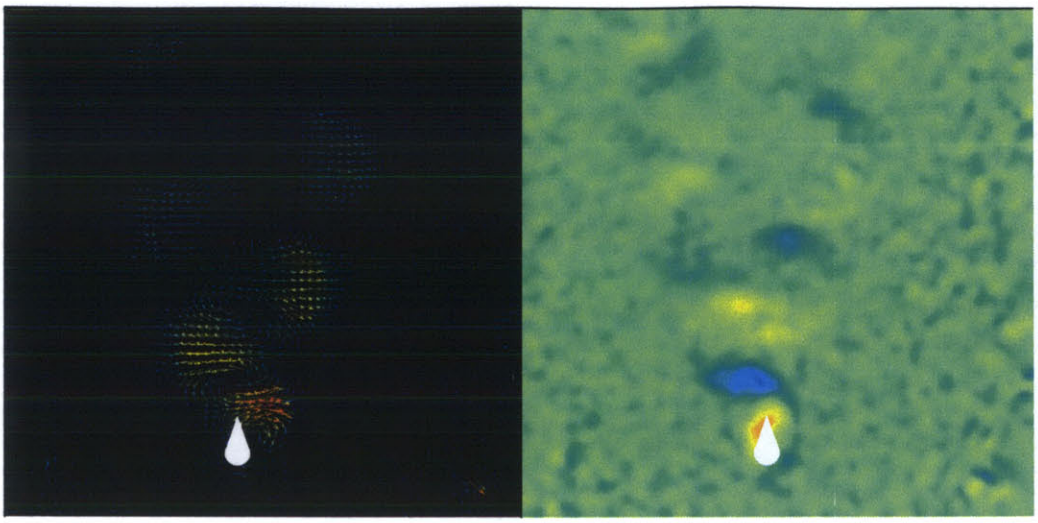

Figure 44: Velocity vectors and vorticity plot for the case $St=0.35$, $\theta_o=5°$, and $\Phi=60°$.

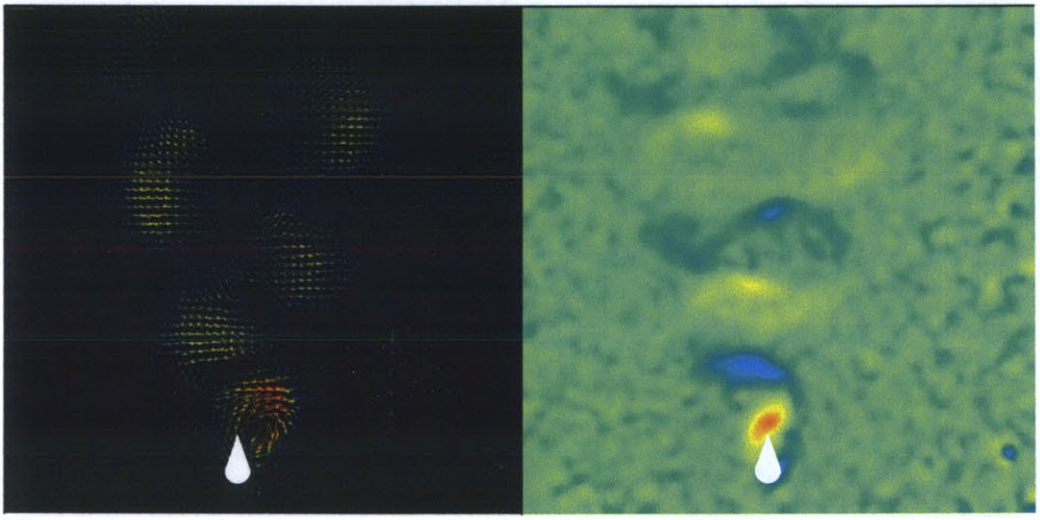

Figure 45: Velocity vectors and vorticity plot for the case $St=0.35$ $\theta_o=5°$, and $\Phi=75°$.

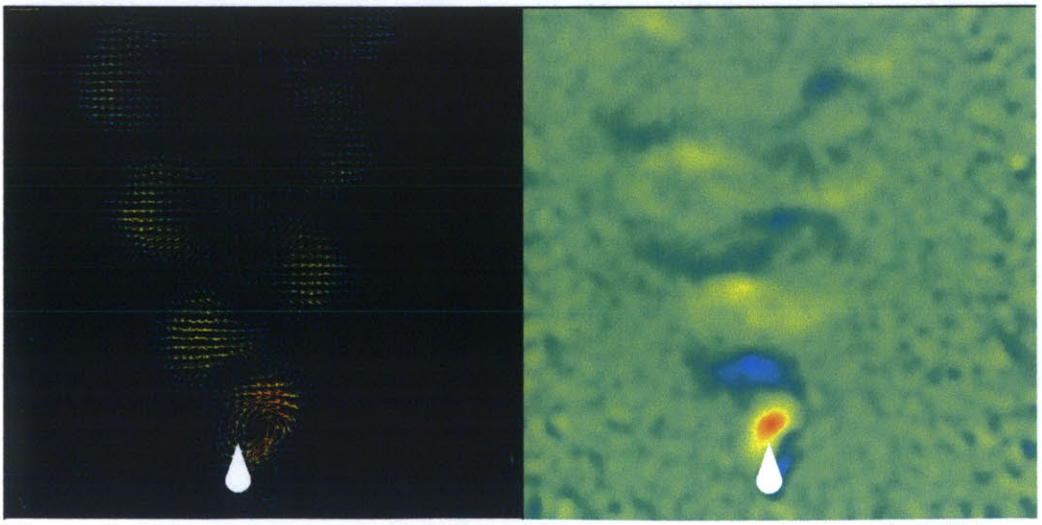

Figure 46: Velocity vectors and vorticity plot for the case $St=0.35$, $\theta_o=5°$, and $\Phi=90°$.

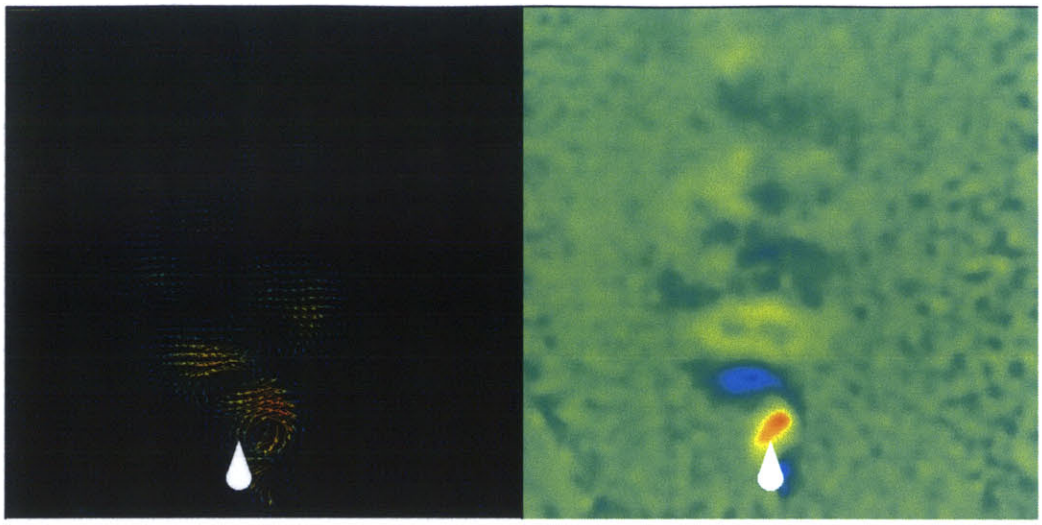

Figure 47: Velocity vectors and vorticity plot for the case *St=0.35*, θ_o*=5°*, and *Φ=105°*.

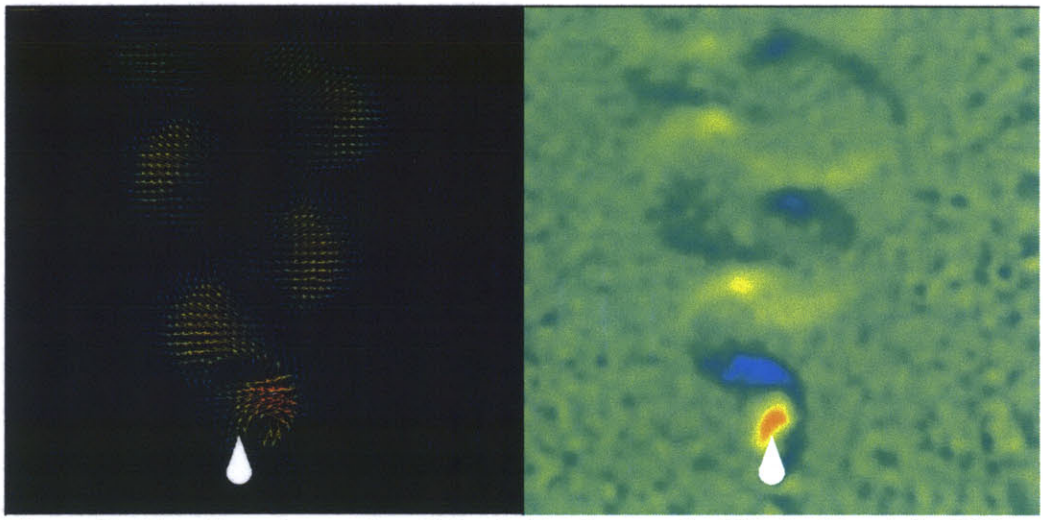

Figure 48: Velocity vectors and vorticity plot for the case *St=0.35*, θ_o*=5°*, and *Φ=120°*.

St	θ_o	Φ	C_t
0.2	5°	90°	0.0185
0.25	5°	90°	1.864
0.3	5°	90°	0.2615
0.35	0°	90°	0.7737
0.35	5°	90°	-0.3034
0.35	10°	90°	2.098
0.35	15°	90°	0.9407
0.35	20°	90°	0.5783
0.35	5°	60°	-0.4987
0.35	5°	75°	0.1725
0.35	5°	105°	-1.291
0.35	5°	120°	1.617
0.4	5°	90°	0.5270

Table 5: Thrust coefficients from each run.

The PIV data looks strikingly similar to the fluorescent dye data in a qualitative sense. The velocity vectors show an 'S' wake at the lowest Strouhal numbers. As Strouhal number increases, the wake is characterized by discreet vortical structures. The velocity vectors field look very similar to the wingtip view of the fluorescent dye visualizations.

The results seen for increasing maximum pitch angle are somewhat difficult to interpret. The vorticity images look very similar. However the velocity vectors show that the vortex closest to the foil is more defined at higher maximum pitch angles.

As with the results from increasing maximum pitch angle, it is difficult to interpret qualitative results from the images obtained from increasing the phase shift between heave and pitch. One observation is that for phase shifts less than $\Phi=90°$ the vortical structures on the left had side of the graph seem more oblique than those on the right hand side. The reverse is true for phase shifts greater than $\Phi=90°$.

The main objective in performing PIV is to get quantitative data, in this case thrust. The thrust coefficients for each of these cases were calculated using the control volume method. The results are shown in table 5.

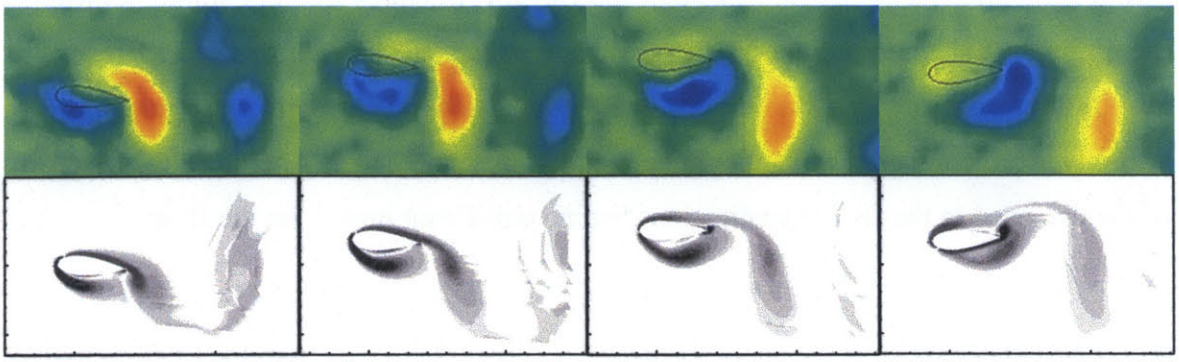

Figure 49: Top: Vorticity computed from PIV data for the case Re=161.5, St=0.35, θ_o=5°, and Φ=90° at times 0, πτ/4, πτ/2, and 3πτ/4. Bottom: Vorticity from Blondeaux *et al.* (2005) for the case Re=164, St=0.35, θ_o=5°, and Φ=90° at times τ=-π/2, -π/4, 0, and π/4.

Surprisingly there appear to be no trends within this data. Repeating the experiments found that the results fluctuated wildly and were not particularly repeatable. The reason for this comes from the scale of the actual thrust measurement, not the coefficient of thrust. The magnitude of the thrusts measured was on the order of 10-100 μN. Since the foil was moving so slowly, the coefficients of thrust computed were on the order of .1-1. Compared to the PIV grid used, these values of thrust are too small too be significant. They are all approximately zero. So despite the variation in parameters, there is no significant variation in thrust produced.

Since there is no thrust produced at the low Reynolds number, the topic of efficiency is moot. It should be noted that experiments were run with both the flexible and rigid foils. Just as in the dye visualization, both performed similarly. Other experiments have shown that while the coefficients of thrust are similar, the power required to oscillate the flexible foil is much less, therefore the flexible foils have much higher efficiencies [Prempraneerach *et al.*, 2003]. The dye visualizations compared very nicely do the flow patterns predicted by Blondeaux *et al.* (2005). One problem with those visualizations was that is was difficult to determine what affect the dye itself had on the flow. One of the advantages of PIV is that the measurement has no effect on the flow, therefore comparisons between PIV and Blondeaux *et al.* (2005) can be used to verify the dye visualizations. Since Blondeaux *et al.* (2005) computed vorticity, the vorticity observed in the PIV experiment was compared to that calculated by Blondeaux *et al.* (2005). The results are shown in figure 49.

The vorticities resulting from the PIV and those from Blondeaux *et al.* (2005) are virtually identical. The size and shape of the vortical structures are very similar as well as the timing and shedding of these structures. Not only does this confirm the PIV results, it also further confirms the fluorescent dye visualizations since both those and the PIV vorticity were compared to results generated by the same code. Therefore the viscosity of the dye used in the flow visualizations had no significant impact on the flow.

4.7 Discussion

Blondeaux *et al.* (2005) studied relatively low Reynolds and Strouhal numbers. This is because solving higher Reynolds and Strouhal number cases becomes computationally expensive. Also some assumptions break down at high Strouhal numbers or angle of attack. Separation and cavitation can occur at large angles of attack [Anderson, 1996]. Non-linear higher order terms can play a significant role at high Strouhal numbers [Wu, 1971]. Since a propulsion system is likely to operate at higher Reynolds and Strouhal numbers, it is advantageous to study how the thrust scales over a wide range of these parameters. This is especially true since the lower Reynolds and Strouhal number cases explored in this chapter failed to yield any thrust. The next chapter explores the morphology and thrust generated by foils at higher Reynolds and Strouhal numbers.

Chapter 5

Particle Image Velocimetry at Extended Reynolds and Strouhal Numbers

5.1 Overview

In this chapter, the thrust production of flapping foils, at relatively higher Reynolds and Strouhal numbers than those looked at in chapter 4, is studied. Since thrust is the aim of flapping foil propulsion, the main goal of these experiments is to figure out how to maximize it under certain conditions. Hydrodynamic efficiency is also of interest but because of apparatus limitations, it is not measured. This chapter looks at the results of other flapping foil experiments, the thrust and wake characteristics of the foils at these higher parameters calculated from PIV, the scaling of these characteristics, and finally how these results compare with what is seen in nature.

5.2 Prior Flapping Foil Experiments

Many flapping foil experiments have been performed at higher Strouhal and Reynolds numbers than those studied in chapter 4. Read *et al.* (2003) looked at Reynolds numbers $Re=5200$ and 12000 as well as higher maximum pitch angles and slight alterations in the heave profile to achieve a more favorable angle of attack. At maximum pitch angles of above $\theta_o=15°$ the foil achieved efficiencies of 50% and greater. In Anderson (1996) the cases studied had Reynolds number 1100 and Strouhal numbers up to 0.45.

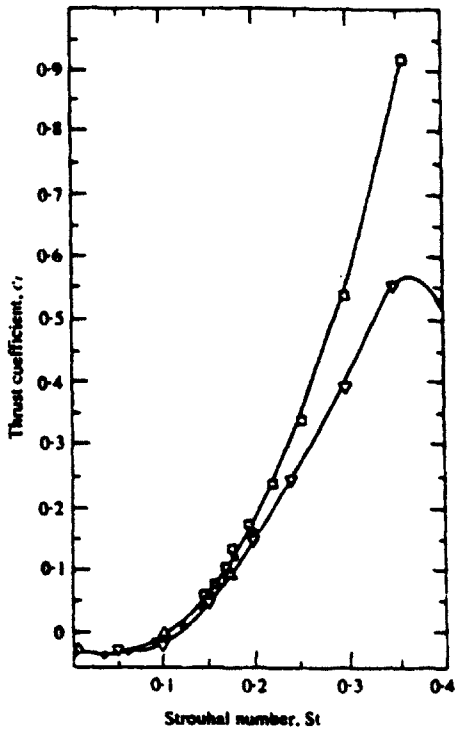

Figure 50: Peak seen in coefficient of thrust when Strouhal number is varied [Triantafyllou *et al.*, 1993].

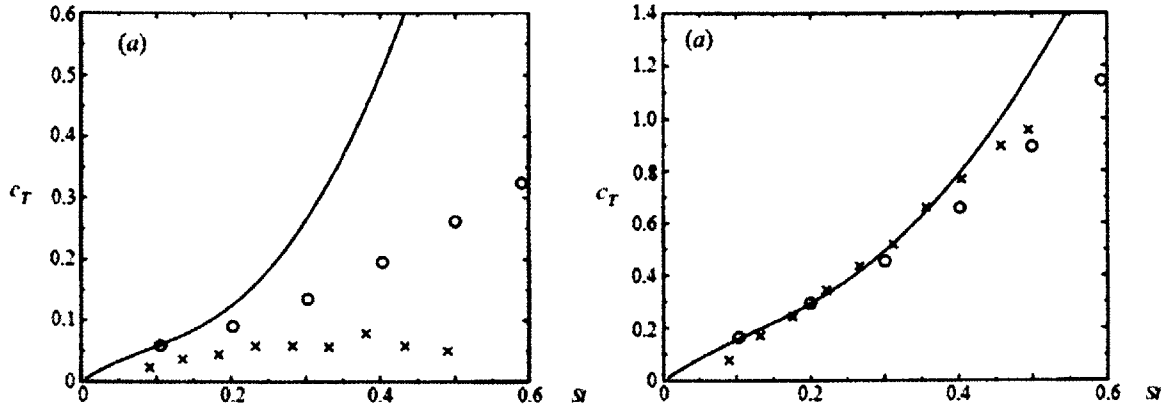

Figure 51: Two cases from Anderson *et al.* (1998). Experimental data is shown as 'x'. In the first case, there is a clear peak in coefficient of thrust. In the second case, coefficient of thrust is continuing to increase at the end of the Strouhal number range.

Triantafyllou *et al.* (1993) looked at Reynolds number *Re=17,000* and Strouhal numbers up to *St=0.35* and saw a peak in the coefficient of thrust at the higher range of the Strouhal variation, shown in figure 50. In Anderson *et al.* (1998), Strouhal numbers are varied from *St=0.1-0.5* at a Reynolds number of *Re=40,000*. In some of these cases the coefficient of thrust clearly peaks just as it does in Triantafyllou *et al.* (1993) where as in other cases the thrust coefficient is still increasing at the high end of the Strouhal number

Re	*St*
161.5	*0.2, 0.3, 0.4, 0.5, 0.6, 0.7, 0.8, 0.9, 1.0, 1.1, 1.2, 1.3, 1.4, 1.5*
750	*0.2, 0.3, 0.4, 0.5, 0.6, 0.7, 0.8, 0.9, 1.0, 1.1*
1000	*0.2, 0.3, 0.4, 0.5, 0.6, 0.7, 0.8*

Table 6: Parameter values for Reynolds number and Strouhal number.

range. An example of each of these cases is shown in figure 51.

5.3 Experimental Parameters and Setup

For Reynolds number *Re=1100*, coefficient of thrust increased with Strouhal number for the entire range of Strouhal numbers varied, but peaked when experiments were performed at a higher Reynolds number [Anderson, 1996]. Since the peak seen Triantafyllou *et al.* (1993) was at the high end of the Anderson (1996) Strouhal number range for *Re=1100*, it made sense to perform experiments similar to Anderson (1996) but at higher Strouhal numbers in an attempt to identify a Strouhal number of maximum thrust. This number would be very valuable in watercraft design since thrust is the primary parameter of interest. How this peak thrust Strouhal number scales with Reynolds number is also of interest since many AUVs operate over a wide range of Reynolds numbers. These reasons as well as the limitations of the apparatus determined the values of Reynolds number and Strouhal number to be varied, which are listed in table 6. For each of those cases the maximum pitch angle was set at $\theta_o=5°$ and the phase shift was set at $\Phi=90°$.

The experimental set up was the same as in chapter 4 as shown in figure 30 except the stepper motor was replaced with a DC motor to achieve higher forward speeds.

5.4 Results

This section discusses the quantitative and qualitative results of the PIV for each of the three Reynolds numbers studied. Velocity vectors and vorticity plots are shown

for a variety of Strouhal numbers, coefficients of thrust are calculated, and velocity profiles of the wakes are plotted.

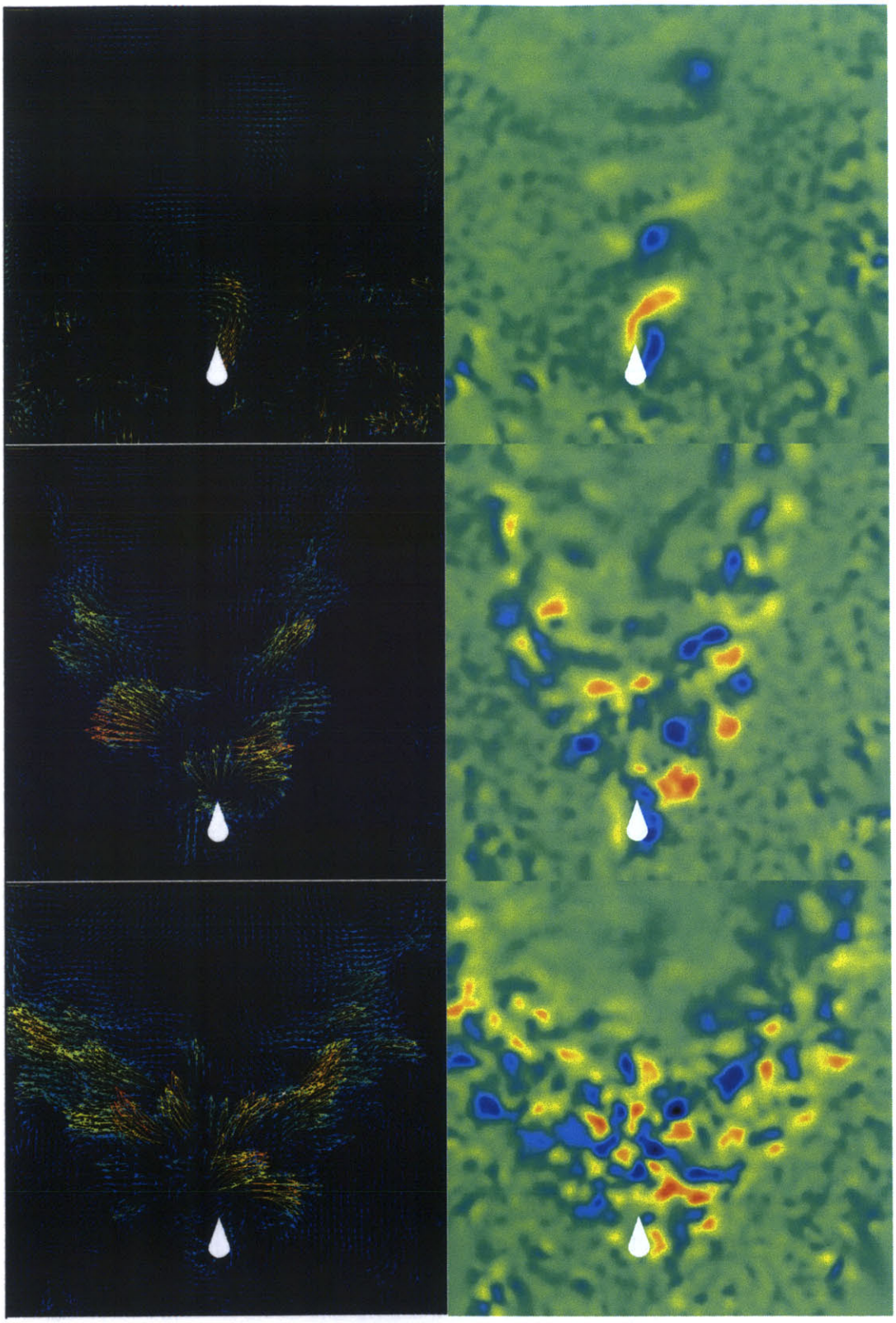

Figure 52: Velocity vectors and vorticity plots from PIV performed at Reynolds number *Re=161.5*. The top is *St=0.2*, the middle is *St=0.8*, and the bottom is *St=1.5*. They are representative of the three wake structures seen at this Reynolds number: the 'S' wake (top), the double jet wake (middle), and the breaking down wake (bottom).

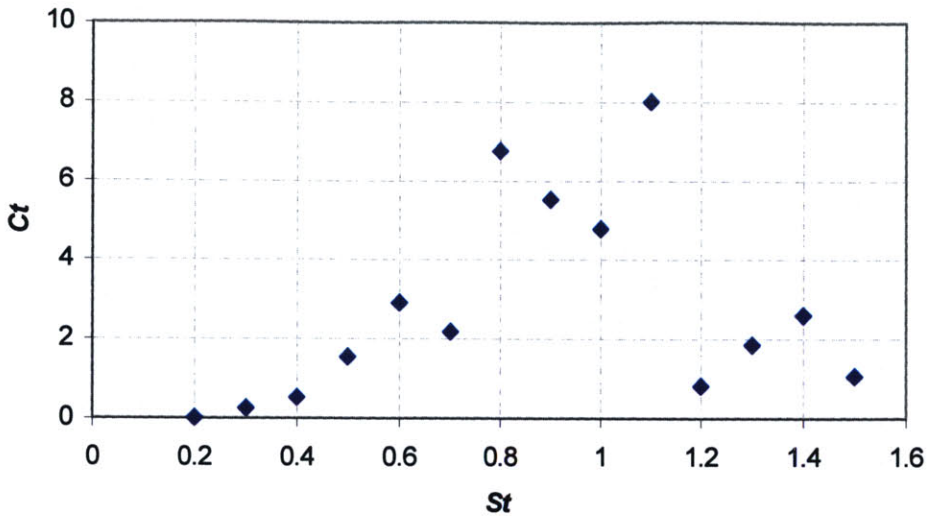

Figure 53: Coeffcient of thrust as a function of Strouhal number for *Re=161.5*.

For Reynolds number *Re=161.5*, the morphology of the wake of the flapping foil goes through three distinct phases. The first, illustrated by the top image in figure 51, is an 'S' wake like the one seen in the fluorescent dye visualizations and PIV for low Strouhal numbers. This wake is prevalent from Strouhal numbers *St=0.2-0.4*. The second phase is a double jet wake which occurs from Strouhal number *St=0.5-1.1*. During the third phase, the double jet wake breaks up due to the large density of vortical structures and their influence on one another. The coefficient of thrust also has three distinct phases, as shown in figure 53.

The reason these coefficients of thrust are so high is because the foil's side-to-side velocity is much higher than its forward velocity. This is similar to a tugboat getting started when it creates thrust but no forward motion. In that case the coefficient of thrust would be infinite. The region between Strouhal numbers *St=0.2-0.4* produces an 'S' wake and has a very low coefficient of thrust. The region where the double jet wake is seen, Strouhal numbers *St=0.5-1.1*, sees an increasing coefficient of thrust which peaks at *St=1.1*. Finally the region of highest Strouhal numbers, where the wake begins to break up, has much lower thrust coefficients than those seen in the double jet region. Velocity profiles for each of these wakes are shown in figures 54 through 56. These velocity profiles are the phase average velocities cut from one chord length behind the foil.

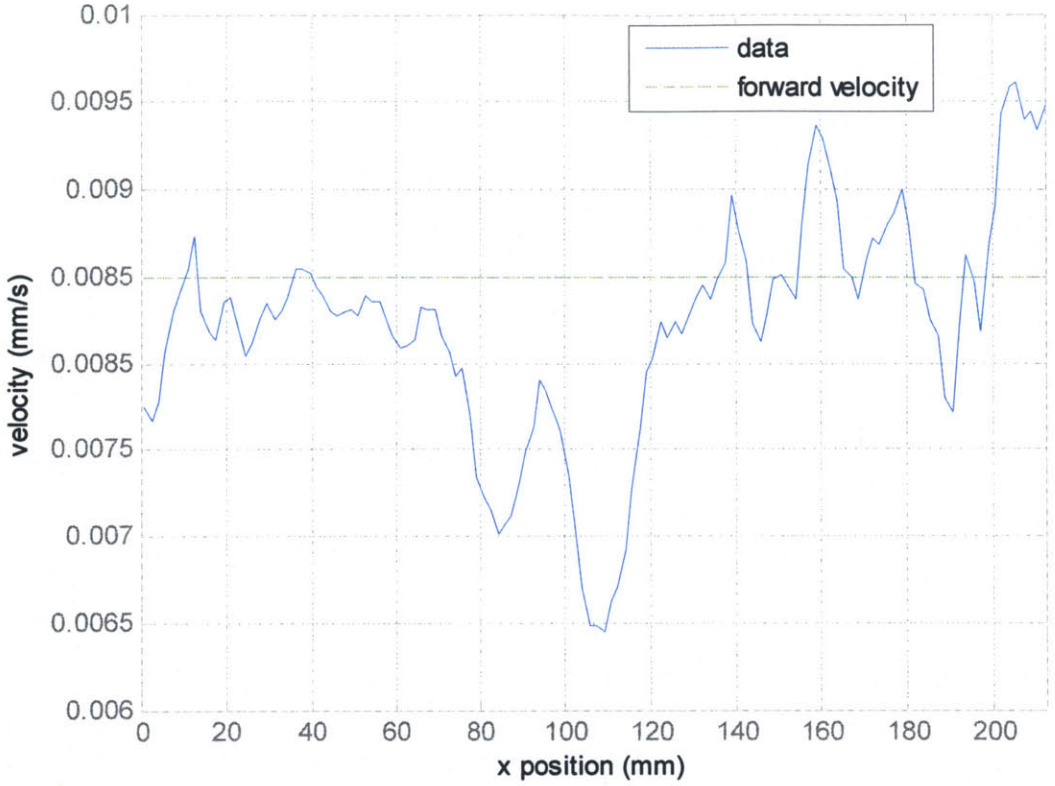

Figure 54: Phase averaged wake velocity profile for *Re=161.5, St=0.2.*

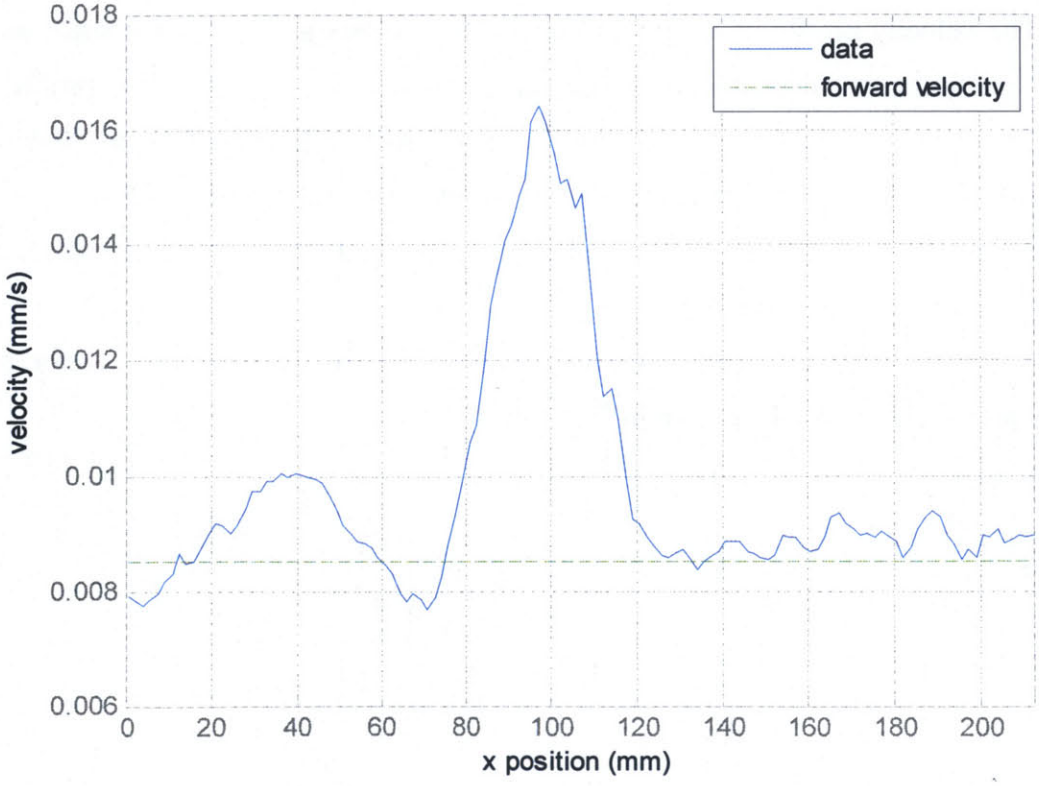

Figure 55: Phase averaged wake velocity profile for *Re=161.5, St=0.8.*

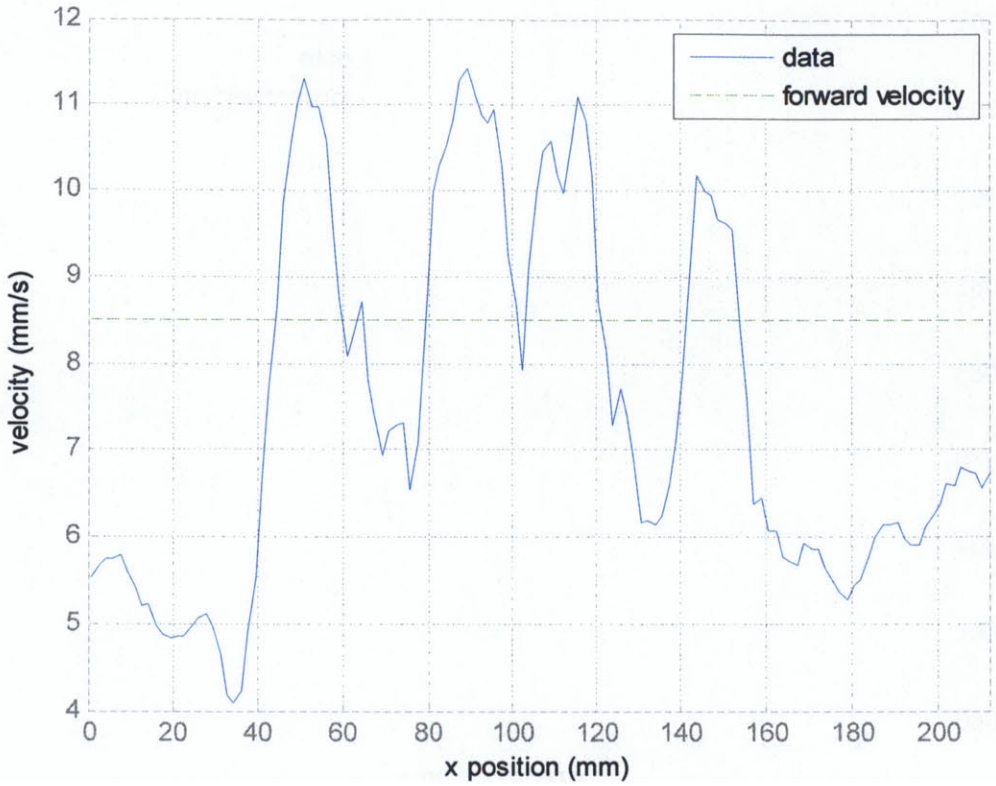

Figure 56: Phase averaged wake velocity profile for Re=*161.5*, *St=1.5*.

The velocity profile of *Re=161.5, St=0.2* clearly shows a drag wake since most parts of the velocity cross-section are less than the forward velocity. The profile at *St=0.8* illustrates a thrust wake with two peaks. Although one of these peaks is significantly higher than the other, this still constitutes a double jet wake. The velocity profile at *St=1.5* shows random and equally strong areas of thrust and drag suggesting there is no coherent wake structure.

The next Reynolds number studied is *Re=750*. Selected velocity vector and vorticity plots of the wake are shown in figure 57.

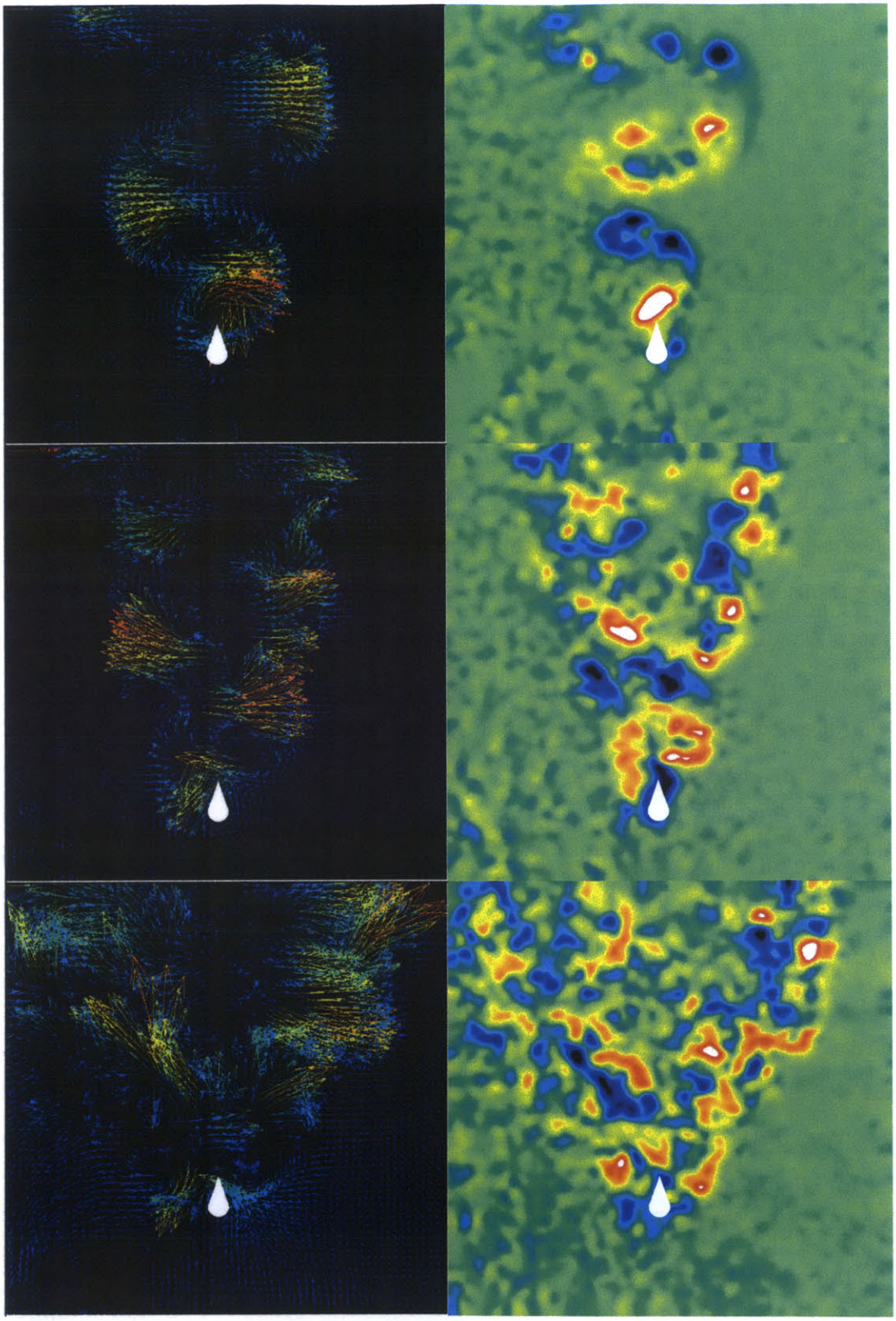

Figure 57: Velocity vectors and vorticity plots from PIV performed at Reynolds number *Re=750*. The top is *St=0.2*, the middle is *St=0.4*, and the bottom is *St=1.1*. They are representative of the three wake structures seen at this Reynolds number: the 'S' wake (top), the double jet wake (middle), and the breaking down wake (bottom).

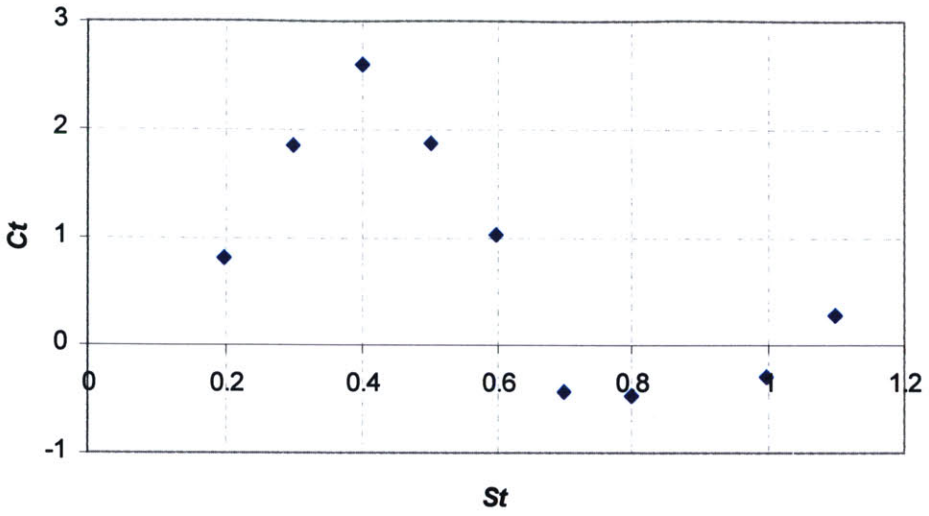

Figure 58: Coefficient of thrust as a function of Strouhal number for Re=750.

Just as with the *Re=161.5* case, the *Re=750* case sees three distinct wake morphologies as Strouhal number is increased. However, the Strouhal numbers at which these morphologies shift is different than the Strouhal numbers at which the morphologies shift for the *Re=161.5* case. The 'S' wake is seen from Strouhal numbers *St=0.2-0.3*, the double jet wake is seen from Strouhal numbers *St=0.4-0.5*, and the wake begins to break up at *St=0.6*.

The coefficients of thrust corresponding to each Strouhal number tested are shown in figure 58. Theses correlate to the morphology of the wake, just as they did for the *Re=161.5*. No thrust or little thrust is produced in the region of Strouhal numbers *St=0.2-0.3* where there is an 'S' wake. Higher thrust coefficients are seen between Strouhal number St=0.4-0.5 where there is a double jet wake. After the wake begins to break down, around Strouhal number 0.6, no or low levels of thrust are produced. Although these coefficients of thrust are significantly lower than those seen in the *Re=161.5* case, the magnitude of thrust is much higher, with a maximum thrust of about 1500 μN for *Re=750* as opposed to a maximum thrust of about 300 μN for *Re=161.5*. The velocity profiles verify the qualifications of the morphologies and are shown in figures 59 through 61.

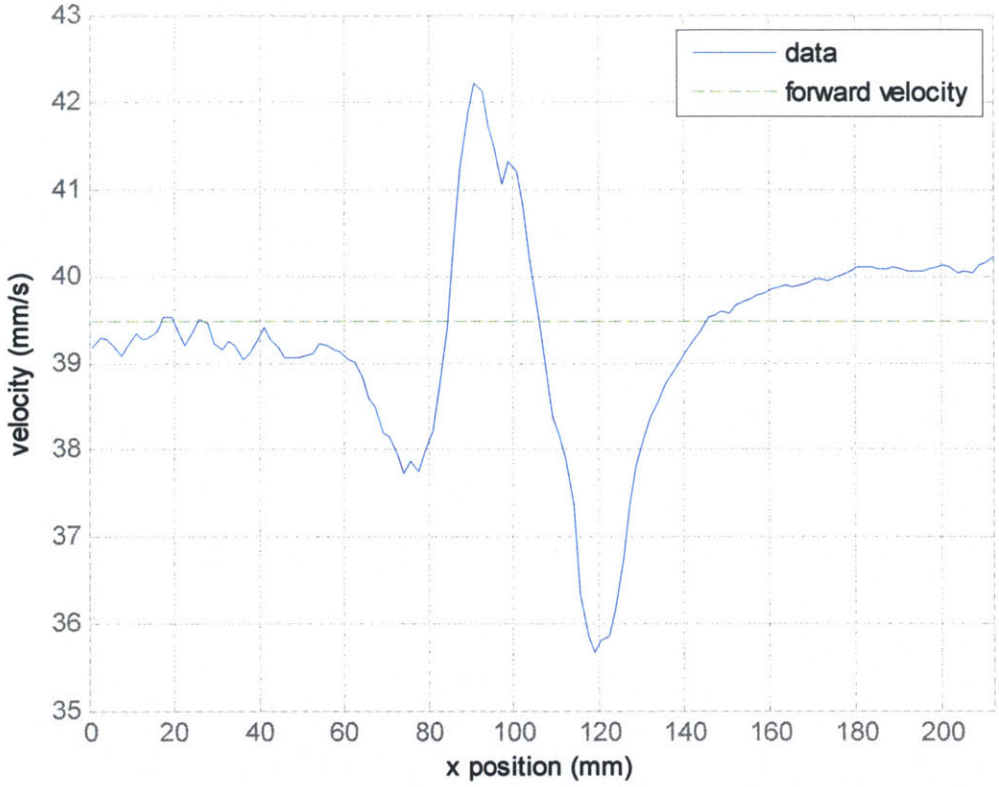

Figure 59: Phase averaged wake velocity profile for *Re=750, St=0.2.*

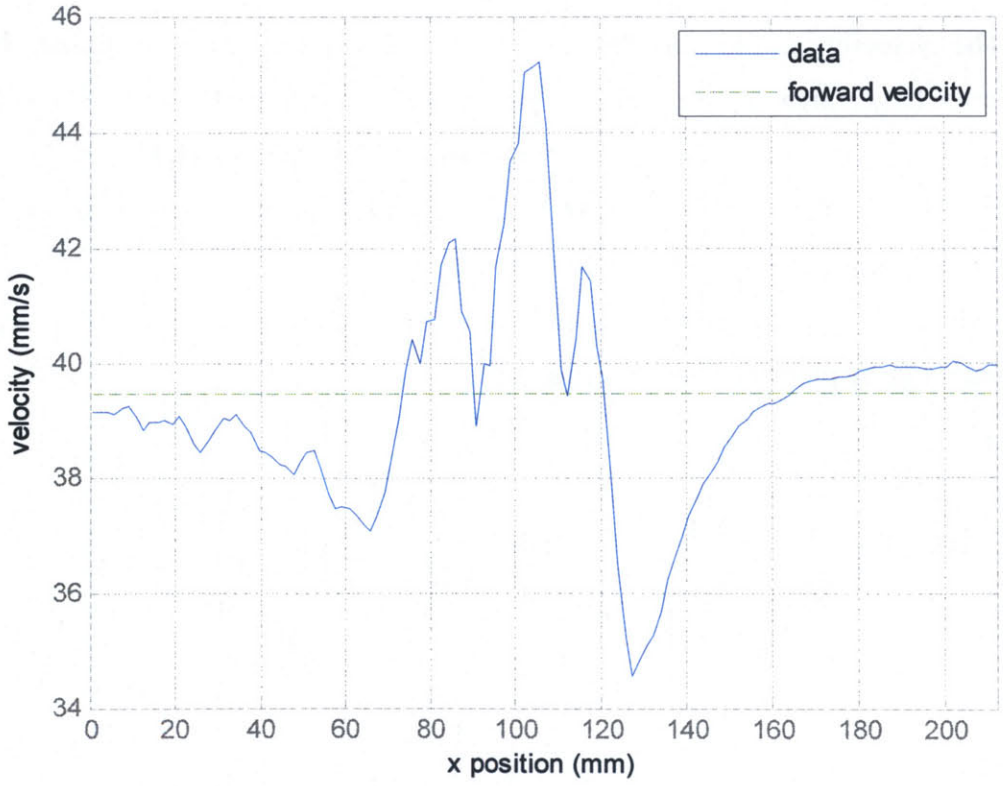

Figure 60: Phase averaged wake velocity profile for *Re=750, St=0.4.*

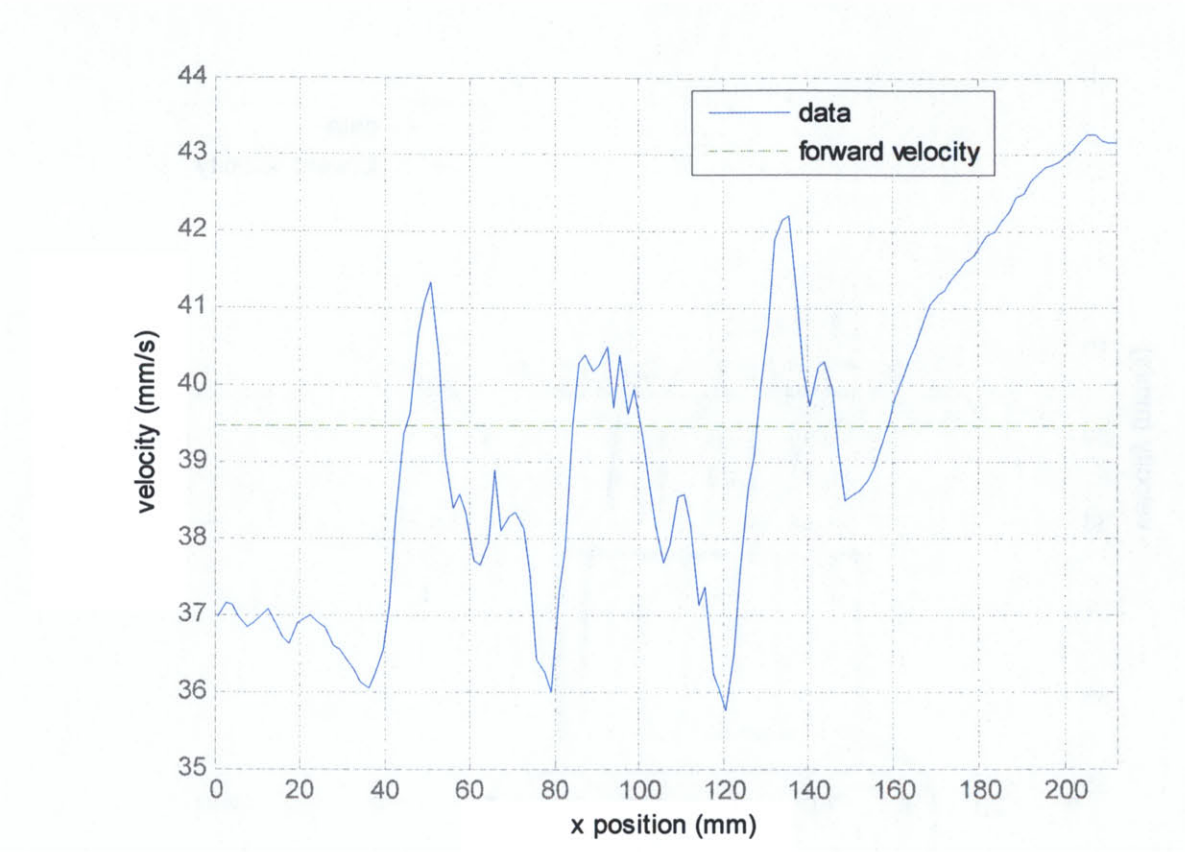

Figure 61: Phase averaged wake velocity profile for *Re=750, St=1.1.*

The velocity profile for *Re=750, St=0.2* shows one area of thrust, but a significantly larger area of drag. The velocity profile for St=0.4 shows two velocity peaks, confirming that it is indeed a double jet wake. The velocity profile for St=1.1 is similar to the velocity profile at *Re=161.5, St=1.5* because there are strong drag and thrust portions but no real coherent wake structure.

The last Reynolds number considered was *Re=1000*. Representative velocity vector and vorticity plots are shown in figure 62.

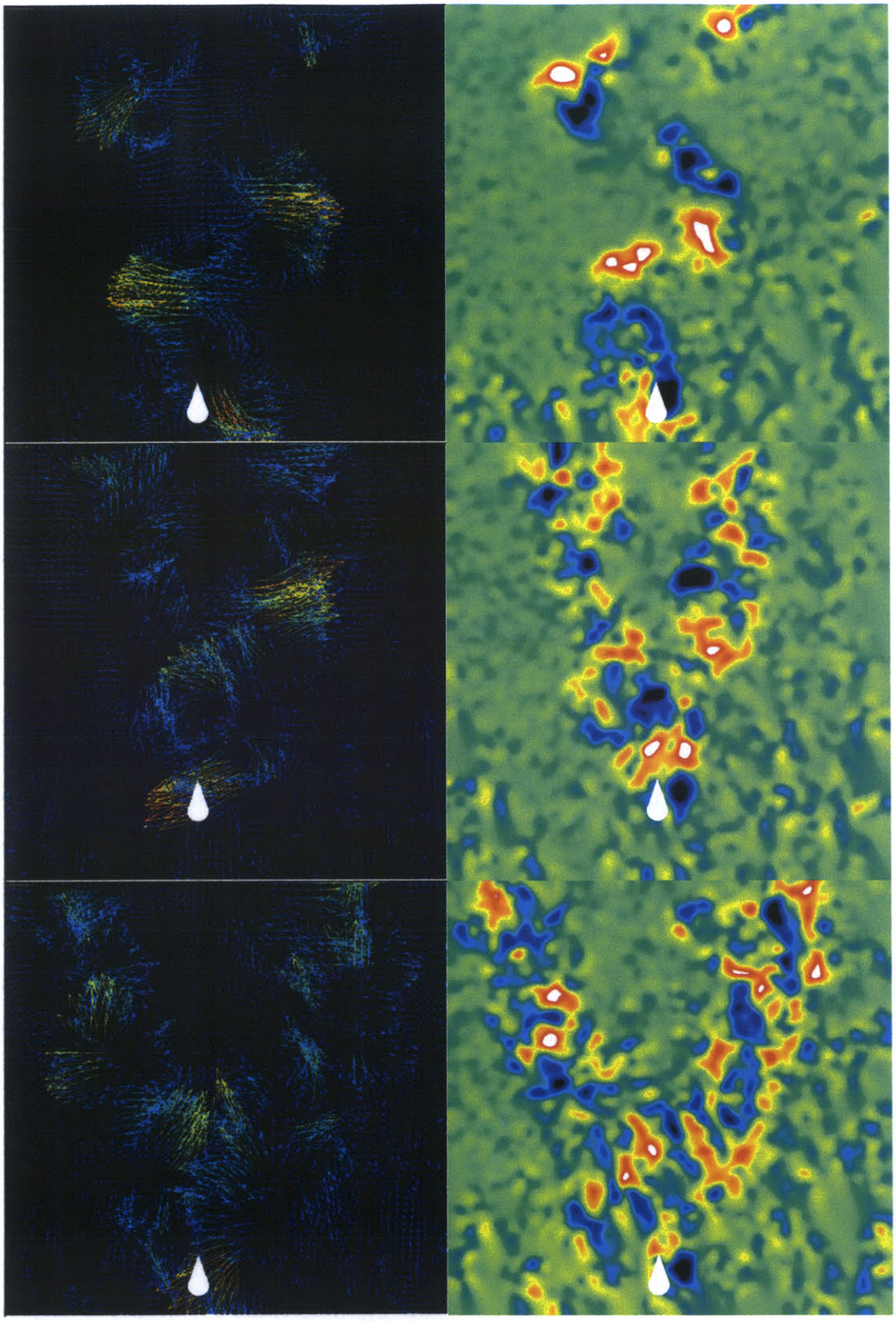

Figure 62: Velocity vectors and vorticity plots from PIV performed at Reynolds number *Re=1000*. The top is *St=0.2*, the middle is *St=0.4*, and the bottom is *St=0.8*. They are representative of the three wake structures seen at this Reynolds number: the 'S' wake (top), the double jet wake (middle), and the breaking down wake (bottom).

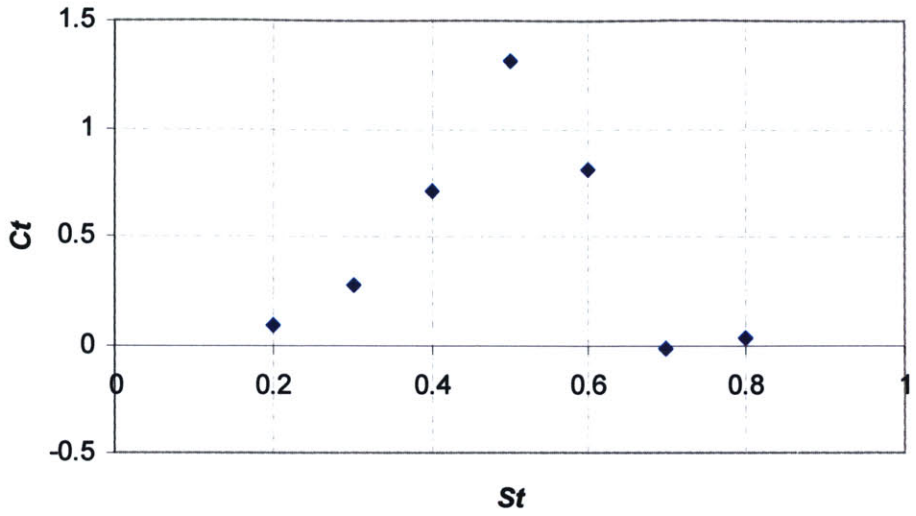

Figure 63: Coefficient of thrust as a function of Strouhal number for *Re=1000*.

The morphology of the wake for *Re=1000* goes through the same three phases seen in the other cases. The 'S' wake is seen from Strouhal numbers *St=0.2-0.3*, the double jet wake is seen from Strouhal numbers *St=0.4-0.5* and the wake begins to break up at Strouhal numbers greater than *St=0.6*. The corresponding thrust coefficients are shown in figure 63.

The coefficients of thrust once again correspond with the phases of the wake morphology. Low Strouhal numbers result in no or low thrust and an 'S' wake, moderate Strouhal numbers result in thrust and a double jet wake, and high Strouhal numbers result in low or no thrust and a poorly defined wake. Although the coefficients of thrust are lower for *Re=1000* than the other cases, the magnitude of thrust is higher. The maximum thrust achieved at *Re=1000* was about 2000 μN as opposed to 1500 μN for *Re=750* and 300 μN for *Re=161.5*. As with the other two cases, the morphologies are confirmed by velocity profiles in figures 64 through 66.

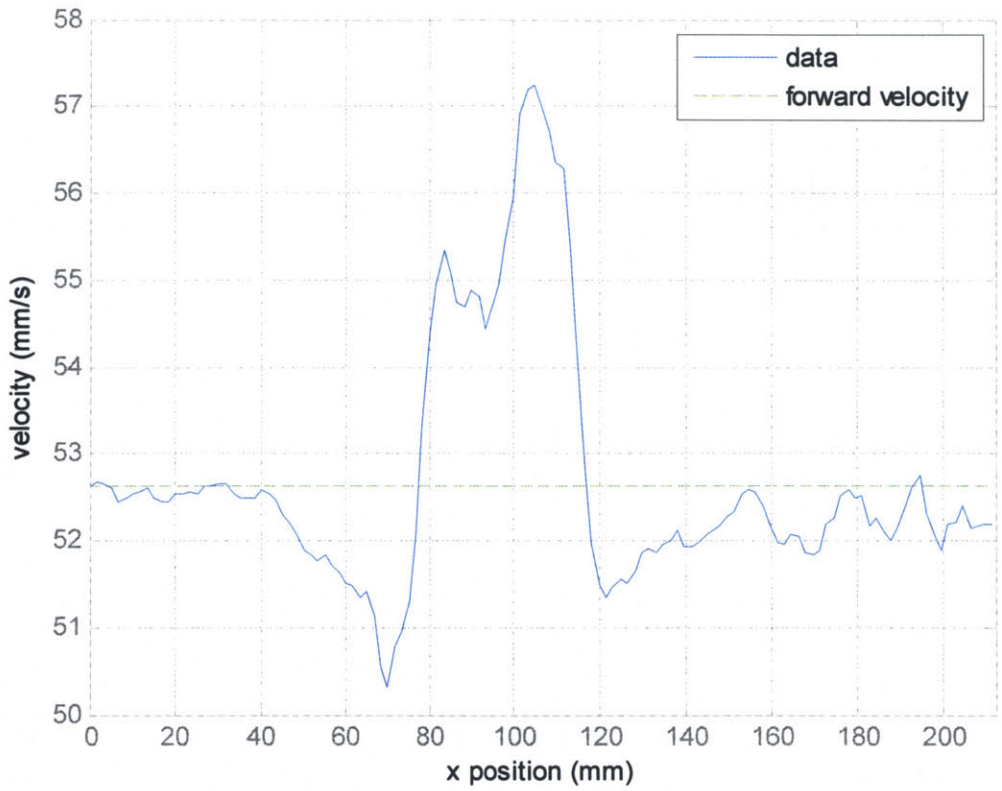

Figure 64: Phase averaged wake velocity profile for *Re=1000, St=0.2.*

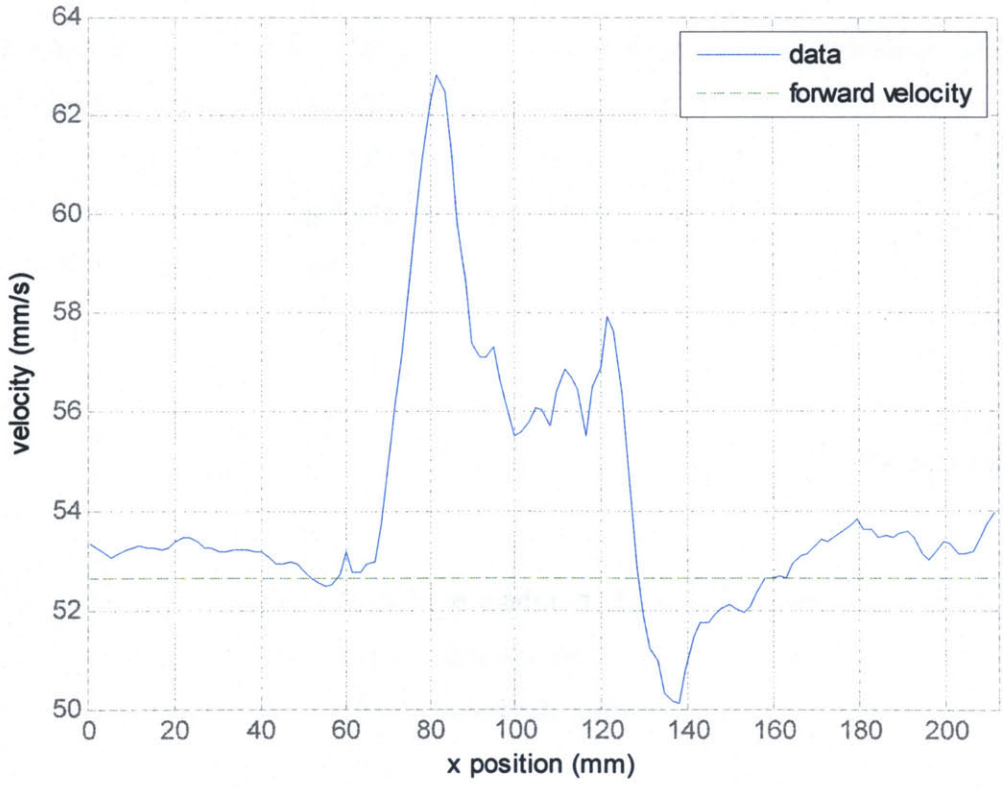

Figure 65: Phase averaged wake velocity profile for *Re=1000, St=0.4.*

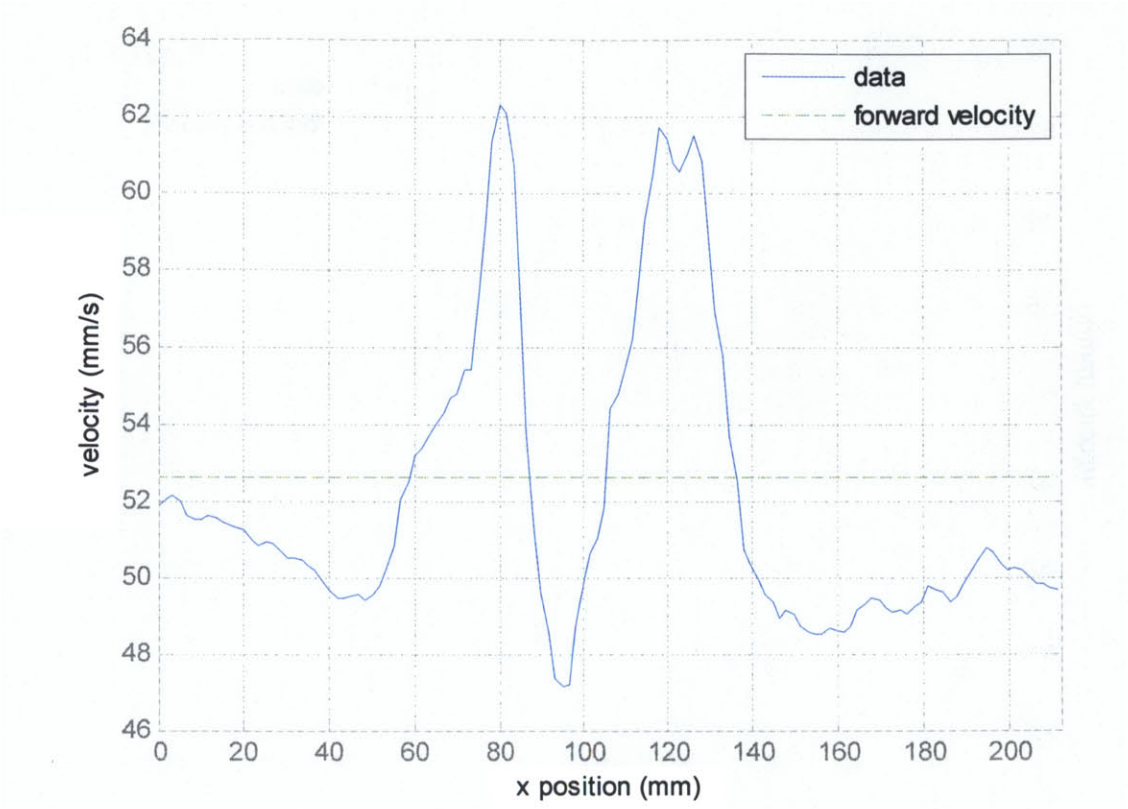

Figure 66: Phase averaged wake velocity profile for *Re=1000, St=0.8*.

The velocity profiles for *Re=1000* are somewhat different than the velocity profiles for the other Reynolds numbers. At *St=0.2*, the wake is already beginning to show signs of being a double jet wake. At *St=0.4*, the wake also exhibits the characteristics of a double jet wake. At *St=0.8*, the wake has not become shapeless, as it did in the other two cases. The two velocity peaks still remain but there is a strong area of drag between the two peaks.

5.5 Discussion

Though not enough Reynolds numbers have been evaluated to realistically talk about scaling laws, when these results are compared to the data seen in nature and other papers, there is a definite trend relating Reynolds number to Strouhal number at which maximum thrust is obtained.

Genera	*Median observed St*	*Re*
Dace, Trout, Goldfish	*0.30*	8×10^4
Dolphin	*0.30*	8×10^5
Bream	*0.32*	1×10^4
Bonito, Bluefish, Striped Mullet	*0.31*	6×10^4
Trout	*0.31*	2×10^4
Jack mackerel	*0.31*	2×10^5
Sockeye salmon	*0.26*	2×10^4
Bluefish	*0.35*	5×10^4
Cod	*0.30*	4×10^4
Blacktip shark	*0.25*	3×10^5
Saithe	*0.18*	6×10^5
Mackerel	*0.30*	1×10^6
Rainbow Trout	*0.32*	2.5×10^4

Table 7: Reynolds and Strouhal numbers for a variety of fish complied by Triantafyllou *et al.* (1993).

The majority of large fish swim at Strouhal numbers ranging from $St=0.25\text{-}0.35$ at Reynolds numbers on the order of $Re=10^4\text{-}10^6$. A survey of different breeds of fish and their respective Strouhal numbers and Reynolds numbers taken from Triantafyllou *et al.* (1993) is shown in table 7.

It should be noted that fish swim at the most efficient Strouhal number rather than the Strouhal number that creates the most thrust. In Anderson *et al.* (1998) the Strouhal number of peak efficiency was typically lower than the Strouhal number of highest thrust coefficient. This suggests that the Strouhal number of highest thrust for fish swimming is probably slightly higher than $St=0.3$. The highest thrust Strouhal number would probably be comparable to how fish swim when attempting to escape a predator.

On the other end of nature's spectrum are the copepods. These swimmers typically have a body length on the order of 1mm and swim at a Reynolds number of order $Re=1$ and a Strouhal number of approximately $St=5.0$ [Taylor *et al.*, 2003]. Though this is probably a Strouhal number of maximum efficiency as opposed to thrust, it is still interesting to look at this data in conjunction with the data for the larger fish and

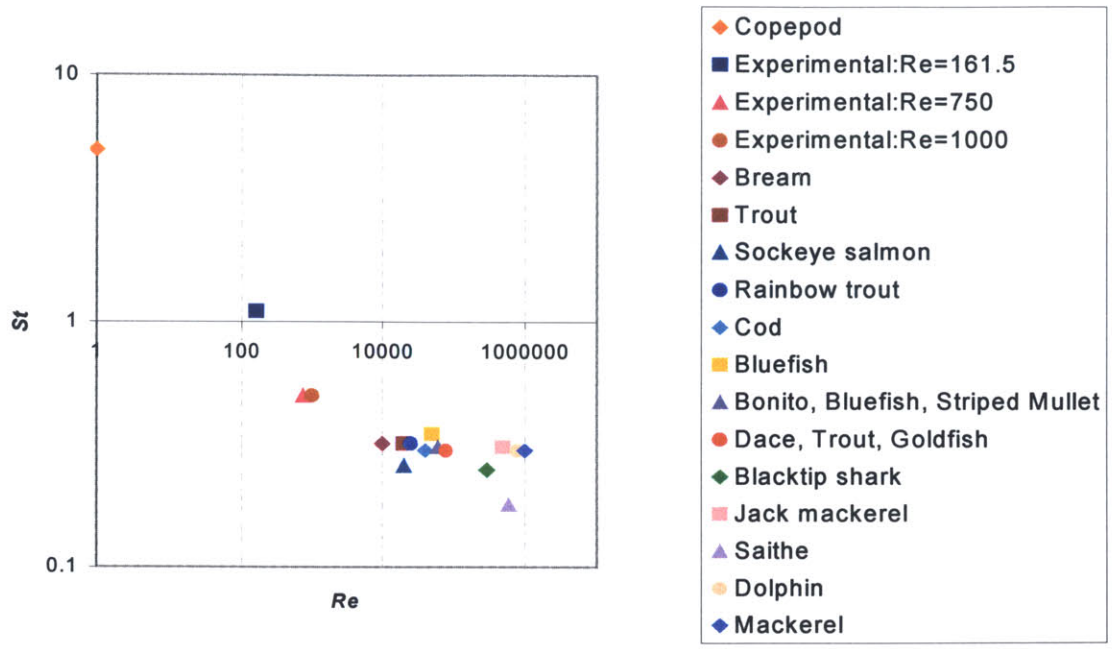

Figure 67: Key Strouhal numbers v. Reynolds number. For the experimental data, this plot is Strouhal number for maximum coefficient of thrust v. Reynolds number. For the fish data, this plot is typical Strouhal number for swimming v. Reynolds number.

the experimental data collected from the PIV experiments. These Strouhal numbers of maximum thrust for the PIV and Strouhal numbers typical for swimming in nature are plotted against Reynolds number in figure 67.

Although the experimental data is not directly comparable to the fish data since the experimental data represents Strouhal number at which maximum coefficient of thrust is achieved and the fish data represents typical Strouhal number seen in natural swimming, it is still very interesting that the Strouhal number decreases somewhat linearly with respect to Reynolds number when plotted on log-log axes. This suggests that the Strouhal number at which maximum thrust occurs varies significantly over a wide range of Reynolds numbers. Exactly how this varies is essential to know when designing flapping foil propulsion vehicles that must operate over a wide range of Reynolds numbers.

Although efficiency is not explicitly measured here, it makes sense to discuss the general trends seen in other experiments. In Anderson *et al.* (1998) the efficiency measured far exceeded the efficiency predicted by both linear and non-linear theory

suggesting that the higher order terms ignored in these calculations actually improve efficiency tremendously. Some efficiencies seen were over 80%. This suggests that it is entirely possible to design an efficient flapping foil propulsion vehicle. The data collected in the PIV experiments suggest that this type of vehicle could also generate high amounts of thrust. The way efficiency changes with Reynolds number and Strouhal number as collected by Anderson *et al.* (1998) coupled with the way thrust characteristics change with Reynolds number and Strouhal number from the data presented in this chapter combine to create a powerful way to analyze the performance of flapping foil propulsion. Though more work needs to be done, this promises to drastically simplify and improve the way flapping foil propulsive systems are designed.

Chapter 6

Impulsive Starts

6.1 Overview

The design of an AUV requires consideration of how the vehicle will start from rest as well as how it will perform under normal swimming conditions. Heaving and pitching a foil for one-half or one whole cycle without any forward velocity models the impulsive start of a flapping foil vehicle. Thrust can then be measured using the same control volume approach used in chapters 4 and 5.

6.2 Prior research

There has been a fair amount of research done on the topic of impulsive starting. Read *et al.* (2003) studied half cycle impulsive flaps with a maximum pitch angle of $\Phi=90°$. The maximum coefficients of thrust obtained by varying heave velocity, which also varied the frequency of the flap, appeared to be fairly independent of the heave velocity; however the instantaneous coefficient of thrust varied significantly over the period of the maneuver. Since the non-dimensional parameters, such as coefficient of thrust, are

traditionally defined using forward velocity, which in this case is zero, for this chapter C_t is defined as

$$Ct = \frac{\overline{T}}{\frac{1}{2}\rho U_h^2 cs} \qquad \textit{Eq. 14}$$

where U_h is the maximum heave velocity. This C_t was also used in Read *et al.* (2003). Since U_h is dependant on frequency it does not make sense to look at Strouhal number since it would be constant given a constant maximum heave amplitude. Reynolds number varies linearly with U_h.

The impulse generated by an impulsively started flapping foil is very similar to the impulsive generated by a vortex puff, such as those studied in Gharib *et al.* (1998). Since the dynamics of the single flap maneuver are primarily governed by the starting vortex, it makes sense to discuss these results in the context of vortex formation. Krueger and Gharib (2003) measured the thrust generated by vortices using PIV and the same control volume method used in chapter 4 to calculate thrust generated by flapping foils. They measured the thrust produced in the direction of vortex generation. However, to explore the forward thrust generated by a single flap of a flapping foil, it is necessary to measure the component of force in the direction of the desired foil motion.

The impulsive start has also been studied significantly with regard to live fish. While studying the maneuvering capabilities of the sunfish, Drucker and Lauder (1999) used another method of measuring thrust generated by a starting maneuver. Thrust was defined as

$$\overline{F} = \frac{p}{N\Psi}\sum_{n=1}^{N}\Gamma_n A_n \qquad \textit{Eq. 15}$$

where $\overline{F}$ is average force, N is the number of discreet measurements in one period, p is the fluid density, Ψ is the period, Γ is the circulation of the vortex and A is the area of the vortex in the plane perpendicular to the PIV plane. Drucker and Lauder (1999) estimate

the three-dimensional shape of the vortex to be donut shaped. Circulation is defined as

$$\Gamma = \int_A w \cdot dA \qquad \textit{Eq. 16}$$

where A is the area of the vortex and w is the vorticity at each point inside the area [Kundu and Cohen, 2004]. Two-dimensional vorticity is defined as

$$w = \frac{\partial V}{\partial x} - \frac{\partial U}{\partial y} \qquad \textit{Eq. 17}$$

where U is the velocity in the x-direction and V is the velocity in the y-direction. Vorticity is very easy to calculate from PIV. The trickier part of finding circulation in this way is defining the two-dimensional area of the vortex. Mohseni *et al.* (1991) defines this area as the contiguous area where vorticity was within two percent of the maximum vorticity of the vortex. This can be a misleading criterion because if the vortices are closely spaced two distinct vortices may be defined as one. The most difficult challenge with using this approach is defining A_n. Drucker and Lauder (1999) estimate the shape of the vortex as a donut and define the out of plane area accordingly.

6.3 Apparatus and Experimental Setup

PIV experiments were run using the same experimental set up used in chapters 4 and 5, which is shown in figure 30. The only difference was that the forward moving carriage was locked in place. The main purpose of performing these experiments was to observe the forces generated at the beginning of the impulsive maneuver. In order to calculate thrust, both the Krueger and Gharib (2003) and Drucker and Lauder (1999) methods were considered. The florescent dye visualizations showed that the wake of flapping foils of finite span is highly three-dimensional and fairly irregular. Since Drucker and Lauder (1999) relies on the out of plane area being predictable the Krueger and Gharib (2003)

Duration	f (Hz)	θ_o	Φ
half periof, full period	*0.1, 0.2, 0.3, 0.4, 0.5, 0.6, 0.7, 0.8, 0.9*	*5°*	*90°*
half periof, full period	*0.5*	*0°, 5°, 10°, 15°, 20°*	*90°*
half periof, full period	*0.5*	*5°*	*60°, 75°, 90°, 105°, 120°*

Table 8: Parameters varied for impulsive start experiments.

approach was chosen.

The parameters varied in the experiments were the frequency of the sinusoidal motion, the maximum pitch angle, the phase shift between heave and pitch, and whether or not the foil traveled a full period or half period. The combinations of parameter values used are listed in table 8.

6.4 Results

For each of the cases described in table 8, vorticity plots were created at even time intervals. Typically these were one-quarter period intervals for the full flap cases and one-eighth period intervals for the half flap cases. Since the PIV camera had a maximum frequency of 5.9 Hz., some of the higher frequency cases had to be sampled less often. Specifically, at frequencies greater than 0.8 Hz, full flap vorticity plots were created at one-third period intervals and half flap vorticity plots were created at one-sixth period intervals. The maximum coefficient of thrust during the time span of each full and half flap was also recorded. Figures 68 and 69 show vorticity plots for full and half flaps as Strouhal number is increased. The maximum coefficients of thrust for each of these cases are listed in tables 9 and 10. Figures 70 and 71 show vorticity plots for full and half flaps as maximum pitch angle is increased and their corresponding coefficients of thrust are listed in tables 11 and 12. Lastly, figures 72 and 73 show vorticity plots for full and half flaps as phase shift between heave and pitch is increased. The corresponding maximum coefficients of thrust are listed in tables 13 and 14.

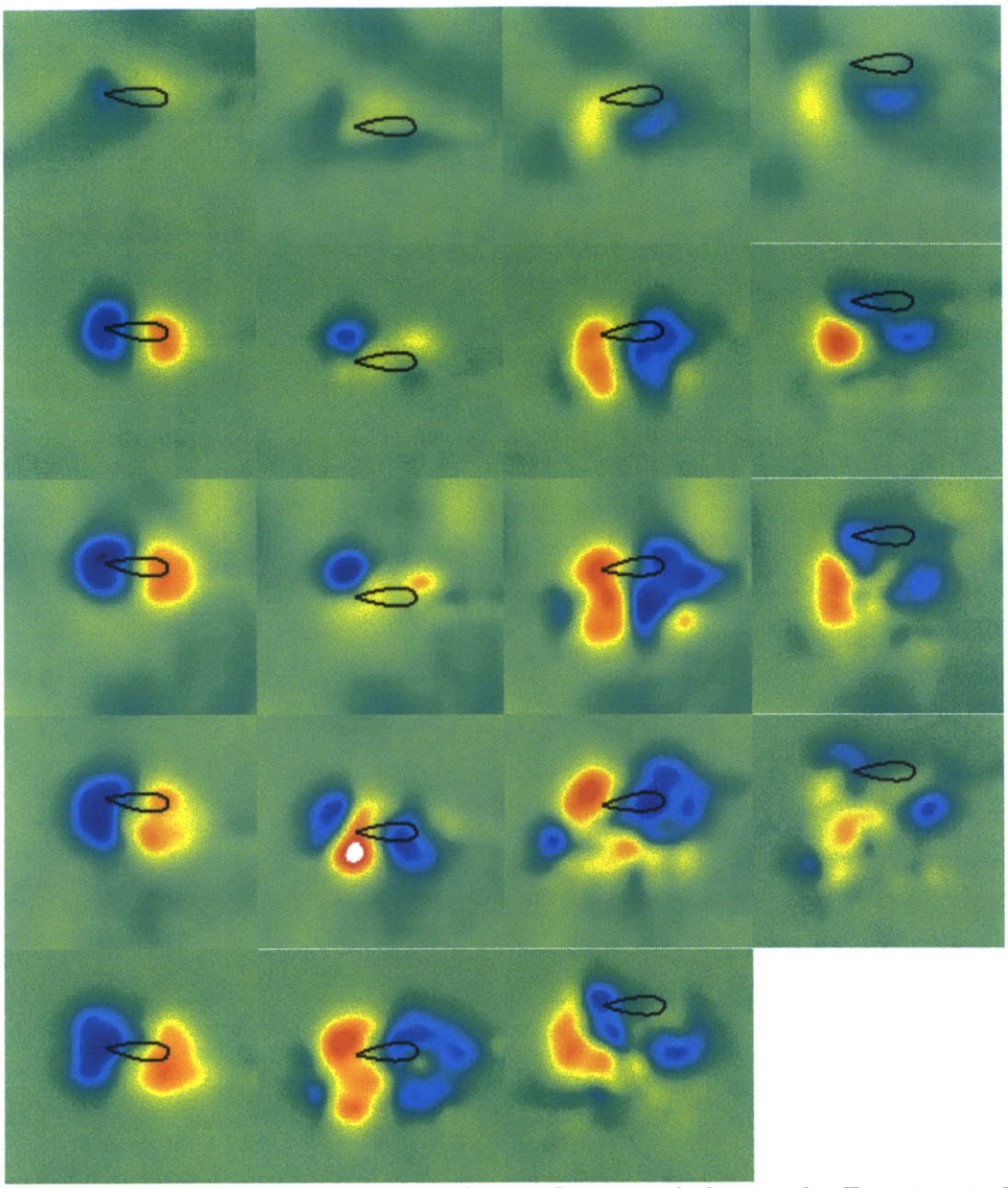

Figure 68: Vorticity plot of a single flap as frequency is increased. From top to bottom the frequencies are f=*0.1, 0.3, 0.5, 0.7,* and *0.9 Hz*. The foil is impulsively started at $\tau = -\pi/2$. For the first four cases, vorticity is shown *at* $\tau=0, \pi/2, \pi,$ and $3\pi/2$. For the last case, *f=0.9 Hz*, vorticity is shown at $\tau = \pi/6, 5\pi/6,$ *and* $3\pi/2$.

f (Hz)	C_t
0.1	*0.014*
0.2	*0.017*
0.3	*0.226*
0.4	*0.179*
0.5	*0.136*
0.6	*0.218*
0.7	*0.149*
0.8	*0.118*
0.9	*0.81*

Table 9: Maximum thrust coefficients seen over a full flap as frequency is increased.

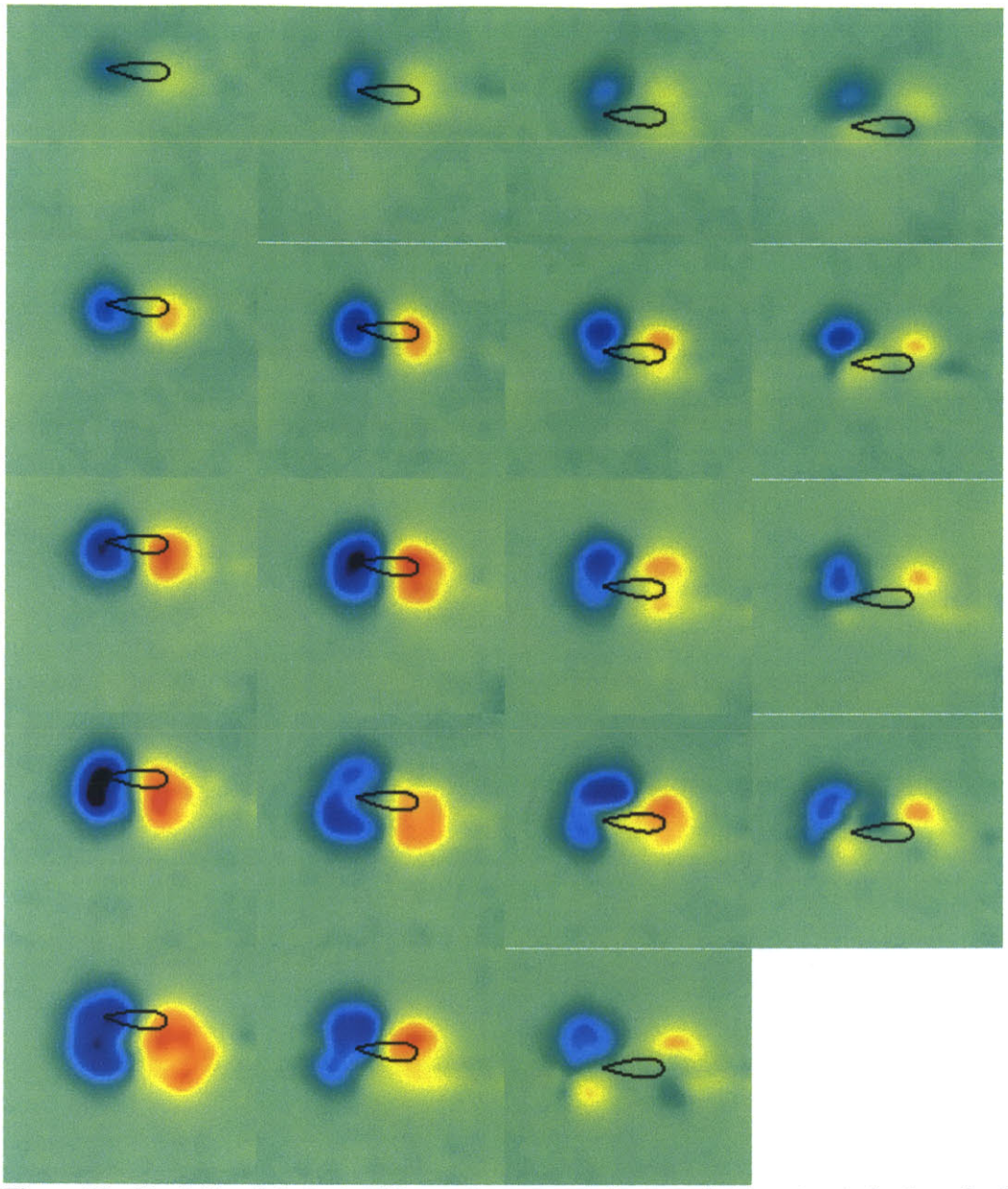

Figure 69: Vorticity plot of a half flap as frequency is increased. From top to bottom the frequencies are *f=0.1, 0.3, 0.5, 0.7,* and *0.9 Hz*. The foil is impulsively started at $\tau = -\pi/2$. For the first four cases, vorticity is shown at $\tau = -\pi/4$, *0*, $\pi/4$, and $\pi/2$. For the last case, *f=0.9 Hz*, vorticity is shown at $\tau = \pi/6$, $5\pi/6$, and $3\pi/2$.

f (Hz)	C_t
0.1	*-0.278*
0.2	*0.002*
0.3	*0.167*
0.4	*0.234*
0.5	*0.007*
0.6	*0.153*
0.7	*0.077*
0.8	*0.356*
0.9	*0.035*

Table 10: Maximum thrust coefficients seen over a half flap as frequency is increased.

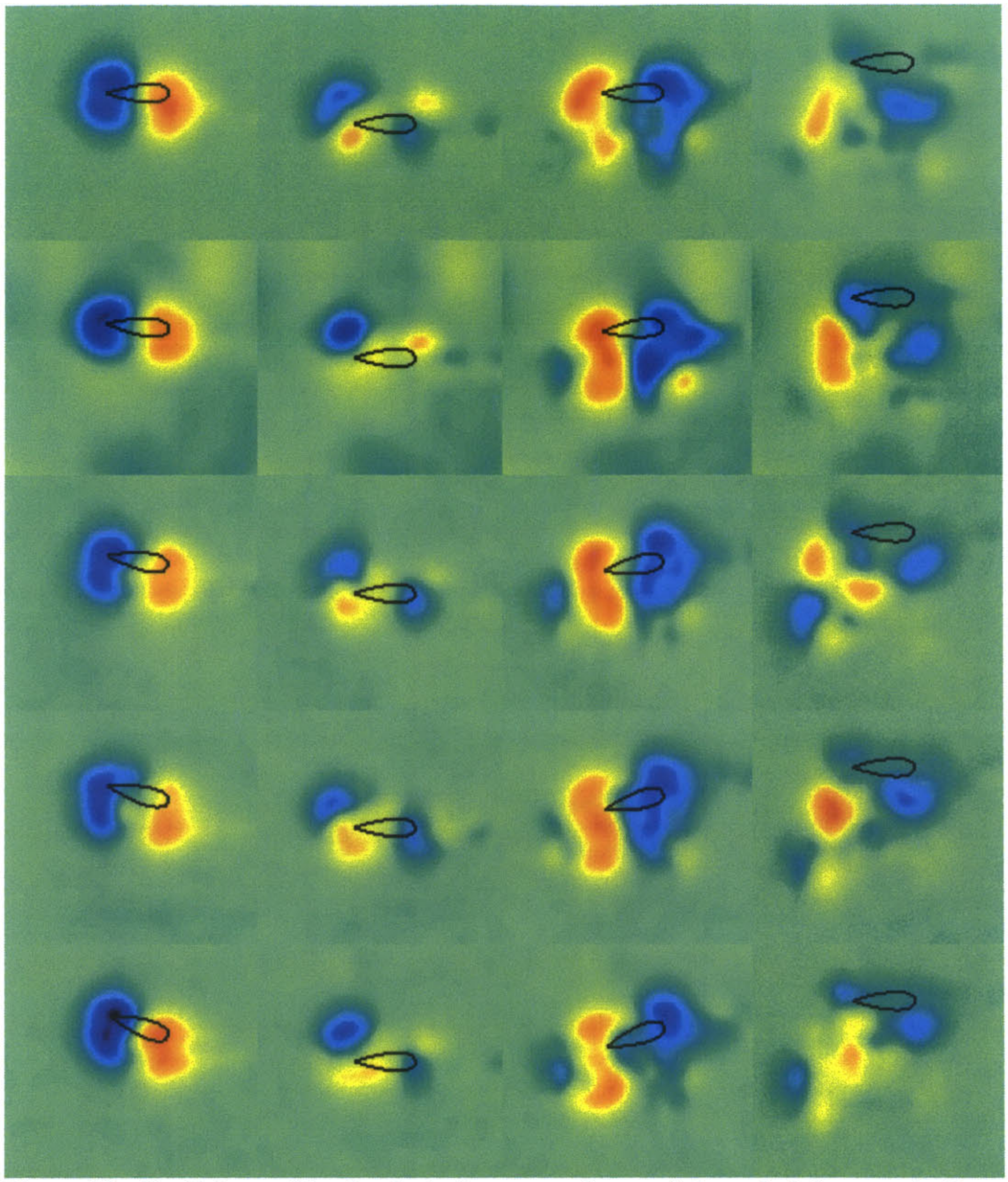

Figure 70: Vorticity profile of a single flap as maximum pitch angle is increased. From top to bottom the maximum pitch angle θ_o=0°, 5°, 10°, 15°, and 20°. The foil is impulsively started at τ=-π/2. For each case vorticity is shown at τ=0, π/2, π, and 3π/2.

θ_o	C_t
0°	0.008
5°	0.136
10°	0.059
15°	0.084
20°	0.108

Table 11: Maximum thrust coefficients seen over a full flap as maximum pitch angle is increased.

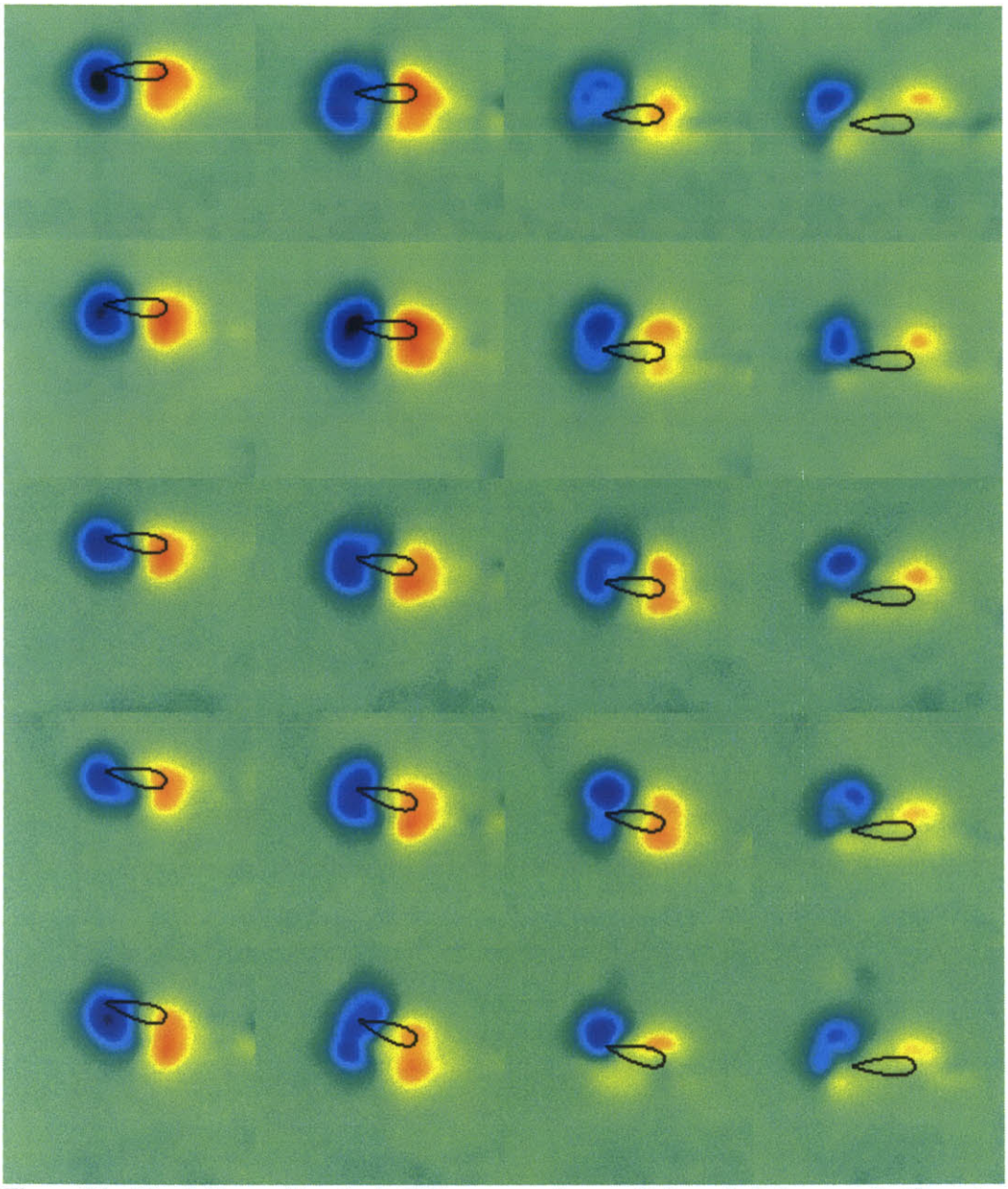

Figure 71: Vorticity profile of a half flap as maximum pitch angle is increased. From top to bottom the maximum pitch θ_o =0°, 5°, 10°, 15°, and 20°. The foil is impulsively started at τ=-π/2. For each case vorticity is shown at τ=- π/4, 0, π/4, and π/2.

θ_o	C_t
0°	0.005
5°	0.007
10°	0.053
15°	0.051
20°	0.090

Table 12: Maximum thrust coefficients seen over a half flap as maximum pitch angle is increased.

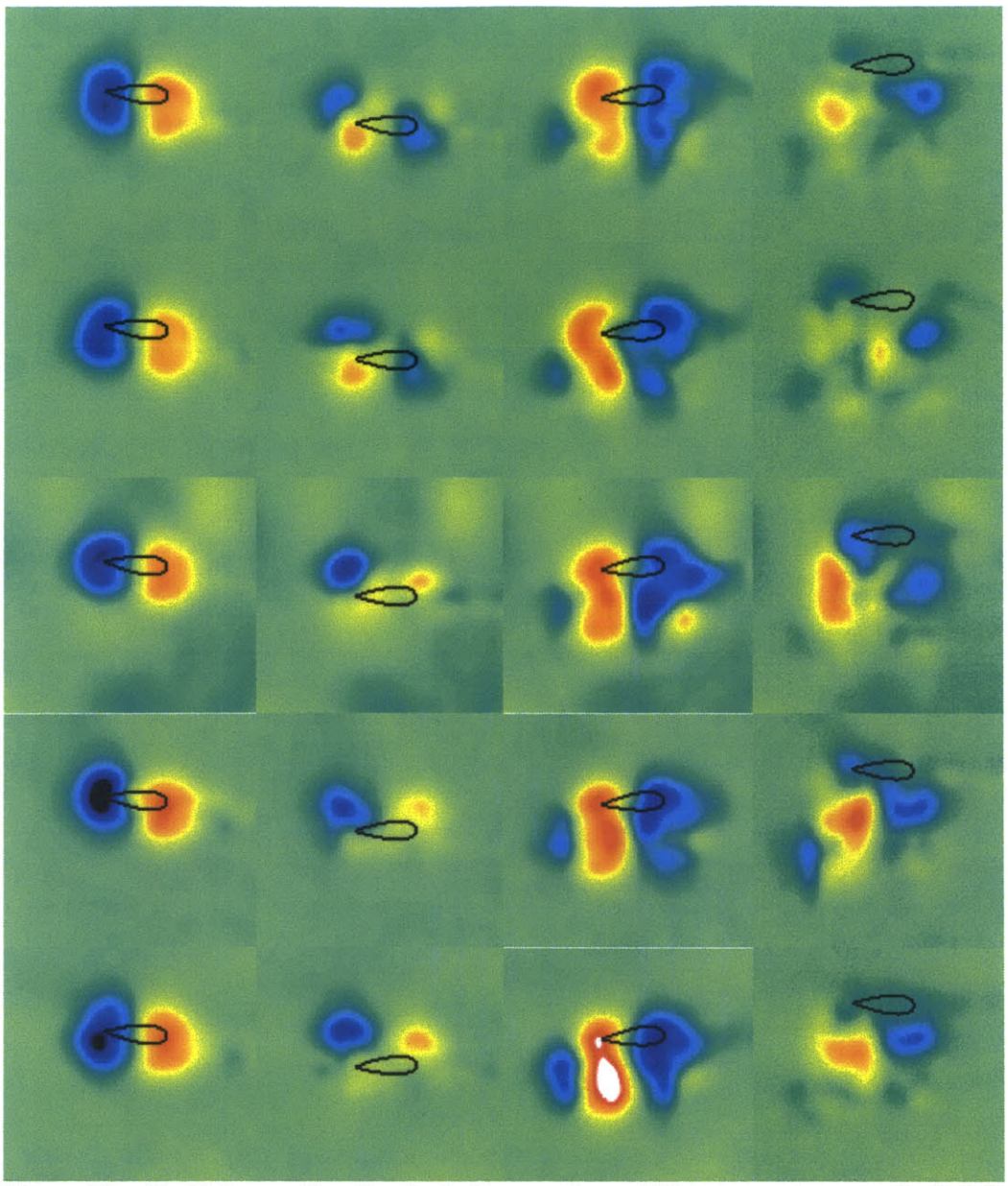

Figure 72: Vorticity profile of a single flap as phase shift between heave and pitch is increased. From top to bottom the phase shift $\Phi=60^\circ$, 75°, 90°, 105°, and 120°. The foil is impulsively started at $\tau=-\pi/2$. For each case vorticity is shown at $\tau=0$, $\pi/2$, π, and $3\pi/2$.

Φ	C_t
60°	0.060
75°	0.114
90°	0. 136
105°	0.117
120°	0.126

Table 13: Maximum thrust coefficients seen over one impulsively started full flap as phase shift is increased.

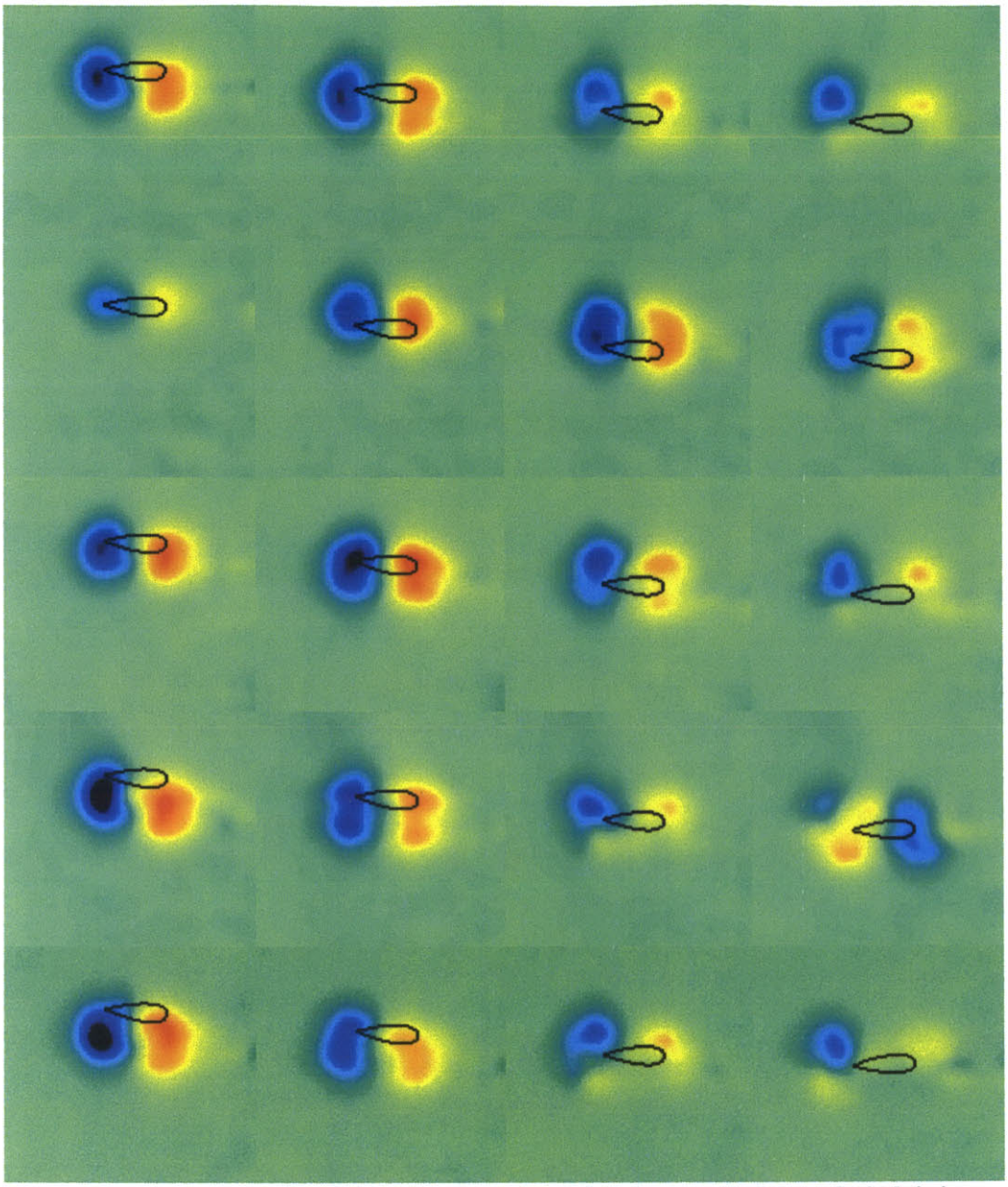

Figure 73: Vorticity profile of a half flap as phase shift between heave and pitch is increased. From top to bottom the phase shift $\Phi=60^{\circ}$, 75°, 90°, 105°, and 120°. The foil is impulsively started at $\tau=-\pi/2$. For each case vorticity is shown at $\tau=-\pi/4$, 0, $\pi/4$, and $\pi/2$.

Φ	C_t
60°	0.042
75°	0.030
90°	0. 007
105°	0.090
120°	0.130

Table 14: Maximum thrust coefficients seen over a half flap phase shift is increased.

6.5 Discussion

One major issue when looking at this data is the low frequency capability of the camera and the manual triggering. Although all the images are spaced evenly, the starting image can be up to one-twelfth of a period off for the higher frequency sequences. Because of this, the coefficients of thrust obtained are somewhat questionable. The reason maximum coefficient of thrust was displayed as opposed to a phase average coefficient of thrust was because the impulsive start is a transient maneuver; a phase average coefficient of thrust value would not be particularly meaningful [Read *et al.*, 2003].

For the full flapping foil, at very low frequencies the vorticity is on the low end, as shown in the images. This results in a low coefficient of thrust. As frequency increases, the strength of the vortices increase, though the coefficient of thrust seems to hit local maximums at $f=0.3$ *Hz* and $f=0.6$ *Hz*. This could be similar to the swimming case where there is an ideal Strouhal number for maximum thrust. However, this data could also be skewed because thrust was measured using a control volume bounded one chord length behind the foil. If the vortical structures had not yet developed enough to influence the velocity one-chord length behind the foil, than no thrust would be seen. A better way to measure this forward thrust would be to use a force transducer built into the shaft of the foil. It is also clear from the images that the vortex shed during the second half of the maneuver is much stronger than the vortex shed during the first half of the maneuver. The half flap case also sees two local maximums. These occur at $f=0.4$ *Hz* and $f=0.6$ *Hz*, close to where the local maximums occur during the full flap case. The half flap case only sheds one distinct vortex. There is no reason that the first half of the full flap maneuver should not be identical to the half flap maneuver. The maximum coefficients of thrust are much lower for the half flap case, confirming that the second vortex shed in the full flap is much stronger than the first. This suggests that an escape-type maneuver performed by a flapping foil propulsion AUV should use at least a full flap.

As maximum pitch angle is increased for the full flap case, coefficient of thrust generally increases. The exception is that the $\theta_o=5^\circ$ case has the highest coefficient of thrust. This is most likely due to the sampling point error introduced by manual

triggering and low sampling frequency. The coefficient of thrust also increases with maximum pitch angle for the half flap case. As with the increasing frequency cases, the maximum coefficient of thrust for the half flap case is lower than that for the corresponding full flap case, once again confirming that the second shed vortex in the full flap case is stronger than the first.

In the swimming cases, most of the results for altering the phase shift between heave and pitch have been symmetric about $\Phi=90^{\circ}$. That is to say that in general the $\Phi=60^{\circ}$ case behaved similarly to the $\Phi=120^{\circ}$ case. For the impulsively started full flap, that symmetry does not exist. Instead, coefficient of thrust seems to increase with phase shift. As previously stated, the second vortex shed is considerably stronger than the first. This asymmetry can be exploited by altering phase change. That is why the $\Phi=120^{\circ}$ case appears to be the strongest. In the half flap case, this asymmetry is not really seen. In fact there is no real trend to the half flap phase shift data. Perhaps this is because the initial vortex is not only weak, but also not as organized as the second. Therefore the thrust characteristics would be harder to predict.

6.6 Conclusions

The data suggests that a flap frequency of about $f=0.5$ *Hz* produces the most initial thrust along with a high maximum pitch angle. Also because of the unsteady asymmetries, higher thrust can be obtained by biasing the phase shift. Since the second shed vortex in the full flap maneuver is much stronger than the first, it makes sense to use a full flap as opposed to a half flap for rapid accelerations. Lastly, since the forces seen by Read *et al.* (2003) were much higher, it may be advantageous to look into flaps with much larger maximum pitch angles.

Chapter 7

Variations in Foil Shape

7.1 Overview

Though a NACA foil does a fairly good job of representing a fish tail, it is by no means identical to one. Fish fins have evolved over millions of years to become the efficient and versatile propulsors they are today. In order to improve the thrust characteristics and efficiencies of flapping foils, it makes sense to see what has been done in nature. This chapter looks the same experiments performed in chapters 5 and 6, but using a trout shaped foil, shown in figure 13, as opposed to the NACA 0030 foil.

7.2 Prior Research

Many biomimetic vehicles have been built which take advantage of biomimetic propulsors. Among these are "robo-tuna" [Anderson and Kerrebrock, 1997] and a turtle like flapping foil vehicle [Licht *et. al.*, 2004]. Others have attempted to incorporate the nuances of fish fins into more traditional flapping foil propulsors. It is thought that the flexibility of fish fins increases their efficiency so experiments have been done on flexible foils that can actively change their three-dimensional shape [Lauder *et al.*, 2005]. The trajectory of the foil has been looked at and it turns out small changes to the sinusoidal motion can result in non-trivial gains in efficiency [Hover *et al.*, 2004]. There is a vast quantity of examples of effective foil propulsors in nature and an equally massive amount of research being done in this area.

7.3 Experimental Parameters

In choosing the parameters to vary for the trout tail foil experiments, prior work was considered as well as the experiments discussed in chapters 5 and 6. Many of the robotic animals operated at much higher Reynolds numbers than the current test set up. Since time was a factor, making a complex form changing foil was not an option. The apparatus was only designed for sinusoidal motion so altering the kinematics as Hover *et al.* (2004) did was not an option. So it was decided to vary parameters similarly to the parameters chosen in the earlier chapters.

The first set of experiments were performed with the same apparatus and with the same parameters varied as the heaving and pitching experiments of chapter 5. The trout tail foil, shown in figure 13, was used at a Reynolds number of $Re=1000$. Strouhal number, maximum pitch angle, and phase shift were varied. The values chosen for each of these variables are listed in table 15.

The second set of experiments replicated the half and full flap experiments performed in chapter 6. These experiments varied flap frequency, maximum pitch angle, and phase shift between heave and pitch. They used the exact same values used in the experiments in chapter 6. These values are listed in table 16.

St	θ_o	Φ
0.44, 0.66, 0.87, 1.09, 1.31, 1.53, 1.75	*5°*	*90°*
1.09	*0°, 5°, 10°, 15°, 20°*	*90°*
1.09	*5°*	*60°, 75°, 90°, 105°, 120°*

Table 15: Experimental parameters for pitching and heaving trout tail foil experiments.

Duration	*f*	θ_o	Φ
half periof, full period	*0.1, 0.2, 0.3, 0.4, 0.5, 0.6, 0.7, 0.8, 0.9*	*5°*	*90°*
half periof, full period	*0.5*	*0°, 5°, 10°, 15°, 20°*	*90°*
half periof, full period	*0.5*	*5°*	*60°, 75°, 90°, 105°, 120°*

Table 16: Parameters varied for trout tail foil impulsive start experiments.

7.4 Results and Discussion

The velocity vectors and vorticity plots for a select few of the swimming trout cases are shown in figure 74 with their corresponding phase average coefficients of thrust listed in table 17. The vorticity plots for time sequences of various full and half flap maneuvers are shown in figures 75 through 80. The maximum coefficients of thrust for each of these cases are listed in tables 18 through 23.

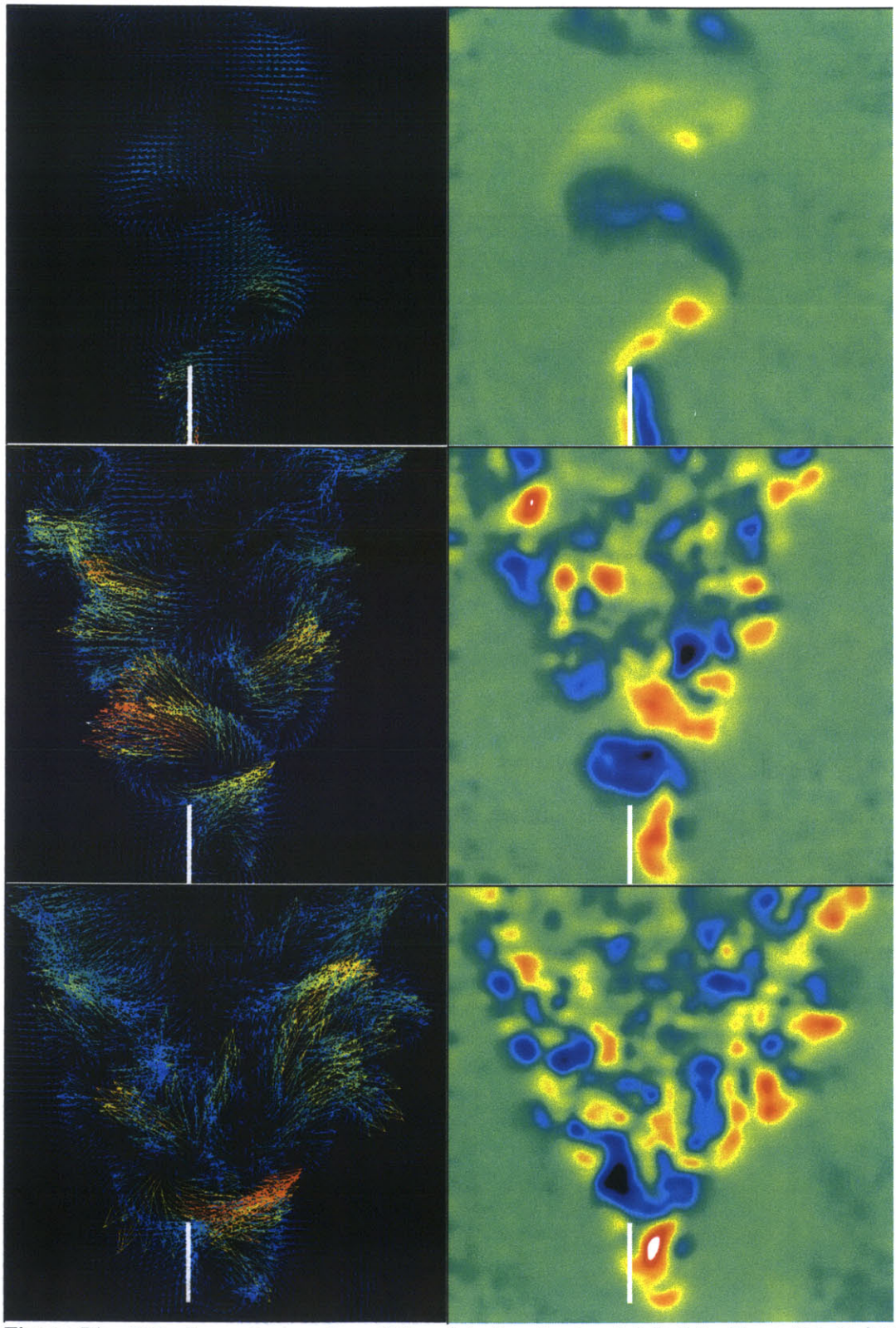

Figure 74: Velocity vectors and vorticity plots for the trout tail foil From top to bottom the frequencies shown are *f=0.2, 0.5, and 0.8 Hz.*

St	C_t
0.437	*0*
0.655	*-0.462*
0.873	*0.481*
1.092	*1.360*
1.310	*1.014*
1.528	*2.026*
1.747	*1.694*

Table 17: Phase averaged coefficients of thrust for a heaving and pitching trout tail foil for various Strouhal numbers.

During the forward swimming experiments, the trout foil seemed to go through the same three wake morphologies seen in the NACA foil experiments. At lower Strouhal numbers, an 'S' wake is seen, at moderate Strouhal numbers, a double jet wake is seen, and at high Strouhal numbers, the double jet wake begins to break up. The curious thing is that for the NACA foil *Re=1000* case, the Strouhal number of maximum thrust was *St=0.5* where as for the trout foil, also at *Re=1000*, the Strouhal number at which the maximum coefficient of thrust is seen is about *St=1.5*. This discrepancy suggests that Strouhal number of maximum thrust does not scale directly with Reynolds number but is also dependant on other parameters.

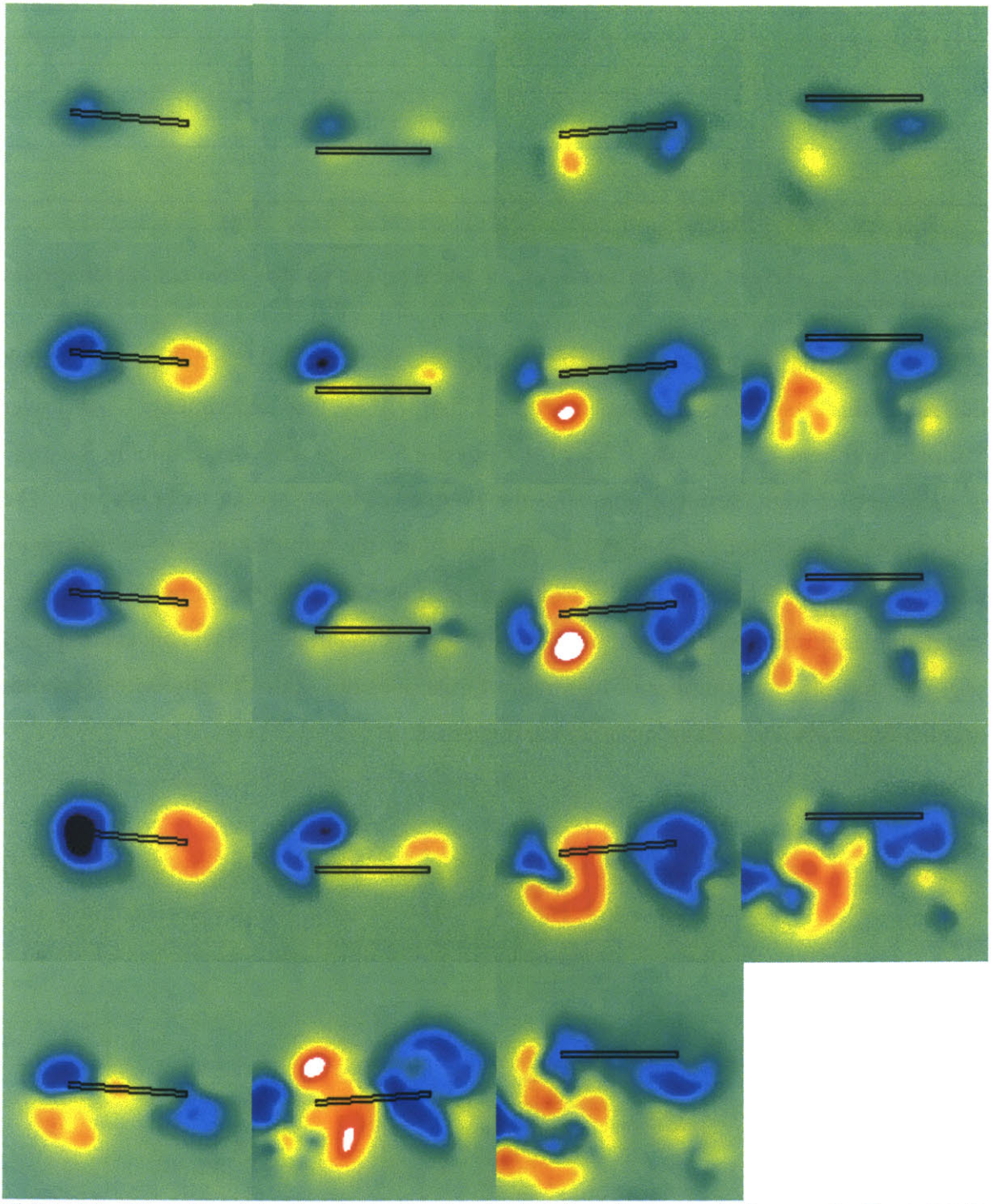

Figure 75: Vorticity plots of a single flap trout tail foil as frequency is increased. From top to bottom the frequencies are *f=0.1, 0.3, 0.5, 0.7,* and *0.9 Hz.* The foil is impulsively started at $\tau = -\pi/2$. For the first four cases, vorticity is shown at τ=0, $\pi/2$, π, and $3\pi/2$. For the last case, *f=0.9 Hz,* vorticity is shown at $\tau = \pi/6$, $5\pi/6$, and $3\pi/2$.

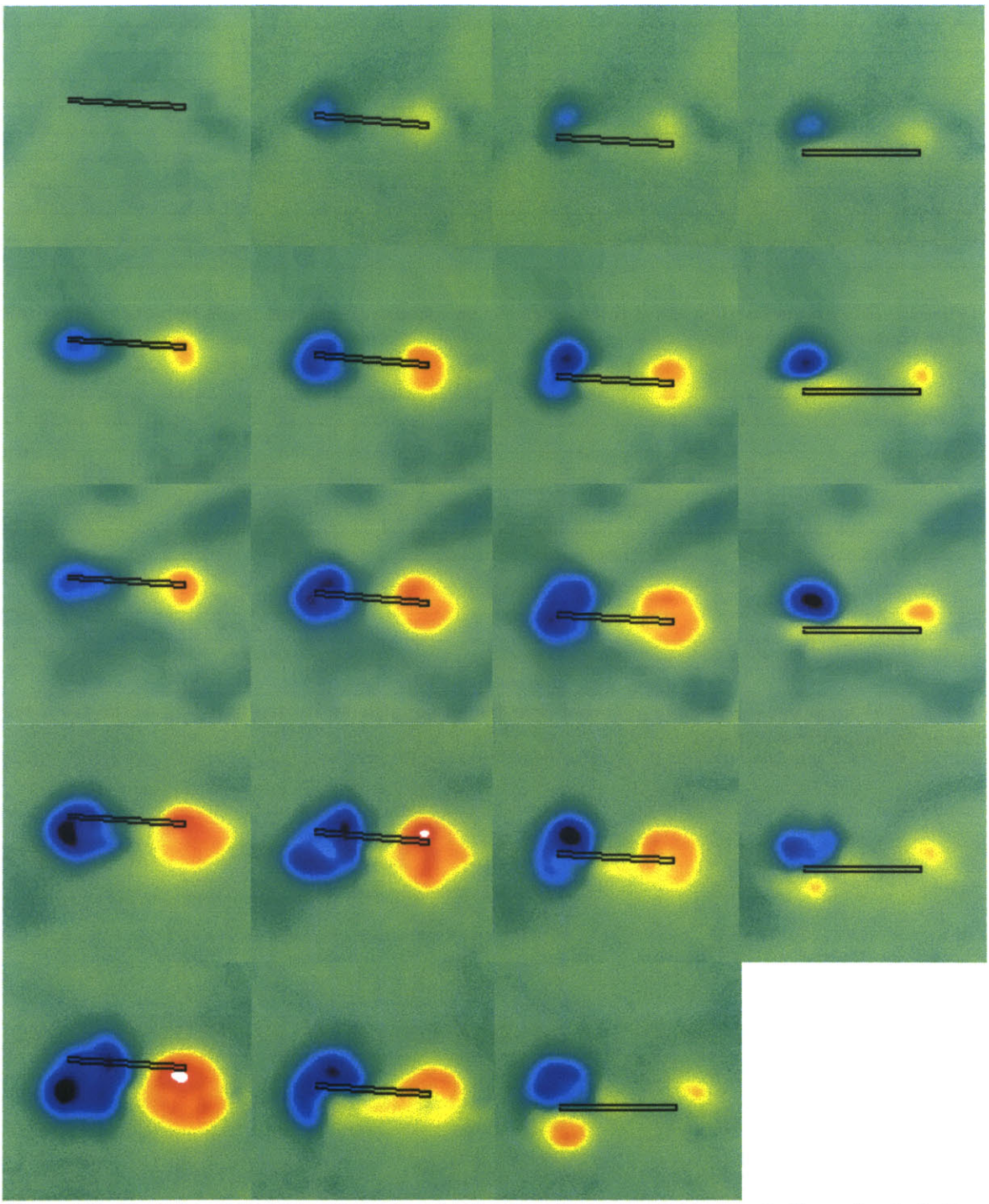

Figure 76: Vorticity plots of a half flap trout tail foil as frequency is increased. From top to bottom the frequencies are *f=0.1, 0.3, 0.5, 0.7,* and *0.9 Hz*. The foil is impulsively started at $\tau = -\pi/2$. For the first four cases, vorticity is shown at $\tau = -\pi/4$, 0, $\pi/4$, and $\pi/2$. For the last case, *f=0.9 Hz*, vorticity is shown at $\tau = \pi/6$, $5\pi/6$, and $3\pi/2$.

f	C_t
0.1	*-0.135*
0.2	*0.254*
0.3	*0.827*
0.4	*0.466*
0.5	*0.438*
0.6	*0.835*
0.7	*0.242*
0.8	*0.254*
0.9	*0.188*

Table 18: Maximum coefficients of thrust seen for an impulsively started single flap of the trout tail foil as frequency is increased.

f	C_t
0.1	*0.160*
0.2	*-0.027*
0.3	*0.088*
0.4	*0.519*
0.5	*0.081*
0.6	*0.178*
0.7	*0.080*
0.8	*0.210*
0.9	*0.142*

Table 19: Maximum coefficients of thrust seen for an impulsively started half flap of the trout tail foil as frequency is increased.

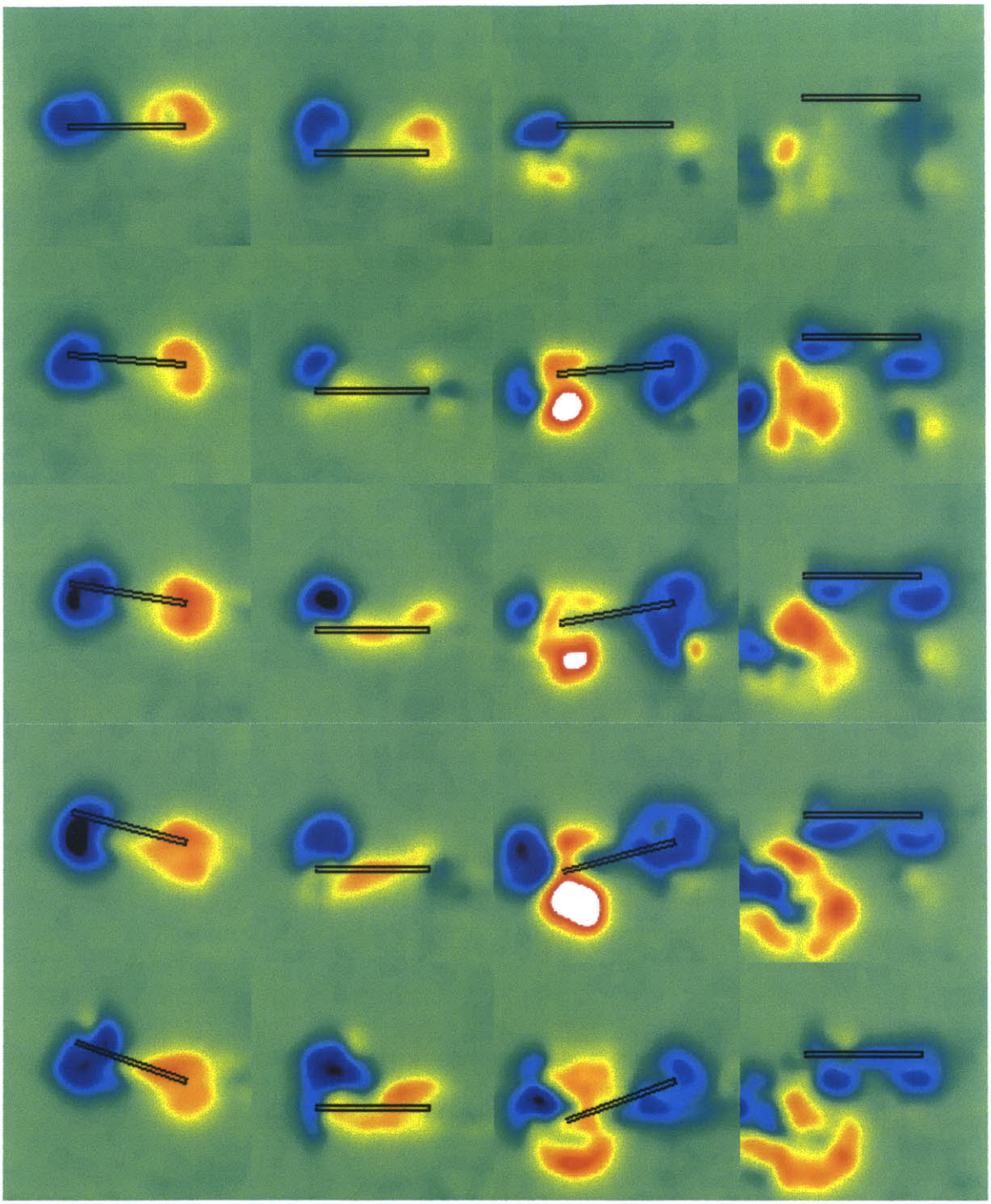

Figure 77: Vorticity plots of a single flap trout tail foil as maximum pitch angle is increased. From top to bottom the maximum pitch angle θ_o=0°, 5°, 10°, 15°, and 20°. The foil is impulsively started at τ=-π/2. For each case vorticity is shown at τ=0, π/2, π, and 3π/2.

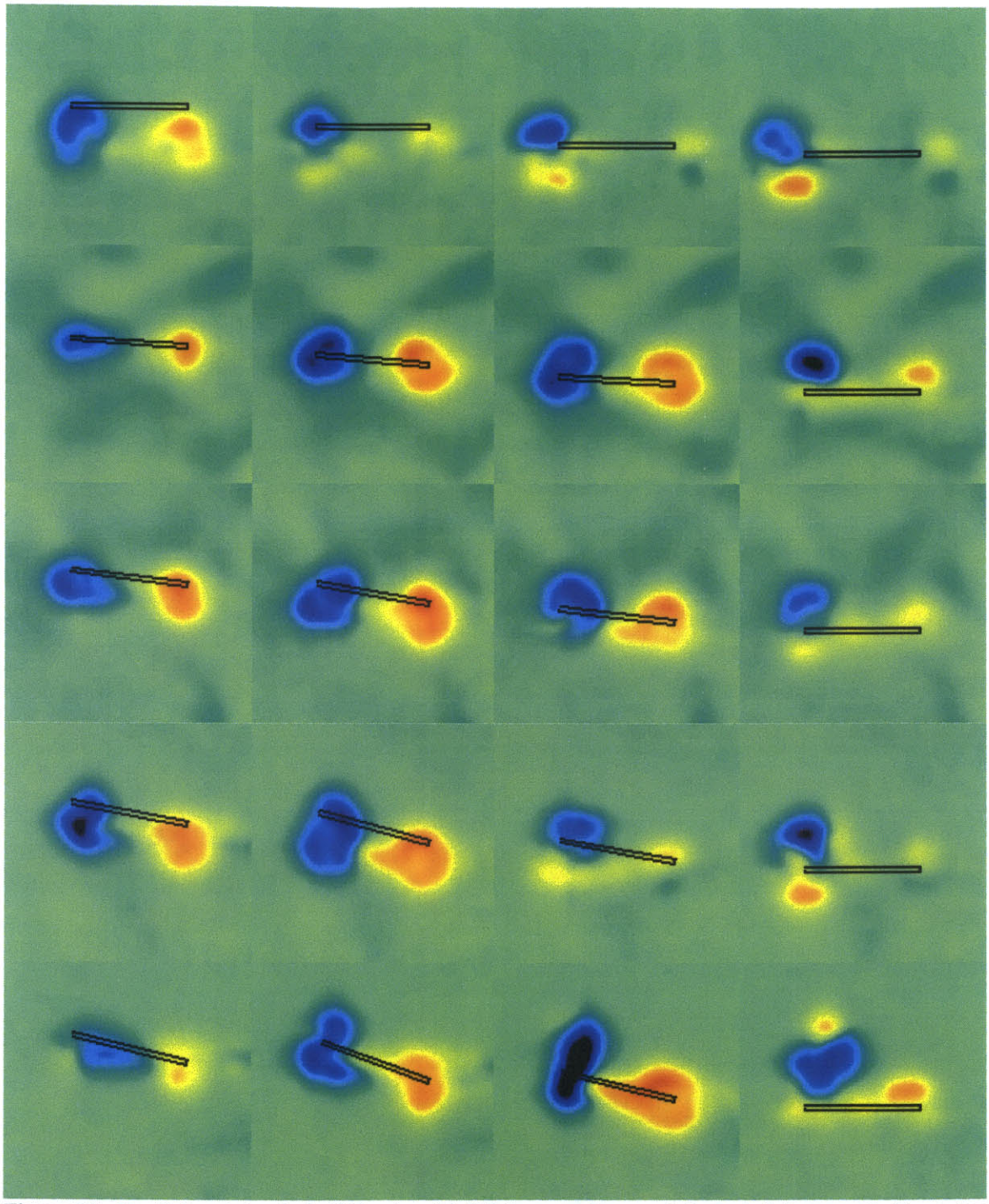

Figure 78: Vorticity plots of a half flap trout tail foil as maximum pitch angle is increased. From top to bottom the maximum pitch angle θ_o=0°, 5°, 10°, 15°, and 20°. The foil is impulsively started at τ= $\pi/2$. For each case vorticity is shown at τ= $\pi/4$, 0, $\pi/4$, $\pi/2$.

θ_o	C_t
0°	0.255
5°	0.438
10°	0.539
15°	1.530
20°	0.708

Table 20: Maximum coefficients of thrust seen for an impulsively started single flap of the trout tail foil as maximum pitch angle is increased.

θ_o	C_t
0°	0.255
5°	0.081
10°	0.146
15°	0.393
20°	0.303

Table 21: Maximum coefficients of thrust seen for an impulsively started half flap of the trout tail foil as maximum pitch angle is increased.

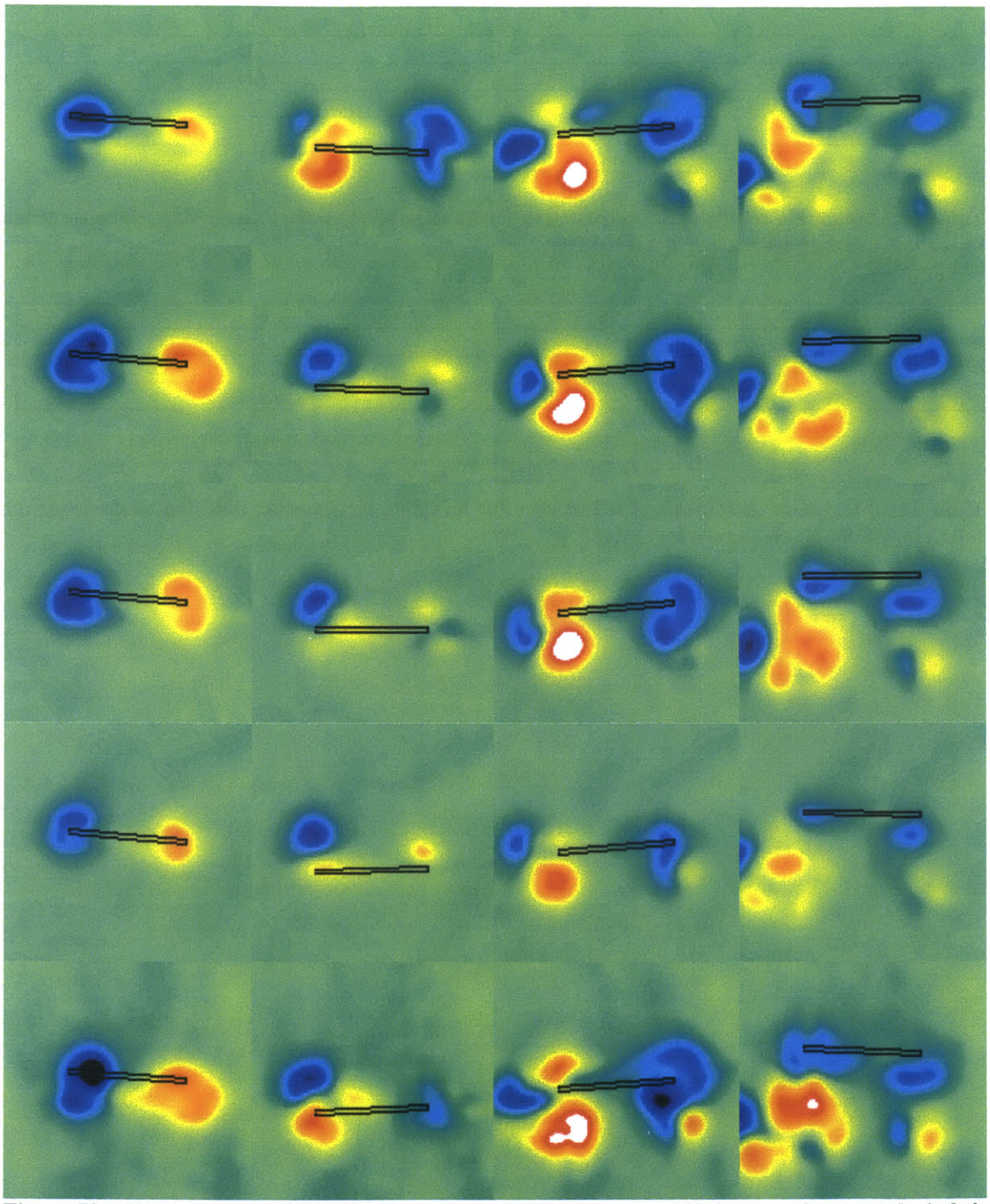

Figure 79: Vorticity plots of a single flap trout tail foil as phase shift between heave and pitch is increased. From top to bottom the phase *shift* Φ=60°, 75°, 90°, 105°, and 120°. The foil is impulsively started at τ=-π/2. For each case vorticity is shown at τ=0, π/2, π, and 3π/2.

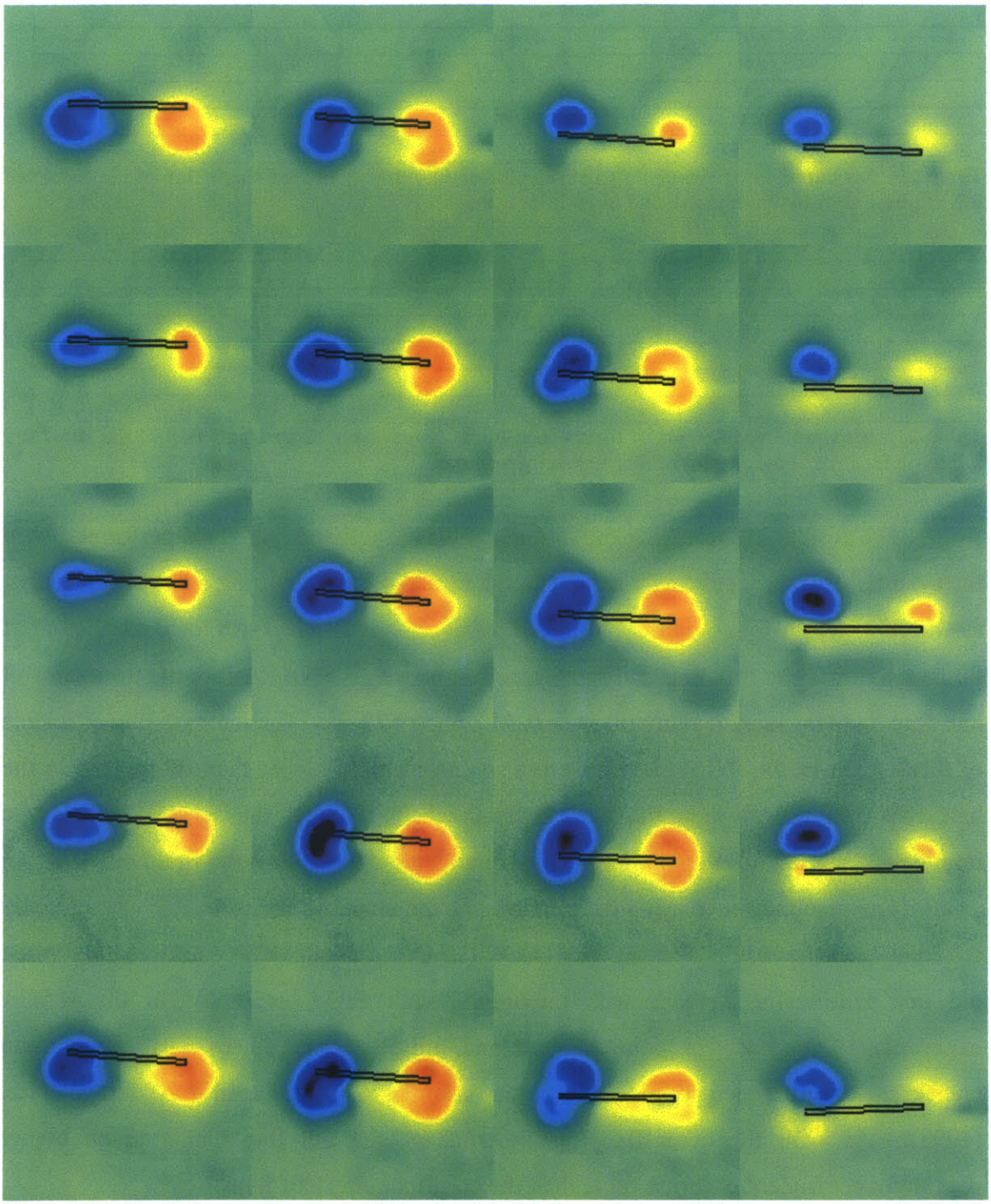

Figure 80: Vorticity profile of a half flap trout tail foil as phase shift between heave and pitch is increased. From top to bottom the phase shift *Φ=60°, 75°, 90°, 105°*, and *120°*. The foil is impulsively started at $\tau=-\pi/2$. For each case vorticity is shown at $\tau=-\pi/4$, 0, $\pi/4$, and $\pi/2$.

Φ	C_t
60°	0.645
75°	0.896
90°	0.438
105°	0.203
120°	0.458

Table 22: Maximum coefficients of thrust seen for an impulsively started single flap of the trout tail foil as phase shift between heave and pitch is increased.

Φ	C_t
60°	0.078
75°	0.066
90°	0.081
105°	0.168
120°	0.176

Table 23: Maximum coefficients of thrust seen for an impulsively started half flap of the trout tail foil as phase shift between heave and pitch is increased.

The results of increasing the frequency for the full and half flaps performed with the trout tail foil were strikingly similar to the results seen when using a NACA foil. Just as with the NACA foil, the trout tail foil impulsive single flap had two local coefficient of thrust maximums at f=0.3 *Hz* and f=0.6 *Hz*. Just as with the NACA foil, the trout tail foil half flap had two local maximums at f=*0.4 Hz* and f=*0.6 Hz*. The maximum coefficients of thrust seen in the full flap case were also considerably higher than those seen in the half flap case, confirming the hypothesis in chapter 6 that the second half of the impulsively started full flap produces considerably more thrust than the first half.

The results of increasing the maximum pitch angle for the trout foil were slightly different than the results seen in the NACA foil experiments. The coefficient of thrust did not continually increase with maximum pitch angle, as it did in the NACA experiments. Instead, for both the half and full flap cases, there was a maximum coefficient of thrust seen at the θ_o=*15*° case. A similar result was seen in Anderson *et al.*, (1998). As with the other flapping experiments, the full flap had a much higher maximum coefficient of thrust value than the corresponding half flaps.

The results of increasing the phase shift between heave and pitch for the flapping trout foil were somewhat puzzling. In the NACA experiments, the full flap cases showed a bias towards higher phase shifts, with the maximum coefficient of thrust coming at the Φ=120° case, whereas the half flap case showed no noticeable trends. The reverse appears to be true for the trout foil experiments. In the NACA foil experiments, the half

flap shows a clear thrust producing bias towards higher phase shifts, whereas the results of changing phase shift in the full flap case are unclear.

7.5 Conclusions

This chapter, though relatively brief, offered various insights that apply to the other experiments described in this thesis. The first is that the Strouhal number of maximum thrust does not scale directly with Reynolds number based on chord length, but is also dependent on other parameters. The second is that for certain foil shapes, there may be an ideal maximum pitch angle for thrust production. The last conclusion of this chapter is that although there are definite asymmetries in the impulsively started maneuvers, how best to exploit them varies. The full flap showed increased performance with phase delays for the NACA foil, whereas only the half flap showed any increase in thrust production due to large phase delays for the trout tail foil. This chapter also confirmed the three wake morphologies seen in chapter 5 and the conclusion in chapter 6 that impulsively started single flaps produce far more thrust than impulsively started half flaps.

Chapter 8

Conclusions

8.1 Summary

This thesis has explored various phenomena relating to flapping foil propulsion at Reynolds numbers ranging from Re=100 to Re=1000. An elegant mechanism for performing heaving and pitching experiments was developed. Fluorescent dye visualizations were performed to determine three-dimensional wake morphologies. PIV was performed to measure thrust characteristics, wake vorticity, and further understand wake morphology. Experiments were performed to measure the thrust characteristics of various types of impulsive starts. Many of these experiments were performed on both a NACA 0030 foil and a biomimetic trout tail shaped foil and the results from each type of foil were compared.

The fluorescent dye visualizations confirmed that at low Reynolds number Re=161.5 and Strouhal numbers of about St=0.2, there is a 'S' shaped wake but as Strouhal number increases through about St=0.4, the wake develops relatively discreet vortices which are horseshoe-shaped. This is confirmed by the wake structure predicted by Blondeaux *et al.* (2005) and simultaneously casts doubt on the wake structure proposed by von Ellenrieder *et al.* (2003).

PIV performed on the same cases subjected to dye visualizations showed that none of these cases produced thrust wakes. It also measured vorticity and showed it to be virtually identical to the vorticity predicted by Blondeaux *et al.* (2005). This further confirmed the fluorescent dye visualization results while dismissing the question of whether or not the dye significantly impacted the flow.

PIV performed at higher Strouhal numbers at a variety of Reynolds numbers lead to the discovery that for each Reynolds number there was a Strouhal number that produced a maximum coefficient of thrust. This Strouhal number of maximum thrust appears to vary linearly with Reynolds number when plotted on a log-log scale and fits in well with data taken from nature, ranging from the tiny copepods to the fast-swimming dolphins.

The half and full flap maneuvers modeled impulsive starts. All of the results seemed to suggest that the full flap has a lot more thrust producing capability than the half flap. There seems to be a frequency at which coefficient of thrust is maximized, just as the swimming case has a Strouhal number at which the coefficient of thrust is maximized. The results also suggest that a larger maximum pitch angle is beneficial for thrust production and that the asymmetries introduced by the unsteady nature of the maneuver can be exploited by biasing the phase shift between heave and pitch.

The experiments performed on the trout shaped foil add a new dimension to how the results of the previous experiments are interpreted. First, since the Strouhal number of maximum thrust for the trout tail foil swimming case is significantly higher than the swimming case at the same Reynolds number for the NACA foil, this maximum thrust Strouhal number must be dependant on more than just Reynolds number defined by chord length. Also this foil appears to have a maximum pitch angle of maximum thrust, whereas the NACA did not over the range studied. Also, it appears the phase shift biasing works in a slightly different manner for the trout tail foil than it does for the NACA foil.

Overall this research makes significant headway into developing a set of scaling laws for designing flapping foil propulsion systems. Much is still left to be done and is discussed in the following section.

8.2 Recommendations for Further Research

Virtually every area of this thesis leaves room for further work to be done. First of all, the mechanism, though elegant, is not very flexible and is very difficult to calibrate.

Therefore it is suggested that future work use separate motors for heave and pitch with feedback control that can be synchronized with the laser and camera.

It would be very interesting to see the results of fluorescent dye visualizations at higher Reynolds and Strouhal numbers. This requires developing a new type of dye that will not dissolve at higher speeds.

The coefficient of thrust results for the PIV should be repeated and verified. Also a forced transducer should be installed on the new mechanism so that efficiencies can be measured. A wider range of Reynolds numbers should be studied to confirm the relationship between maximum thrust Strouhal number and Reynolds number.

The half and single flap maneuvers should be repeated with a higher sampling frequency while being triggered along with the laser to avoid any phase delay errors. These experiments should be repeated in order to confirm them.

Lastly, since the trout tail foil results varied significantly from the NACA 0030 foil results, it is recommended that a wide range of foil shapes and sizes be tested to determine what other parameters influence the way thrust characteristics scale.

References

[1] Anderson, J. (1996) "Vorticity control for efficient propulsion," Ph.D. Thesis, Massachusetts Institute of Technology.

[2] Anderson, J. and Kerrebrock, P. (1997) "Vorticity control unmanned undersea vehicle (VCUUV) - an autonomous vehicle employing fish swimming propulsion and maneuvering," *Proceedings of the International Symposium on Unmanned Untethered Submersible Technology*, pp. 189-195.

[3] Anderson, J., Streitlien, K., Barrett, D., and Triantafyllou, M. (1998) "Oscillating foils of high propulsive efficiency," *Journal of Fluid Mechanics,* Vo. 360, pp. 41-72.

[4] Blake, R. (1983) *Fish Locomotion,* Cambridge University Press.

[5] Blondeaux, P., Fornarelli, F., Gugluelmini, L., Triantafyllou, M., and Verzicco, R. (2005) "Vortex structures generated by a finite-span oscillating foil," *Proceedings of the 43rd AIAA Aerospace Sciences Meeting and Exhibit.*

[6] Breder, C. (1926) "The locomotion of fishes," *Zoologica*, Vol. 4, pp. 159-256.

[7] Drucker, E. and Lauder, G. (1999) "Locomotor forces on a swimming fish: three-dimensional vortex wake dynamics quantified using digital particle image velocimetry," *The Journal of Experimental Biology,* Vol. 202, pp. 2393-2412.

[8] Freymouth, P. (1989) "Visualizing the connectivity of vortex systems for pitching wings," *Journal of Fluids Engineering,* Vol. 111, pp. 217-220.

[9] Gharib, M., Rambod, E., and Shariff, K. (1998) "A universal time scale for vortex ring formation," *Journal of Fluid Mechanics,* Vol. 260, pp. 121-140.

[10] Gharib, C. and Willart. (1991) "Digital particle image velocimetry," *Experiments in Fluids*, Vol. 10, pp. 181-193

[11] Guglielmini, L. and Blondeaux, P. (2004) "Propulsive efficiency of oscillating foils," *European Journal of Mechanics B: Fluids,* Vol. 34, 2004, pp. 255-278.

[12] Hover F., Haugsdal, O., Triantafyllou, M. (2004) "Effect of angle of attack profiles in flapping foil propulsion," *Journal of Fluids and Structures,* Vol. 19, pp. 37-47.

[13] Krueger, M. (2005) "Three-dimensional vortical structures in the wake of a flexible foil," S.B. Thesis, Massachusetts Institute of Technology.

[14] Krueger, P. and Gharib, M. (2003) "The significance of vortex ring formation to the impulse and thrust of a starting jet," *Physics of Fluids,* Vol. 15, number 5, pp.1271-1281.

[15] Kundu, P. and Cohen, I. (2004) *Fluid Mechanics, Third Edition*, El Sevier Academic Press.

[16] Lauder, G., Madden, P., Hunter, I., Tangorra, J., Davidson, N., Proctor, L., Mittal, R., Dong, H., and Bozkurttas, M. (2005) "Design and performance of a fish-fin-like propulsor for AUVs," *Proceedings of the 14th International Symposium on Unmanned Untethered Submersible Technologies.*

[17] Licht, S., Polidoro, V., Flores, M., Hover, F., Triantafyllou, M. (2004) "Design and projected performance of a flapping foil AUV," *IEEE Journal of Oceanic Engineering,* Vol. 29, No.3, pp. 786-794.

[18] Mohseni, K., Hongyu R, and Collonius, T. (1991) "Numerical experiments on vortex ring formation", *Journal of Fluid Mechanics,* Vol. 430, pp. 267-282..

[19] Prempraneerach, P., Hover, F., and Triantafyllou, M. (2003) "The effect of chordwise flexibility on thrust and efficiency of a flapping foil," *Proceedings of the 13th International Symposium Unmanned Untethered Submersible Technologies.*

[20] Raffel, M., Willert, C., and Kompenhans, J. (1998) *Particle Image Velocimetry: A Practical Guide*, Springer.

[21] Read, D., Over, F., and Triantafyllou, M. (2003) "Forces on oscillating foils for propulsion and maneuvering," *Journal of Fluids and Structures,* Vol. 17, pp. 163-183.

[22] Sfakiotakis, M., Lane, D., and Davies, B. (1999) "Review of fish swimming modes for aquatic locomotion," *IEEE Journal of Oceanic Engineering,* Vol. 24. No. 2, pp. 237-252.

[23] Taylor, G., Nudds, R., and Thomas, A. (2003) "Flying and swimming animals cruise at a Strouhal number tuned for high efficiency," *Nature*, Vol. 425, pp. 707-711.

[24] Triantafyllou, G., Triantafyllou, M., and Grosenbaugh, M. (1993) "Optimal thrust development in oscillating foils with application to fish propulsion," *Journal of Fluids and Structures*, Vol. 7, pp. 205-224.

[25] Triantafyllou, M., Techet, A., Hover, F. (2004) "Review of experimental work in biomimetic foils," *IEEE Journal of Oceanic Engineering*, Vol. 29, No. 3, pp. 585-594.

[26] Videler, J. (1993) *Fish Swimming*, Chapman and Hall.

[27] von Ellenrieder, K., Parker, K., and Soria, J. (2003) "Flow structures behind a heaving and pitching finite-span wing," *Journal of Fluid Mechanics*, Vol. 490, pp. 129-128.

[28] von Kármán, T. and Burgers, J. (1934) *General Aerodynamic Theory: Perfect Fluids*, Vol. 2, *Aerodynamic Theory,* Springer.

[29] Weihs, D. (1972) "A hydrodynamic analysis of fish manoeuvres," *Proceedings of the Royal Society of London B*, Vol. 182, pp. 59-72.

[30] Wu, T. (1971) "Hydromechanics of Swimming Propulsion. Part 1. Swimming of a two-dimensional flexible plate at variable forward speeds in an inviscid fluid," *Journal of Fluid Mechanics,* Vol. 26, part 2., pp. 337-355.